



Petri Hannukainen

**NON-LINEAR JOURNAL BEARING MODEL FOR
ANALYSIS OF SUPERHARMONIC VIBRATIONS OF
ROTOR SYSTEMS**

Thesis for the degree of Doctor of Science (Technology) to be presented with due permission for public examination and criticism in the Auditorium 1383 at Lappeenranta University of Technology, Lappeenranta, Finland on the 14th of November, 2008, at noon.

Acta Universitatis
Lappeenrantaensis
321

Supervisor Professor Aki Mikkola
Institute of Mechatronics and Virtual Engineering
Department of Mechanical Engineering
Lappeenranta University of Technology
Finland

Reviewers Professor Jouko Karhunen
Laboratory of Machine Design
University of Oulu
Finland

D.Sc. Markku Keskiniva
Sandvik Mining and Construction
Tampere
Finland

Opponents Professor Jouko Karhunen
Laboratory of Machine Design
University of Oulu
Finland

Professor Erno Keskinen
Machine Dynamics Laboratory
Tampere University of Technology
Finland

ISBN 978-952-214-643-4
ISBN 978-952-214-644-1 (PDF)
ISSN 1456-4491

Lappeenrannan teknillinen yliopisto
Digipaino 2008

ABSTRACT

Petri Hannukainen

Non-Linear Journal Bearing Model for Analysis of Superharmonic Vibrations of Rotor Systems

Lappeenranta, 2008

111 p.

Acta Universitatis Lappeenrantaensis 321
Diss. Lappeenranta University of Technology

ISBN 978-952-214-643-4 ISBN 978-952-214-644-1 (PDF) ISSN 1456-4491

A rotating machine usually consists of a rotor and bearings that supports it. The non-idealities in these components may excite vibration of the rotating system. The uncontrolled vibrations may lead to excessive wearing of the components of the rotating machine or reduce the process quality. Vibrations may be harmful even when amplitudes are seemingly low, as is usually the case in superharmonic vibration that takes place below the first critical speed of the rotating machine. Superharmonic vibration is excited when the rotational velocity of the machine is a fraction of the natural frequency of the system. In such a situation, a part of the machine's rotational energy is transformed into vibration energy. The amount of vibration energy should be minimised in the design of rotating machines. The superharmonic vibration phenomena can be studied by analysing the coupled rotor-bearing system employing a multibody simulation approach.

This research is focused on the modelling of hydrodynamic journal bearings and rotor-bearing systems supported by journal bearings. In particular, the non-idealities affecting the rotor-bearing system and their effect on the superharmonic vibration of the rotating system are analysed. A comparison of computationally efficient journal bearing models is carried out in order to validate one model for further development. The selected bearing model is improved in order to take the waviness of the shaft journal into

account. The improved model is implemented and analyzed in a multibody simulation code.

A rotor-bearing system that consists of a flexible tube roll, two journal bearings and a supporting structure is analysed employing the multibody simulation technique. The modelled non-idealities are the shell thickness variation in the tube roll and the waviness of the shaft journal in the bearing assembly. Both modelled non-idealities may cause subharmonic resonance in the system. In multibody simulation, the coupled effect of the non-idealities can be captured in the analysis. Additionally one non-ideality is presented that does not excite the vibrations itself but affects the response of the rotor-bearing system, namely the waviness of the bearing bushing which is the non-rotating part of the bearing system. The modelled system is verified with measurements performed on a test rig. In the measurements the waviness of bearing bushing was not measured and therefore its affect on the response was not verified. In conclusion, the selected modelling approach is an appropriate method when analysing the response of the rotor-bearing system. When comparing the simulated results to the measured ones, the overall agreement between the results is concluded to be good.

Keywords: Rotor dynamics, flexible multibody systems, journal bearing, shaft journal waviness

UDC 621.822.5 : 534.44

ACKNOWLEDGEMENTS

This research work was mainly carried out between 2000 and 2004 in the Institute of Mechatronics and Virtual Engineering at Lappeenranta University of Technology. The work was done as a part of PyöriVÄRE project that was financed by the National Technology Agency of Finland (TEKES).

Many compliments goes to my superiors Seppo Anttila, Arto Hietanen and Sam Freesmeyer at my current employer Valtra Inc. for providing the possibility to finalize my doctoral thesis work at the time I have been working for Valtra.

I would like to thank all the people in the Institute of Mechatronics and Virtual Engineering at Lappeenranta University of Technology. Specially, D.Sc. Jussi Sopanen and the supervisor of the thesis, professor Aki Mikkola has provided a lot of advices and effort during my thesis work.

I wish to thank the reviewers of the thesis, D.Sc. Markku Keskiniva from Sandvik Mining and Construction and Professor Jouko Karhunen from University of Oulu, for their valuable comments and corrections.

I am happy to acknowledge the financial support provided by Tekniikan edistämissäätiö and Lahja ja Lauri Hotisen rahasto.

Finally, many thanks go to my whole family and especially I would like to dedicate this thesis to my wife Mariliina and daughter Meeri who have given a lot of motivation to complete this work.

Petri Hannukainen

November, 2008

Lappeenranta, Finland

CONTENTS

1	INTRODUCTION	15
1.1	General	15
1.2	Analysing Tools for Rotating Machines	18
1.3	Previous Studies on Journal Bearings	19
1.4	Scope of the Study and Overview of the Dissertation.....	21
1.5	Contribution of the Dissertation.....	22
2	MODELS OF JOURNAL BEARINGS	23
2.1	Reynolds Equation	25
2.1.1	Boundaries in the Integration of the Pressure Equation.....	29
2.2	Short Journal Bearing Model 1	34
2.3	Short Journal Bearing Model 2	36
2.4	Long Journal Bearing Model 1.....	40
2.5	Long Journal Bearing Model 2.....	43
2.6	Comparison and Validation of the Journal Bearing Models	47
2.6.1	Comparison of the Static Characteristics of the Models	47
2.6.2	Comparison of the Dynamic Characteristics of the Models	51
2.6.3	A Validation of the Model for Multibody Simulations.....	57
3	NON-IDEALITIES IN JOURNAL BEARING	59
3.1	Modelling of Waviness of the Shaft Journal	60
3.2	Modelling of Waviness of the Bearing Bushing	66
4	NUMERICAL EXAMPLES	68
4.1	A Rigid Rotor with Journal Bearing.....	68
4.1.1	The computation of linearized responses	69
4.1.2	Comparison between linear and non-linear models	74
4.2	A Simulation Model of a Roll Tube Supported by Plain Journal Bearings .80	80
4.2.1	Multibody Dynamics.....	81
4.2.2	Flexible Roll Tube.....	84
4.2.3	Support of the Roll	89
4.2.4	Journal Bearing	90
4.2.5	Shaft Journal Waviness	91
4.2.6	Bearing Bushing Waviness	93
4.2.7	Temperature and Viscosity of the Lubricants	94
4.2.8	Measurements of the Rotor System	95

4.2.9	Verification of the Model of the Rotor-Bearing System.....	96
5	CONCLUSIONS	103
5.1	Suggestions for Future Studies.....	105
	REFERENCES	107

NOMENCLATURE

Abbreviations

ADAMS	Automatic Dynamic Analysis of Mechanical Systems
FEM	Finite Element Method
FFT	Fast Fourier Transform

Symbols

\mathbf{A}^i	Rotation matrix of body i
a_1, a_2	Adjusting parameters defined by Equations (2.47) and (2.48)
b_1, b_2	Adjusting parameters defined by Equations (2.59) and (2.60)
C_1, C_2	Integration constants
C_{1e}, C_{2e}	Integration constants in non-ideal equations
\mathbf{C}	Vector of kinematical constraint equations
\mathbf{C}_q	Constraint Jacobian matrix
c	Radial clearance of the bearing
c_e	Radial clearance of the non-ideal journal bearing
$c_1 \dots, c_5$	Adjusting parameters defined by Equations (2.52) – (2.56)
D	Diameter of the shaft journal
D_{ij}	Dimensional linearized damping coefficient of the bearing
D'_{ij}	Dimensionless linearized damping coefficient of the bearing
\mathbf{D}	Damping matrix
e	Eccentricity of the shaft journal
e_0	Eccentricity of the shaft journal at static equilibrium
e_u	Distance of mass unbalance from rotating axis
e_x, e_y	Eccentricity components of shaft journal
F_x, F_y	Force components in bearing coordinate system
F_{xu}, F_{yu}	Force components caused by unbalance
F_{slX}, F_{slY}	Force components caused by sliding in bearing coordinate system

F_{sqX}, F_{sqY}	Force components caused by squeezing in bearing coordinate system
F_r, F_t	Radial and tangential force components, respectively
F_{r0}, F_{t0}	Radial and tangential force components at static equilibrium, respectively
F_{slr}, F_{slt}	Radial and tangential force components caused by sliding, respectively
F_{sqr}, F_{sqt}	Radial and tangential force components caused by squeezing, respectively
$\mathbf{F}_s, \mathbf{F}_c$	Unbalance force vectors
g_r, g_t	Dimensionless functions defined by Equations (2.67) – (2.70)
h	Oil film thickness of ideal journal bearing
h_{be}	Non-ideal oil film thickness, when non-ideal shaft journal and bearing bushing accounted for
h_e	Non-ideal oil film thickness, when non-ideal shaft journal accounted for
I	Inertia tensor
K_{ij}	Dimensional linearized stiffness coefficients of the bearing
K'_{ij}	Dimensionless linearized stiffness coefficients of the bearing
K	Stiffness matrix
k	Order of the waviness component
L	Length of the bearing
M	Mass matrix
M	Rotor mass
m_u	Mass of unbalance
n	Number of generalized coordinates
n_c	Number of constraint equations
O_i	Origin of local coordinate system
p	Pressure
p_{cl}	Centreline pressure caused by sliding
p_{c2}	Centreline pressure caused by squeezing
p_e	Pressure of non-ideal bearing
p_{sl}	Pressure caused by sliding

p_{sq}	Pressure caused by squeezing
p^i	Arbitrary particle of body I
$Q(\varepsilon)$	Dimensionless function defined by Equation (2.91)
\mathbf{Q}_c	Vector that arises by differentiating the constraint equations twice with respect to time
\mathbf{Q}_e	Generalised force vector
\mathbf{Q}_v	Quadratic velocity vector
q_i	Generalized coordinate
\mathbf{q}^i	Vector of generalized coordinates
R_{b0}	Nominal radius of the bearing bushing
R_{be}	Non-ideal radius of the bearing bushing
R_{bk}	k^{th} order waviness component of the bearing bushing
R_e	Non-ideal radius of the shaft journal
R_k	k^{th} order waviness component of the shaft journal
R_0	Nominal radius of the shaft journal
R_1, \dots, R_3	Position coordinates in local coordinate system
\mathbf{R}^i	Position vector of the origin of the local coordinate system
\mathbf{r}^i	Position vector in global coordinate system
So_d, So_v	Adjusted Sommerfeld numbers, defined by Equations (2.46) and (2.58), respectively
T	Temperature of the lubricant
t	Time
t_i	Measured shell thickness of the roll in the node i
\dot{t}_i	Doubled shell thickness of the roll in the node i
U_e	Surface velocity of the non-ideal shaft journal
U_0	Surface velocity of the shaft journal
U_1	Surface velocity of the bearing
$\bar{\mathbf{u}}^i$	Position vector of a particle in local coordinate system
W	Static load of the journal bearing

X	Bearing coordinate
x'	Shaft journal local coordinate
\mathbf{x}	Displacement vector of the rotor
$\mathbf{x}_s, \mathbf{x}_c$	Arbitrary vectors in solution of equations of motion
Y	Bearing coordinate
y'	Shaft journal local coordinate
Z	Axial coordinate

Greek Letters

α	Position angle of the imbalance mass
β	Orientation angle of the shaft journal about rotation axis
χ	Auxiliary angle defined by Equation (2.51)
δ_k	Relative waviness amplitude of the k^{th} order
ε	Dimensionless eccentricity ratio of the shaft journal
ε_0	Dimensionless eccentricity ratio of the shaft journal in static equilibrium
$\dot{\varepsilon}, \ddot{\varepsilon}_t$	Dimensionless velocity components of shaft journal
ϕ	Attitude angle of the shaft journal
ϕ_0	Attitude angle of the shaft journal in static equilibrium
$\dot{\phi}$	Time derivate of the attitude angle of the shaft journal
η	Dynamic viscosity of lubricant
η_x	Lubricant constant
φ	Angular coordinate of the shaft journal, defined by Equation (3.5)
λ	Vector of Lagrange multipliers
λ	Weighting factor
$\gamma_{1,2}$	Auxiliary angles, defined by Equations (2.71) and (2.72)
$\theta, \theta', \theta^*$	Circumferential coordinates
θ'_1, θ'_2	Integration limits
ρ	Density of the lubricant
τ	Phase angle of the unbalance mass
ω	Angular velocity of shaft journal
$\bar{\omega}$	Effective angular velocity of shaft journal defined by Equation (2.45)

ψ_{bk}	Phase angle of k^{th} order waviness component of the bearing bushing
ψ_k	Phase angle of k^{th} order waviness component of the shaft journal

Sub- and superscripts

c	Centreline
i	Body i
id	Ideal representation, waviness excluded
e	Non-ideal representation, waviness included

1 INTRODUCTION

1.1 General

Rotors are used in many practical devices such as electrical machines, combustion engines and paper machines. Rotors are supported by one or more bearings. The bearing plays a significant role when considering the dynamic and static characteristics of the rotating machine. Therefore, the machine designer should be aware of different types of bearings that could be used in the system under consideration [1]. Based on the structure, bearings can be divided into rolling bearings and journal bearings (also called as sliding bearings). Bearings can support either an axial or a radial load and, accordingly, bearings can also be classified based on the direction of the supported load. Additionally, there are bearing types that can carry both the axial and the radial load. In rolling bearings, the load carrying capacity is obtained by rolling elements such as rolls, needles or balls. In contrast, in journal bearings the load is carried by a pressurized oil film. The journal bearings can be divided into two groups based on the manner in which the oil film is pressurized. In hydrostatic bearings, the oil film is pressurized externally with a hydraulic pump. A hydrodynamic bearing can be considered as a self-acting bearing. This is due to the phenomena by which the pressure is generated inside the bearing. A hydrodynamic bearing needs no external pressure; only oil feeding needs to be taken care of. When the shaft rotates inside the bearing the oil starts to flow thus generating the load carrying pressure to the oil film.

In Figure 1, several common geometries of hydrodynamic and hydrostatic bearings are presented. Different types of bearings are developed in order to obtain good performance and lubrication conditions for various operating conditions. Figure 1 shows that oil can be provided to the bearing clearance in several ways. Different geometries of bearings such as cases (d) to (h) in Figure 1 are designed to provide a more stable bearing performance as compared to traditional cylindrical design. Rolling bearings consist of different constructions, as can be seen in Figure 2 where structures of the most common rolling bearings are shown. Different types of rolling elements enable larger loads with tolerable surface pressure. Additionally, the use of, for example, tapered rolling elements enables axial loading conditions. It is important to note,

however, that both the rolling and journal bearings require lubrication. If there is an insufficient supply of fluid in the journal bearing, the fluid film breaks down and the journal contacts the bearing surface. Bearings where such contact continuously occurs are called boundary-lubricated bearings. During the running up sequence, hydrodynamic bearings are usually boundary-lubricated. This is caused by very low rotational velocity that is not capable of generating a high enough pressure to carry the load [2]. One application of hydrodynamic bearing is a squeeze-film damper in which the sliding velocity between journal and bearing surface is zero. The operation of the squeeze-film damper is based on a squeeze motion that generates the oil pressure in the clearance space between the journal and bearing surfaces. Typically, squeeze-film dampers are used as assistance bearings to provide more damping to the rotating system while the main support of the rotor is accomplished with other bearings. Gas-lubricated bearings operate according to the same principle as oil-lubricated bearings. However, they have different performance characteristics than oil-lubricated bearings due to a highly compressible lubricant. Gas bearings may also be self-acting or externally pressurized.

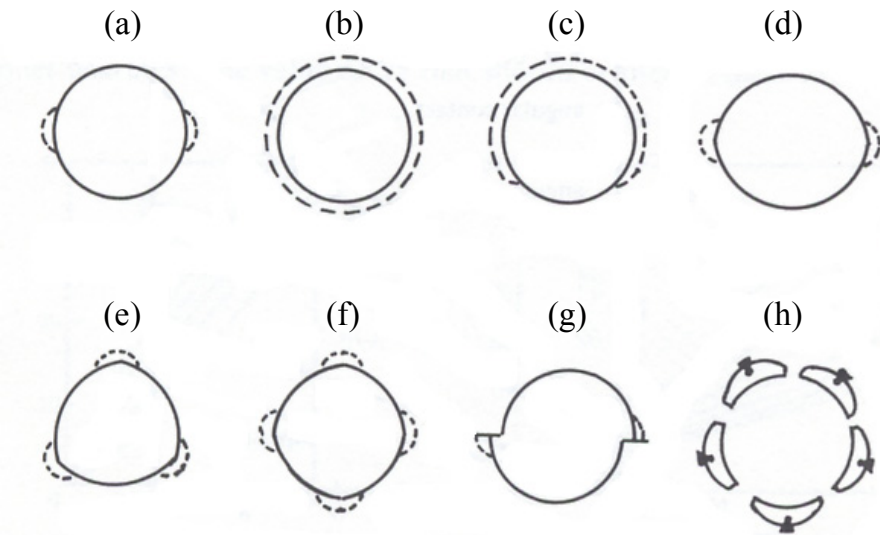


Figure 1. Types of journal bearings, (a) plain cylindrical with two axial grooves, (b) with circumferential groove, (c) partial arc, (d) lemon bore, (e) three-lobe, (f) four-lobe, (g) offset halves, (h) tilting pad [1].

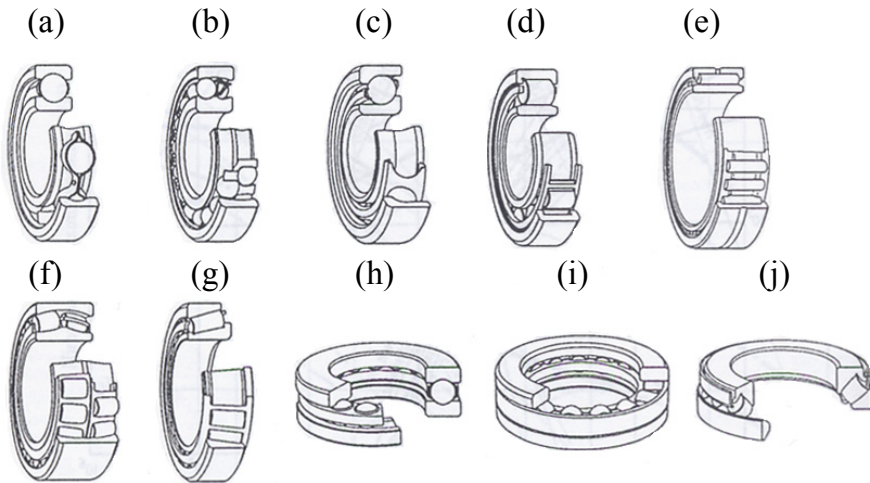


Figure 2. Different types of rolling bearings, (a) deep groove ball bearing, (b) double row ball bearing, (c) angular contact ball bearing, (d) cylindrical roller bearing, (e) needle roller bearing, (f) spherical bearing, (g) tapered roller bearing, (h) pressure ball bearing, (i) pressure cylindrical bearing and (j) spherical pressure bearing [3].

Demands of productivity in industry are continuously increasing. Consequently, the operating circumstances of the machines become more demanding from the product development point of view. When the angular velocity of the rotating machine increases, the vibration of the system plays a more significant role in the performance of the machine. The vibrations of the machine influence both the product quality and the operating life of the machine system. The use of a journal bearing is becoming more common in machines that operate at a high angular velocity. This is due to the fact that a journal bearing has significantly larger damping when compared to the traditional rolling bearing. Larger damping is a consequence of oil film thickness that is about ten times greater in journal bearings than in rolling bearings [4]. Another important feature in journal bearings is the low noise level while operating. This is also the result of thick oil film between the moving bodies. The drawbacks of a journal bearing when compared to a roller bearing are higher losses and need for a separate lubrication system.

It is important to note that a journal bearing has always some non-idealities that may excite vibrations in the rotor-bearing system, such as waviness in the shaft journal. In

addition, non-ideal geometry and material properties of the rotor may be a source of vibrations. A rotating machine is a complex system that consists of components that are coupled with each other. Accordingly, the overall performance of a rotating machine is defined by the operation of individual components as well as interactions of components. The coupling sets high demands for the analysis of rotating systems. This is due to the fact that all dynamically significant components should be taken into consideration in the analysis of rotor systems. Traditionally, each component of a rotating machine has been studied individually since the available computing tools are mainly developed for analysing individual components, such as, computation of linearized bearing coefficients for a certain operation condition. Which are furthermore used in a calculation code for rotor dynamics. For this reason, the interaction between components has been difficult to understand and account for in dynamic analysis.

The vibration of a rotor system depends upon its geometry and the type of the support, as well as the excitation forces. In this study, the bearing housing and pedestal are considered as the support structure. When considering the excitation of the bending vibrations of the rotor, the sources can be roughly divided into two areas namely, the rotor and the bearing assembly. Due to manufacturing tolerances, the rotor may have an uneven mass and stiffness distribution. On the other hand, the shaft journal waviness may excite vibrations due to an improper bearing assembly. As a result, these non-idealities may cause superharmonic vibrations in the rotor system. In this case, the natural vibration mode of the rotor is excited when the rotational velocity is a fraction of the natural frequency. It is important to note that the support structure of the rotating system does not usually excite any vibrations by itself. However, the support structure may affect the total stiffness and damping of the system and therefore it may have a significant effect to the performance of the rotating machine.

1.2 Analysing Tools for Rotating Machines

Several analysing tools for rotating machines have been developed. The most traditional approach is to use analytical equations to compute response and critical speeds of the rotor. Many analytical models of rotors and rotor systems have been presented in previous studies such as the Jeffcott rotor, which was introduced in 1895 by Föppl. The model was named after Jeffcott because in 1919 he explained the science of

rotordynamics in a graphical way, which is still in use today [5]. Many important results can be obtained analytically using the simple model of the Jeffcott rotor. The finite element method (FEM) is a computer based approach for the detailed modelling of flexible structures including rotors. FEM provides the possibility of computing response and critical speeds of the rotor. A number of customized computer codes have been created for analyzing rotor systems. An alternative approach to the analysis of a complete rotor system is the multibody dynamics simulation [6]. The multibody dynamics simulation provides a possibility of making analyses that cover important non-idealities in the bearing and rotor as well as the interactions between the system's components. Multibody simulation uses a general methodology that can describe the dynamics of machine components that undergo large relative translational and rotational displacement. This inevitably leads to non-linear equations of motion which must be solved with respect to time using numerical integration methods. The obtained time-domain results can be post-processed in order to study the response of the rotor system in the frequency domain. In multibody dynamics simulation, the machine components are described as individual bodies that can interact with each other via force and/or constraint equations. This makes it possible to describe the hydrodynamic force developed in a journal bearing. The flexibility of the elements of the multibody simulation model can be described using for example the lumped mass or the floating frame of reference approaches [7] and [8].

The use of simulations as a part of product development reduces both the time used and the costs involved. These advantages can mainly be obtained by the reduced need for physical prototypes that are expensive and time consuming to build. With the help of simulations, safety issues can be covered more comprehensively than by using traditional prototypes. Some testing, for example in extreme operating conditions and accident scenarios, can be done without risks when using a simulation model [9].

1.3 Previous Studies on Journal Bearings

Hydrodynamic journal bearings and their computational models have interested scientists for some time. A number of books and articles have been published concerning the theory of journal bearings. Pinkus and Sternlicht [10] have presented a theory of hydrodynamic lubrication. Specifically, Pinkus and Sternlicht presented the

general principles of fluid flow in the circumstances of bearing operation by introducing the differential equations for bases of bearing modelling. Also introduced were techniques for solving these equations analytically as well as some approximate solutions that provide the basis for the solutions of specific bearing problems. Cameron [11] has presented the basic theory and differential equations needed for journal bearing modelling. Techniques for solving bearing problems are presented in Cameron's study. In addition to hydrodynamic journal bearings, Cameron introduced solutions to bearings of other types. He has studied pad bearings, porous bearings and hydrostatic bearings as well as some aspects on the theory of viscosity of the fluids. Hamrock [12] has given detailed information on fluid film lubrication. He presented the theory on hydrodynamic bearing computation including rolling-element bearings. Hamrock also presented some tables of stiffness and damping coefficients for different types of fluid film bearings. Someya [13] has produced a handbook for bearing design. He presented theories related to journal bearings and explained techniques to compute dynamic coefficients for journal bearings. Furthermore, he presented a wide range of pre-calculated bearings stiffness and damping coefficients for different types of journal bearings.

Several authors have studied the non-idealities of journal bearings and their effect on the vibrations of the rotor system. Rasheed [14] has studied the surface waviness of a plain hydrodynamic bearing. He considered only the waviness of the non-rotating surface of the bearing, that is, the bearing bushing. Rasheed studied the influence of waviness on the load carrying capacity of the bearings and he concluded that the circumferential waviness of the bearing bushing increases load carrying capacity. Prakash and Peeken [15] have considered the combined effect of the roughness of the surface of the bearing and the elastic deformation of the bearing. They analyzed cases in which waviness was applied to both the rotating and the non-rotating surfaces. They found out that the elasticity of the bearing decreases the effects of roughness; however, they did not perform a vibration analysis of a rotor-bearing system. Bachschmid et al. [16] studied the geometrical errors of the shaft journal in a two-lobe "lemon-shaped" journal bearing. They considered only the so-called ovalization and its influence on the twice-running-speed vibration component of a rotating machine. Bachschmid et al. also carried out experimental measurements, which they compared to the simulations. In the simulations, they used a linearized model of the rotor-bearing system. The overall agreement between the measured and calculated results was not acceptable, but in the

horizontal direction, the vibrations were recognizable in both results. However, the mean value of the horizontal amplitude was considerable smaller in the analytical results.

1.4 Scope of the Study and Overview of the Dissertation

In this study, the models of hydrodynamic journal bearings are examined. One model is further developed to take the waviness of the shaft journal and bearing bushing into account. The bearing model is implemented in multibody dynamics simulation software where it performs as an interface element in a rotor system simulation. The focus of this study is in superharmonic vibrations of the rotor generated by the coupling of non-idealities in the bearing assembly and the rotor. Analysis of superharmonic vibrations of the rotor system requires detailed bearing modelling. Therefore, this study concentrates on journal bearing modelling.

Chapter 2 presents four different solutions for computing hydrodynamic forces acting in plain journal bearings. A comparison of the bearing models is accomplished by computing the load carrying capacity of the models and by computing the linearized dynamic coefficients based on each model. As well, the computation of linearized bearing coefficients is presented. In chapter 2, one model is chosen for further development in order to take non-idealities into account.

Chapter 3 deals with the non-idealities of the bearing assembly. A method for describing the waviness of the shaft journal and bearing bushing is introduced. In the method, a geometrical error is introduced to the equation of journal bearings film thickness with help of the Fourier cosine series. This expansion leads to the integration of complex trigonometric equations that are solved numerically to obtain the description of the hydrodynamic force. The simulation model of the hydrodynamic plain journal bearing that is extended in this study to include the waviness of the shaft journal and bearing bushing is employed in a simulation model of a tube roll supported by journal bearings. By exploiting geometric information measured from the real structure, the present inaccuracies can be modelled accurately.

Chapter 4 presents two different numerical examples to study the developed bearing model. The first example consists of a simple rotor-bearing system with two degrees of freedom. This example is used to study the difference between linear and non-linear bearing theory. In addition, the non-linear bearing model used is verified with the results obtained from literature. In the second example the simulation model and the measurement installation of the test rig are presented. The results from comparison of the simulation model and experimental data from the test rig are presented to verify the simulation model of the test rig.

Conclusions and suggestions for further studies are given in Chapter 5.

1.5 Contribution of the Dissertation

The contribution of the research is the modelling of non-idealities in the journal bearing assembly. Non-idealities under investigation include waviness of a shaft journal as well as waviness of a bearing bushing. These non-idealities have been introduced to non-linear journal bearing model by employing cosine terms of the Fourier series in the equation of bearings film thickness and its derivates. This leads to complex representation of pressure distribution in the journal bearing. For this reason, the numerical integration procedure based on the Midpoint rule with appropriate boundary conditions is used to compute bearing force components. In this study, the introduced modelling approach to account for non-idealities of the journal bearing assembly is employed in the dynamic analysis of cylindrical journal bearings. However, the modelling approach can be extended in a straightforward manner to other journal bearing types. Non-linear journal bearing model with description of shaft journal and bearing bushing waviness is implemented into a multibody simulation software application where the model can be used as an interface element between the rotor and supporting structure. In the multibody simulation, the bearing model is used to analyze superharmonic responses of a tube roll. In order to validate introduced simulation model, numerical results are verified with experimental measurements.

2 MODELS OF JOURNAL BEARINGS

In this chapter, different solutions for computing hydrodynamic forces acting in a plain cylindrical journal bearing are introduced. A survey is made to explore models of journal bearings obtained from literature for a plain journal bearing that is shown in Figure 3.

In this study, only resulting force component equations are presented, while derivations of equations may be found in References [17]-[21]. Two solutions for infinitely short journal bearings and two solutions for finite length journal bearings are studied. All models are based on the analytical solution of the Reynolds equation. The Reynolds equation is a second order differential equation that can be used to describe pressure distribution over the bearing surface as a function of eccentricity, angular and radial velocities of the journal. The solution of Reynolds equation usually employs the Half-Sommerfeld boundary condition in the integration of the pressure equation. A closed form solution for integration of pressure equation can be obtained in certain cases [22]. It is noteworthy that the journal bearing models based on the Reynolds equation computes non-linear bearing forces. For this reason, they also apply to scenarios where large displacements of the shafts take the place. Such situations are in practice, for example, a run-up of a rotating machine or the acceleration of a rotor over its critical speed. One of the introduced models is chosen for detailed studies of the rotor system. The selected model is further developed to be appropriate for use in simulations in which the vibrations of rotating systems supported with plain journal bearings is under consideration.

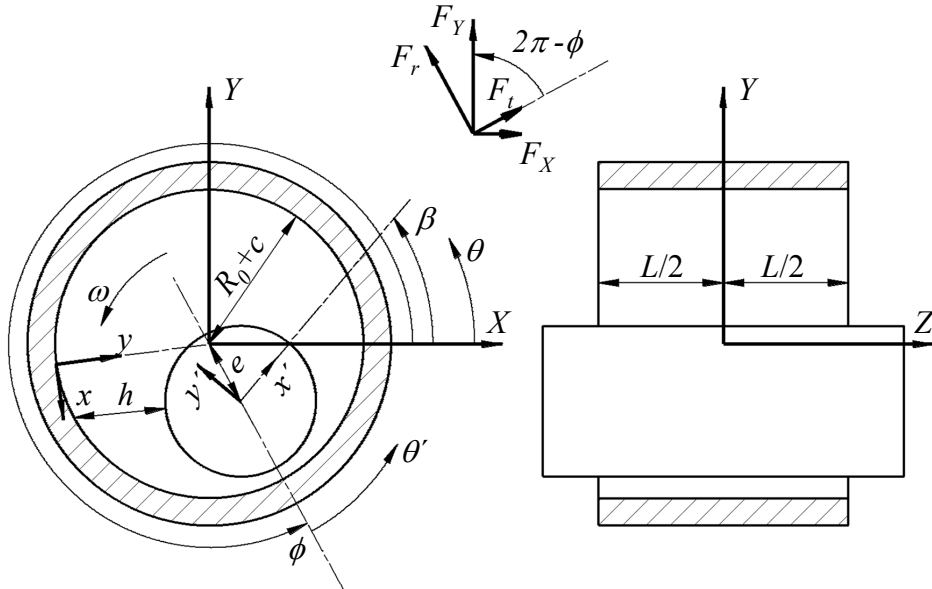


Figure 3. Geometry of the plain journal bearing.

In Figure 3, the geometry of the journal bearing, force components and coordinate systems are depicted. In this study, three different coordinate systems are used. The bearing coordinate system (XY) is fixed, that is, it does not rotate or translate; the hydrodynamic forces are computed in this coordinate system. The moving coordinate system (xy) is used in the definition of the Reynolds equation. The coordinate system ($x'y'$) is attached to the journal. The axial coordinate is described with Z , and two circumferential coordinates are used. Firstly, circumferential coordinate θ is defined in the bearing coordinate system and is used in the definition of the Reynolds equation while θ' is a circumferential coordinate which is used in integration of the hydrodynamic pressure equation. The relationship between circumferential coordinates can be presented as $\theta' = \theta - \phi$, where ϕ is the attitude angle of the journal as can be seen in Figure 3. The attitude angle ϕ is defined in Equation (2.23). Furthermore, the directions of hydrodynamic force components are illustrated in Figure 3. The force components F_X and F_Y apply on fixed directions of bearing coordinate axes X and Y . The directions of radial F_r and tangential F_t force components depend on the journal attitude angle ϕ .

2.1 Reynolds Equation

The basic problem of hydrodynamic bearing analysis is the determination of the fluid-film pressure for a given bearing geometry. A solution to this problem can be found by solving the Reynolds equation of the case under investigation. In the following, the pressure distribution of the journal bearing is introduced. The Reynolds equation was originally developed by Osborne Reynolds in 1886. This equation provides the basis of modern lubrication theory. Presentation of the Reynolds equation can be found in reference [17]. For the journal bearing geometry, as shown in Figure 3, the Reynolds equation can be written as follows [17]:

$$\frac{\partial}{\partial x} \left(h^3 \frac{\partial p}{\partial x} \right) + \frac{\partial}{\partial Z} \left(h^3 \frac{\partial p}{\partial Z} \right) = 6\eta \left\{ \frac{\partial}{\partial x} [(U_0 + U_1)h] + 2 \frac{\partial h}{\partial t} \right\}, \quad (2.1)$$

where h and η are the fluid film thickness and the dynamic viscosity of an incompressible lubricant, respectively. In Equation (2.1), p is the hydrodynamic pressure acting in the journal bearing and t is time. According to Figure 3, Z is the axial and x is the circumferential coordinate of the bearing. In Equation (2.1), U_0 and U_1 are the surface velocities of the shaft and the bearing housing in tangential direction. The variable U_1 can be set to zero when the bearing housing is fixed. The Equation (2.1) includes a number of assumptions that the user should be aware of. Understanding the limitations of the solutions of Equation (2.1) is essential when applying the equation for practical applications. The assumptions of Equation (2.1) can be summarized as follows:

1. Viscous shear effects dominate in terms of the fluid parameter. In practice, the viscosity is the only fluid parameter used while other parameters such as fluid inertia forces are ignored.
2. The fluid is assumed to be incompressible. In general, fluid compressibility plays a role in machine dynamics as it is often the case in hydraulically driven machines. However, in the case of hydrodynamic bearings, the film is thin and the oil volume small so that the compression would be negligible.
3. The viscosity is assumed to be constant throughout the film. Due to the thinness of the oil film this assumption can be made without a significant loss of accuracy.

4. The pressure is assumed to be constant throughout the film thickness. In some situations, as in sudden impacts, there may appear local pressure waves in the lubricant film. However, in the case of thin fluid film, the pressure can be assumed to be constant over the film thickness.
5. The fluid film is assumed to be thin compared to the length and width of the bearing. When this assumption is valid, any curvature of the film can be ignored.
6. It is assumed that there is no slip on the wall (in between the fluid-solid boundaries). This is an assumption that is generally used in hydrodynamics.
7. The lubricant is assumed to be Newtonian; stress is proportional to the rate of the shear. The lubricants used in journal bearings are usually considered to behave as Newtonian fluids.

The use of cylindrical coordinates (θ, Z) in the Reynolds equation is convenient because of the bearing's geometry. The Reynolds equation can be modified to cylindrical coordinates by applying the following relation:

$$\frac{\partial}{\partial x} = \frac{1}{R_0} \frac{\partial}{\partial \theta}, \quad (2.2)$$

where R_0 is the nominal radius of the journal. Substituting the cylindrical coordinates the Reynolds equation gives us:

$$\frac{1}{R_0} \frac{\partial}{\partial \theta} \left(h^3 \frac{1}{R_0} \frac{\partial p}{\partial \theta} \right) + \frac{\partial}{\partial Z} \left(h^3 \frac{\partial p}{\partial Z} \right) = 6\eta \left(\frac{1}{R_0} \frac{\partial}{\partial \theta} U_0 h + 2 \frac{\partial h}{\partial t} \right). \quad (2.3)$$

The film thickness h of the cylindrical bearing geometry can be expressed using notations shown in Figure 3 as follows:

$$h = c - e_x \cos(\theta) - e_y \sin(\theta), \quad (2.4)$$

where c is the radial clearance of the bearing, e_x and e_y are the perpendicular components of shaft journal eccentricity e according to the bearing coordinate axis (XY),

respectively. The time derivative of the fluid film thickness in Equation (2.3) can be written as follows:

$$\frac{\partial h}{\partial t} = -\dot{e}_x \cos(\theta) - \dot{e}_y \sin(\theta), \quad (2.5)$$

where \dot{e}_x and \dot{e}_y are time derivatives of the displacement components. The partial derivative of the film thickness with respect to the circumferential coordinate can be expressed as follows:

$$\frac{\partial h}{\partial \theta} = e_x \sin(\theta) - e_y \cos(\theta). \quad (2.6)$$

The surface velocity of the shaft can be written as

$$U_0 = \omega R_0 - \dot{e}_x \sin(\theta) + \dot{e}_y \cos(\theta), \quad (2.7)$$

where ω is the angular velocity of the shaft. The partial derivative of the surface velocity with respect to θ gives:

$$\frac{\partial U_0}{\partial \theta} = -\dot{e}_x \cos(\theta) - \dot{e}_y \sin(\theta). \quad (2.8)$$

The substitution of Equations (2.4), (2.5), (2.6), (2.7) and (2.8) to the right hand side of Equation (2.3) gives:

$$\begin{aligned} 6\eta \left(\frac{1}{R_0} \frac{\partial}{\partial \theta} U_0 h + 2 \frac{\partial h}{\partial t} \right) = \\ 6\eta \left\{ \frac{[-\dot{e}_x \cos(\theta) - \dot{e}_y \sin(\theta)][c - e_x \cos(\theta) - e_y \sin(\theta)]}{R_0} \right. \\ \left. + \frac{[\omega R_0 - \dot{e}_x \sin(\theta) + \dot{e}_y \cos(\theta)][e_x \sin(\theta) - e_y \cos(\theta)]}{R_0} \right\}_+ \\ 12\eta [-\dot{e}_x \cos(\theta) - \dot{e}_y \sin(\theta)] \end{aligned} \quad (2.9)$$

Making the approximation that $c, e_x, e_y \ll R_0$, the equation can be simplified as follows:

$$6\eta \left(\frac{1}{R_0} \frac{\partial}{\partial \theta} U_0 h + 2 \frac{\partial h}{\partial t} \right) = 6\eta \left[(e_x \omega - 2\dot{e}_y) \sin(\theta) - (e_y \omega + 2\dot{e}_x) \cos(\theta) \right]. \quad (2.10)$$

The Reynolds equation can be further simplified by making the assumption of a short journal bearing. The short bearing theory can be applied when the length-to-diameter (L/D) ratio is less than 0.5. This assumption means, in practice, that the circumferential pressure gradient $\frac{1}{R_0} \frac{\partial p}{\partial \theta}$ is negligible with respect to the axial pressure gradient $\frac{\partial p}{\partial Z}$. In this case, the Reynolds equation can be written as:

$$\frac{\partial^2 p}{\partial Z^2} = \frac{6\eta \left[(e_x \omega - 2\dot{e}_y) \sin(\theta) - (e_y \omega + 2\dot{e}_x) \cos(\theta) \right]}{h^3}. \quad (2.11)$$

In order to obtain the pressure equation that describes the 2-dimensional pressure field in the journal bearing, the Equation (2.11) should be integrated twice with respect to axial coordinate Z . The first integration gives:

$$\left(\frac{\partial p}{\partial Z} \right) = \frac{6\eta}{h^3} \left(\frac{1}{R_0} \frac{\partial}{\partial \theta} U_0 h + 2 \frac{\partial h}{\partial t} \right) Z + C_1. \quad (2.12)$$

The second integration gives:

$$p = \frac{3\eta}{h^3} \left(\frac{1}{R_0} \frac{\partial}{\partial \theta} U_0 h + 2 \frac{\partial h}{\partial t} \right) Z^2 + C_1 Z + C_2, \quad (2.13)$$

where C_1 and C_2 are constants of integration. To obtain values for the constants C_1 and C_2 two boundary conditions are introduced. Firstly, it can be stated that the pressure on both sides of the bearing is zero if the atmospheric pressure is ignored, as it is very small when compared to the hydrodynamic pressure acting in the bearing. Secondly, the

pressure distribution in the axial direction is assumed to be parabolic and symmetric with respect to the centreline of the bearing. This condition can be written as follows:

$$\left(\frac{\partial p}{\partial Z} \right) = 0, \quad Z = 0. \quad (2.14)$$

According to this condition, it can be seen that $C_1 = 0$. The second constant of integration can be solved employing the first condition. When using $Z = L/2$ in Equation (2.13), where L is the length of the bearing, and setting the pressure to zero C_2 can be solved as follows:

$$C_2 = -\frac{3\eta}{h^3} \left(\frac{1}{R_0} \frac{\partial}{\partial \theta} U_0 h + 2 \frac{\partial h}{\partial t} \right) \frac{L^2}{2}. \quad (2.15)$$

Accordingly, the pressure equation in cylindrical coordinates can be written as:

$$p(Z, \theta) = \frac{3\eta}{h^3} \left(\frac{1}{R_0} \frac{\partial}{\partial \theta} U_0 h + 2 \frac{\partial h}{\partial t} \right) \left(Z^2 - \frac{L^2}{2} \right). \quad (2.16)$$

Using the notations of Equations (2.4), (2.5) and (2.8) the pressure equation takes the form:

$$p(Z, \theta) = \frac{3\eta}{h^3} \left[(e_x \omega - 2\dot{e}_y) \sin(\theta) - (e_y \omega + 2\dot{e}_x) \cos(\theta) \right] \left(Z^2 - \frac{L^2}{2} \right). \quad (2.17)$$

2.1.1 Boundaries in the Integration of the Pressure Equation

A common procedure when computing non-linear hydrodynamic forces acting in a plain journal bearing is to integrate the pressure equation over the bearing surfaces. As can be seen in Figure 4, the pressure equation is a function of two variables that are the axial and circumferential coordinates of the bearing. The axial distribution of pressure is defined by a parabolic function while the circumferential distribution is defined by trigonometric functions. The pressure distribution in the journal bearing is generated

due to sliding and squeezing according to Equation (2.17). In Figure 4, the two-dimensional pressure distributions caused by these two phenomena are depicted with respect to axial and circumferential coordinates Z and θ' , respectively.

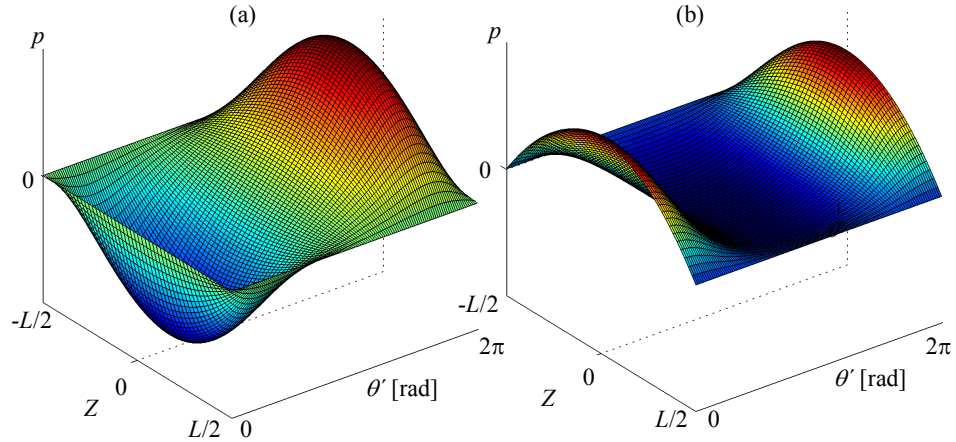


Figure 4. The pressure field generated in the journal bearing by (a) sliding, (b) squeezing.

There are several different boundary conditions introduced in literature that can be used to integrate the pressure field along circumferential coordinate of the hydrodynamic bearing. These boundary conditions are introduced in the following. Basically, different boundary conditions introduce different integration boundaries in circumferential direction θ when integrating the pressure equation into the hydrodynamic force equations.

Full-Sommerfeld Boundary Condition

In case of Full-Sommerfeld boundary condition, the pressure is integrated over the bearing's circumferential coordinate ($\theta = 0 \dots 2\pi$). As can be seen, for example, in Figure 6, the solution of the Reynolds equation with respect to the journal motion develops a high positive pressure at one side of the bearing while there is an equal negative pressure on the opposite side of the bearing. In natural conditions, the lubricant cannot stand negative pressure due to the rupture of the oil film. The saturation pressure of commonly used mineral oils is close to the normal ambient pressure. Additionally

this condition assumes that the zero pressure is obtained in circumferential coordinate positions where the film thickness is smallest and largest as can be seen when looking at Figure 5 and Figure 3. Due to the abovementioned reasons, the Full-Sommerfeld boundary condition gives an unrealistic pressure field. Consequently, the hydrodynamic force obtained using these integration boundaries may be defected.

Half-Sommerfeld Boundary Condition

This condition is similar to Full-Sommerfeld boundary condition except that all negative pressures are ignored. According to the first presenter of this method, it is also called Gumbel's boundary condition. When integrating the pressure field according to the Half-Sommerfeld condition the integration boundaries are $\theta'_1 = -\pi$ and $\theta'_2 = 0$. Even if this is a very simplified approach it gives reasonable results and is often used. The advantage of this method is that it leads to analytical solution of the plain cylindrical bearing.

Reynolds Boundary Condition

The Half-Sommerfeld boundary condition gives a more realistic description than the Full-Sommerfeld boundary condition. However, it is important to note that the Half-Sommerfeld boundary condition leads to a violation of the continuity of mass flow at the outlet end of the pressure curve. When investigating the pressure according to the Half-Sommerfeld boundary condition near $\theta' = 0$, it can be seen that the pressure gradient is not zero when $\theta' < 0$ but jumps suddenly to zero at $\theta' = 0$ while remaining at zero when $\theta' \geq 0$. This can clearly be seen from Figure 5 (b). A more realistic boundary condition can be obtained using the Reynolds boundary condition, where

$$p = 0 \text{ and } \frac{dp}{d\theta'} = 0 \text{ at } \theta' = \theta^*.$$

Where θ^* is the circumferential coordinate where pressure goes to zero as can be seen in Figure 5. The Reynolds boundary condition is rarely used because of its complexity. The use of the Reynolds boundary condition leads to an iteration method. Since the Half-Sommerfeld boundary condition has proven to give a good prediction of a

bearing's performance, despite a violation of the continuity of the mass flow, it is used frequently [23]. Different boundary conditions are illustrated in Figure 5.

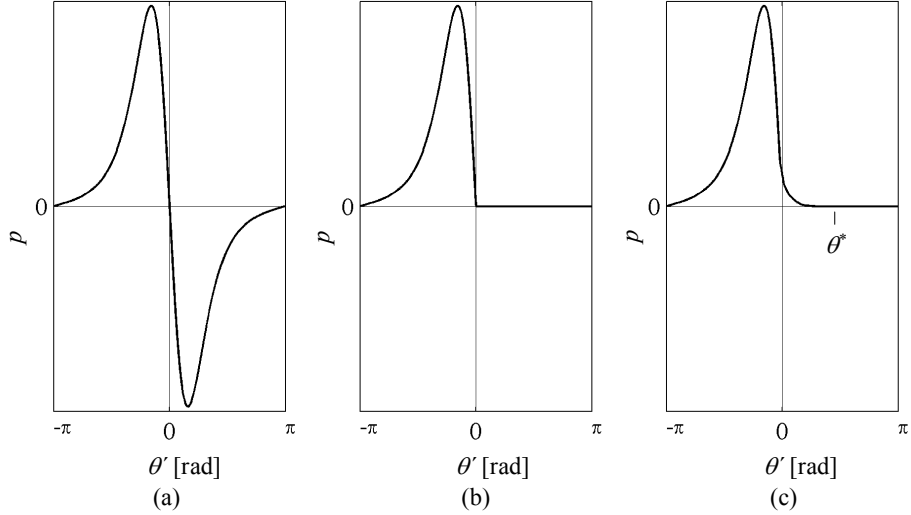


Figure 5. Different boundary conditions for integration of the pressure field, (a) Full-Sommerfeld boundary condition, (b) Half-Sommerfeld boundary condition, (c) Reynolds boundary condition.

Zero-Pressure Boundary Condition

If the rotor is not in equilibrium, that is, the journal has a translational movement when $\dot{e} \neq 0$, the pressure distribution fluctuates along the circumferential coordinate. The boundary of the zero-pressure has changed when comparing pressure curves of zero radial velocity and non-zero radial velocity. This can be observed from Figure 6, where the centreline pressures are plotted.

As can be seen in Figure 6 where the radial velocity component is depicted as a dotted line, both the Full-Sommerfeld and Half-Sommerfeld conditions result in faulty integration boundaries as they assume that zero pressure is located in the circumferential position of smallest and largest film thickness. If the pressure is generated by a sliding motion only, as is the case of the solid line in Figure 6, the positive pressure region can be obtained by setting the boundaries to be $\theta'_1 = -\pi$ and $\theta'_2 = 0$, corresponding to the Half-Sommerfeld boundary condition. On the other hand,

if the radial motion of the journal is involved, the use of Half-Sommerfeld boundary conditions leads to the integration of a pressure curve that is partly negative and partly positive. For this reason, the hydrodynamic force obtained by such an integration of the pressure equation may not be correct, when the assumption that oil fields rupture in the negative pressure region is valid. It is important to note that the roots of the pressure curve vary according to the radial velocity. Therefore, in order to obtain correct integration boundaries the roots of the pressure equation should be solved during simulation. In this case, the definition of integration limits needs to be carried out at each time step of the computation. In practice, it is convenient to use a numerical integration of the pressure equation while using the Zero-Pressure boundary condition with varying integration limits. Such a computation also takes into account the positive pressure region correctly even if the length of the region is not π in the circumferential direction, which is the assumption that both Half- and Full-Sommerfeld conditions make. The Zero-Pressure boundary condition should be applied when computing transient analysis where radial velocity components of the shaft journal are not zero. In this study a boundary condition that is based on Zero-Pressure boundary condition is used. The used boundary condition is discussed further in Chapter 3.1. A comparison of simulation results obtained from the rotor-bearing system by using the Half-Sommerfeld boundary condition and zero-pressure boundary condition can be found in [24].

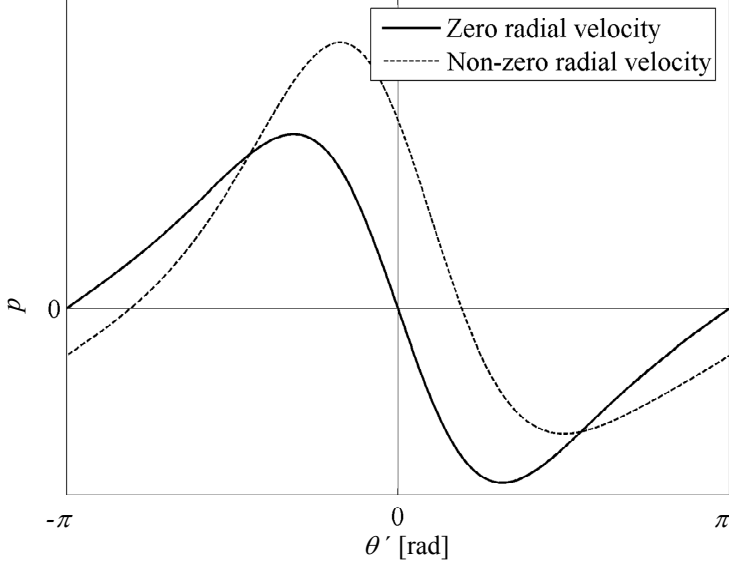


Figure 6. Centreline pressures of the bearing when the radial velocity of the journal appears, dotted line, and when the radial velocity is zero, solid line.

2.2 Short Journal Bearing Model 1

The solution of the infinitely short journal bearing introduced by Vance [17] is a general form of an analytical solution of hydrodynamic forces acting in a short journal bearing. The model employs the Half-Sommerfeld boundary condition in the integration of the pressure equation (Equation (2.17)). The integration is performed over a contracting region of oil film, in which case the selected integration limits are set to $\theta'_1 = -\pi$ and $\theta'_2 = 0$ according to the coordinate system shown in Figure 3. The hydrodynamic force components are obtained by integrating the Equation (2.17), as follows:

$$F_r = R_0 \int_{-\pi}^0 \int_{-\frac{L}{2}}^{\frac{L}{2}} p(\theta', Z) \cos(\theta') dZ d\theta', \quad (2.18)$$

$$F_t = R_0 \int_{-\pi}^0 \int_{-\frac{L}{2}}^{\frac{L}{2}} p(\theta', Z) \sin(\theta') dZ d\theta', \quad (2.19)$$

where F_r and F_t are the radial and tangential components of the hydrodynamic force, respectively. When evaluating the integrals in Equations (2.18) and (2.19), the hydrodynamic force components in the rotating coordinates can be written as:

$$F_r = -\eta R_0 L \left(\frac{L}{c} \right)^2 \left[(\omega - 2\dot{\phi}) \frac{\varepsilon^2}{(1-\varepsilon^2)^2} + \frac{\pi(1+2\varepsilon^2)\dot{\varepsilon}}{2(1-\varepsilon^2)^{5/2}} \right], \quad (2.20)$$

$$F_t = \eta R_0 L \left(\frac{L}{c} \right)^2 \left[(\omega - 2\dot{\phi}) \frac{\pi\varepsilon}{4(1-\varepsilon^2)^{3/2}} + \frac{2\varepsilon\dot{\varepsilon}}{(1-\varepsilon^2)^2} \right], \quad (2.21)$$

where $\dot{\phi}$ is the angular velocity of the journal whirling and can be written as follows:

$$\dot{\phi} = \frac{-\dot{e}_x \sin(\phi) + \dot{e}_y \cos(\phi)}{\sqrt{e_x^2 + e_y^2}}. \quad (2.22)$$

The attitude angle ϕ of the journal can be written as:

$$\phi = \tan^{-1} \left(\frac{e_y}{e_x} \right). \quad (2.23)$$

The dimensionless radial velocity $\dot{\varepsilon}$ can be written as:

$$\dot{\varepsilon} = \frac{\dot{e}_x \cos(\phi) + \dot{e}_y \sin(\phi)}{c}, \quad (2.24)$$

where ε is the dimensionless eccentricity ratio which can be written as:

$$\varepsilon = \frac{\sqrt{e_x^2 + e_y^2}}{c}. \quad (2.25)$$

The perpendicular hydrodynamic force components F_x and F_y in the bearing coordinate system (XY) can be obtained using the following relationship:

$$\begin{bmatrix} F_x \\ F_y \end{bmatrix} = \begin{bmatrix} \cos(\phi) & -\sin(\phi) \\ \sin(\phi) & \cos(\phi) \end{bmatrix} \begin{bmatrix} F_r \\ F_t \end{bmatrix}. \quad (2.26)$$

2.3 Short Journal Bearing Model 2

The second model is based on the analytical solution of the Reynolds equation under the assumptions of the short bearing theory. The model is based on hydrodynamic force equations presented by Cameron [11] and Lang [25]. The combined model based on References [11] and [25] is presented by Keskiniva [18]. The model uses the Half-Sommerfeld boundary condition. The difference in the model with respect to model 1 is that the sliding and squeeze pressure components are integrated using different boundary conditions. Typically, the Half-Sommerfeld boundary condition is used to integrate the pressure equation over the region where the pressure inside the bearing is known to be positive. This approach is applied in the model using two separate pressure distributions. The hydrodynamic force is computed from the positive pressure region of the sliding pressure and from the positive pressure region of the squeeze pressure. However, this approach may not correspond to the pressure distribution that can be found in reality. In the bearing, the pressure is formed due to the sliding and squeezing and for this reason the pressure field should be considered as a coupled function generated by both sliding and squeezing motions. If the radial velocity of the shaft is zero, this model leads to the same results as the short bearing model 1. As discussed in chapter 2.1.1, the dynamic behaviour of the bearing is rarely composed by this situation. If the radial velocity component is not equal to zero, the pressure distribution to be integrated is different in model 1 and in model 2, as can be seen in Figure 7. In Figure 7 the centreline pressures are illustrated over the circumferential coordinate, both of which the short bearing model uses in integration of the pressure distribution.

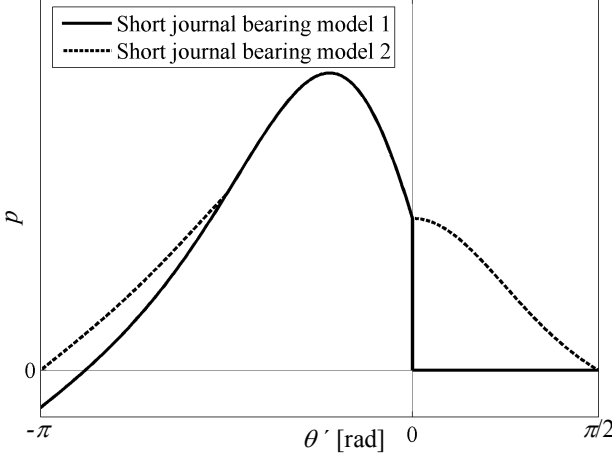


Figure 7. The circumferential pressure to be integrated according to two short journal bearing models with the presence of a radial velocity component.

As can be seen in Figure 7, models 1 and 2 predict the pressure distribution differently when radial velocity component is not zero. As was stated earlier in this chapter the prediction of Short journal bearing model 2 may be unrealistic in some cases. Nevertheless, the Short journal bearing model 1 also predicts the pressure distribution need to be integrated unrealistically. According to model 1, the integration boundaries of circumferential coordinate θ' is set to $-\pi$ and 0 according to the Half-Sommerfeld boundary condition. As can be seen in Figure 7, by using such integration boundaries in this case we use partly negative pressure in integration and on the other hand the positive pressure region is partly left out of the integration. Similar errors are made also in both two long bearing models presented in next chapters since they are using similar boundary conditions for integration. The solution for obtaining more realistic results in integration requires that we need to consider numerical methods as was already discussed in Chapter 2.1.1.

In the second model, the pressure distribution p_{sl} caused by sliding motion is given as:

$$p_{sl}(Z, \theta') = \frac{3\eta(\varepsilon\omega - 2\dot{\varepsilon}_t)\sin(\theta')}{c^2[1 - \varepsilon\cos(\theta')]^3} \left(Z^2 - \frac{L^2}{2} \right). \quad (2.27)$$

The dimensionless tangential velocity component $\dot{\varepsilon}_t$ in Equation (2.27) can be written as:

$$\dot{\varepsilon}_t = \frac{1}{c}(-\dot{e}_x \sin(\phi) + \dot{e}_y \cos(\phi)). \quad (2.28)$$

The sliding force components F_{slr} and F_{slt} in radial and tangential directions, respectively, are obtained from integration as:

$$F_{slr} = -R_0 \int_{-\pi}^0 \int_{-\frac{L}{2}}^{\frac{L}{2}} p_{sl}(\theta', Z) \cos(\theta') dZ d\theta', \quad (2.29)$$

$$F_{slt} = -R_0 \int_{-\pi}^0 \int_{-\frac{L}{2}}^{\frac{L}{2}} p_{sl}(\theta', Z) \sin(\theta') dZ d\theta'. \quad (2.30)$$

When obtaining values for the integrals in Equations (2.29) and (2.30), the force components caused by sliding motion can be written as follows:

$$F_{slr} = -\frac{R_0 \eta L^3}{c^2} \frac{\varepsilon (\varepsilon \omega - 2\dot{\varepsilon}_t)}{(1 - \varepsilon^2)^2}, \quad (2.31)$$

$$F_{slt} = \frac{R_0 \eta L^3}{c^2} \frac{\pi (\varepsilon \omega - 2\dot{\varepsilon}_t)}{4(1 - \varepsilon^2)^{\frac{3}{2}}}. \quad (2.32)$$

The force components caused by squeezing of the lubricant film can be treated separately for positive and negative radial velocities. The pressure distribution caused by a squeezing motion p_{sq} is given as:

$$p_{sq}(Z, \theta') = -\frac{6\eta \dot{\varepsilon} \cos(\theta')}{c^2 [1 - \varepsilon \cos(\theta')]^3} \left(Z^2 - \frac{L^2}{2} \right). \quad (2.33)$$

The squeezing force components in the case of positive radial velocity can be obtained from integration as follows:

$$F_{sq_r} = -R_0 \int_{\frac{\pi}{2}}^{\frac{3\pi}{2}} \int_{\frac{L}{2}}^{\frac{L}{2}} p_{sq}(\theta', Z) \cos(\theta') dZ d\theta', \dot{\varepsilon} \geq 0, \quad (2.34)$$

$$F_{sq_t} = -R_0 \int_{\frac{\pi}{2}}^{\frac{3\pi}{2}} \int_{\frac{L}{2}}^{\frac{L}{2}} p_{sq}(\theta', Z) \sin(\theta') dZ d\theta', \dot{\varepsilon} \geq 0, \quad (2.35)$$

where F_{sq_r} is the radial force component and F_{sq_t} is the tangential force component caused by squeezing. For negative radial velocity the squeezing force components can be written as follows:

$$F_{sq_r} = -R_0 \int_{\frac{\pi}{2}}^{\frac{3\pi}{2}} \int_{\frac{L}{2}}^{\frac{L}{2}} p_{sq}(\theta', Z) \cos(\theta') dZ d\theta', \dot{\varepsilon} < 0, \quad (2.36)$$

$$F_{sq_t} = -R_0 \int_{\frac{\pi}{2}}^{\frac{3\pi}{2}} \int_{\frac{L}{2}}^{\frac{L}{2}} p_{sq}(\theta', Z) \sin(\theta') dZ d\theta', \dot{\varepsilon} < 0. \quad (2.37)$$

When obtaining values for the integrals in Equations (2.34) - (2.37), the force components caused by a squeezing motion when positive radial velocity occurs can be written as follows:

$$F_{sq_r} = -\frac{R_0 \eta L^3}{c^2} \frac{\dot{\varepsilon}}{(1-\varepsilon^2)^{\frac{5}{2}}} \left[(\pi - \arccos(\varepsilon)) (1 + 2\varepsilon^2) + 3\varepsilon \sqrt{1-\varepsilon^2} \right], \dot{\varepsilon} \geq 0, \quad (2.38)$$

$$F_{sq_t} = 0, \dot{\varepsilon} \geq 0. \quad (2.39)$$

And, respectively, with negative radial velocity

$$F_{sqr} = -\frac{R_0 \eta L^3}{c^2} \frac{\dot{\varepsilon}}{(1-\varepsilon^2)^{\frac{5}{2}}} \left[(1+2\varepsilon^2) \arccos(\varepsilon) - 3\varepsilon \sqrt{1-\varepsilon^2} \right], \dot{\varepsilon} < 0, \quad (2.40)$$

$$F_{sqt} = 0, \dot{\varepsilon} < 0. \quad (2.41)$$

The bearing force components caused by both phenomena in the rotating coordinates can be written as:

$$\begin{aligned} F_r &= F_{slr} + F_{sqr} \\ F_t &= F_{slt} + F_{sqt} \end{aligned} \quad (2.42)$$

The transformation of forces to the XY -coordinate system can be made using Equation (2.26).

2.4 Long Journal Bearing Model 1

When the L/D ratio is larger than 0.5, the pressure gradient in the circumferential direction becomes significant. In this case the Reynolds equation can be written [23]:

$$\frac{\partial}{\partial x} \left(h^3 \frac{\partial p}{\partial x} \right) + \frac{\partial}{\partial Z} \left(h^3 \frac{\partial p}{\partial Z} \right) = 6\eta R_0 \omega \frac{\partial h}{\partial x}. \quad (2.43)$$

The analytical solution of Equation (2.43) is not available. A common assumption that is made to solve the Reynolds equation for journal bearings is to ignore either the first or second term on the left side of Equation (2.43). The selection of ignored components is based on the bearings L/D -ratio. In the case of a short bearing, the first term is ignored as discussed in chapter 2.1. In the case of a long bearing, the second term is ignored to obtain an approximate solution. It is important to note that this solution ignores the side leakage of the bearing and it assumes that the pressure is constant throughout the length of the bearing. Various approximate methods have been presented in literature, but only two of these solutions are discussed in this study: one introduced by Butenschön [19] and one by Barrett [20]. Firstly, the approximate solution given by Butenschön [19] which is based on the analytical solution of an infinitely short journal

bearing is considered. In this approach, the bearing force equations are modified in terms of Sommerfeld numbers in order to achieve consistency in the numerical solution. The Sommerfeld number is a dimensionless parameter used in lubrication analysis. The bearing force equations can be described by using a Sommerfeld number. In this model the Sommerfeld number used to compute hydrodynamic forces is modified by means of auxiliary polynomials to achieve consistency with the numerical solution of the finite length bearing. A detailed discussion of this method can be found in Reference [19]. In the long bearing model 1, the hydrodynamic force obtained from a sliding motion can be written as [18]:

$$F_{sl} = \frac{\eta LD^3}{4c^2} |\bar{\omega}| So_d, \quad (2.44)$$

where the effective angular velocity $\bar{\omega}$ is given as

$$\bar{\omega} = \omega - 2\dot{\phi}. \quad (2.45)$$

The adjusted Sommerfeld number needed in Equation (2.44) can be written as follows

$$So_d = \left(\frac{L}{D} \right)^2 \frac{\varepsilon}{2(1-\varepsilon^2)^2} \sqrt{\pi^2 (1-\varepsilon^2) + 16\varepsilon^2} \frac{a_1(\varepsilon-1)}{a_2 + \varepsilon}, \quad (2.46)$$

where the adjusting parameters a_1 and a_2 are given by the polynomials

$$a_1 = 1.1642 - 1.9456 \frac{L}{D} + 7.1161 \left(\frac{L}{D} \right)^2 - 10.1073 \left(\frac{L}{D} \right)^3 + 5.0141 \left(\frac{L}{D} \right)^4, \quad (2.47)$$

$$a_2 = -1.000026 - 0.023634 \frac{L}{D} - 0.4215 \left(\frac{L}{D} \right)^2 - \\ 0.038817 \left(\frac{L}{D} \right)^3 - 0.090551 \left(\frac{L}{D} \right)^4. \quad (2.48)$$

The sliding force components in XY -coordinates can be written as follows:

$$F_{slX} = F_{sl} \cos\left(\phi - \chi \frac{|\bar{\omega}|}{\omega}\right), \quad (2.49)$$

$$F_{slY} = F_{sl} \sin\left(\phi - \chi \frac{|\bar{\omega}|}{\omega}\right). \quad (2.50)$$

Angle χ is given by:

$$\chi = \arctan\left(\frac{\pi\sqrt{1-\varepsilon^2}}{2\varepsilon}\right) \sum_{i=1}^5 c_i \varepsilon^{i-1}, \quad (2.51)$$

where the parameters c_i are defined as follows:

$$c_1 = 1.152624 - 0.105465 \frac{L}{D}, \quad (2.52)$$

$$c_2 = -2.5905 + 0.798745 \frac{L}{D}, \quad (2.53)$$

$$c_3 = 8.73393 - 2.3291 \frac{L}{D}, \quad (2.54)$$

$$c_4 = -13.3415 + 3.424337 \frac{L}{D}, \quad (2.55)$$

$$c_5 = 6.6294 - 1.591732 \frac{L}{D}. \quad (2.56)$$

The bearing force obtained from a squeezing motion can be written as follows:

$$F_{sq} = \frac{\eta LD^3}{4c^2} |\dot{\varepsilon}| So_v. \quad (2.57)$$

In Equation (2.57), the adjusted Sommerfeld number, So_v , is given by:

$$So_v = -\left(\frac{L}{D}\right)^2 \frac{4b_1(1-\varepsilon)}{(b_2 + \varepsilon)(1-\varepsilon^2)^{\frac{5}{2}}} \left[\left(\frac{\pi}{2} - \frac{\arccos(\varepsilon)}{2} \right) (1+2\varepsilon^2) + \frac{3}{2} \varepsilon \sqrt{1-\varepsilon^2} \right], \quad (2.58)$$

where the adjusting parameters b_1 and b_2 are given by:

$$b_1 = 0.700380 + 3.2415 \frac{L}{D} - 12.2486 \left(\frac{L}{D} \right)^2 + 18.895 \left(\frac{L}{D} \right)^3 - 9.3561 \left(\frac{L}{D} \right)^4, \quad (2.59)$$

$$b_2 = -0.999935 + 0.0157434 \frac{L}{D} - 0.74224 \left(\frac{L}{D} \right)^2 + \\ 0.42278 \left(\frac{L}{D} \right)^3 - 0.368928 \left(\frac{L}{D} \right)^4. \quad (2.60)$$

The squeezing force components in XY -coordinates can be written as follows:

$$F_{sqX} = F_{sq} \cos(\phi), \quad (2.61)$$

$$F_{sqY} = F_{sq} \sin(\phi). \quad (2.62)$$

The resultant forces in bearing coordinates X, Y can be calculated as

$$F_X = F_{slX} + F_{sqX}, \quad (2.63)$$

$$F_Y = F_{slY} + F_{sqY}. \quad (2.64)$$

2.5 Long Journal Bearing Model 2

This chapter introduces an alternative way of computing hydrodynamic force in the long journal bearing as proposed by Barrett et al. [20]. The solution uses finite length correction factors that extend the short bearing theory to a wider range of bearings L/D -ratios. A detailed derivation of the force equations can be found in Reference [20]. The

non-linear bearing force components in the radial and tangential directions can be written as:

$$F_r = \frac{D^3}{L} \left\{ \frac{1}{g_{r1}^2} \left[1 - \left(\frac{D}{g_{r1}L} \right) \tanh(g_{r1}L/D) \right] \int_{\theta_1'}^{\theta_2'} p_{c1} \cos(\theta') d\theta' + \frac{1}{g_{r2}^2} \left[1 - \left(\frac{D}{g_{r2}L} \right) \tanh(g_{r2}L/D) \right] \int_{\theta_1'}^{\theta_2'} p_{c2} \cos(\theta') d\theta' \right\}, \quad (2.65)$$

$$F_t = \frac{D^3}{L} \left\{ \frac{1}{g_{t1}^2} \left[1 - \left(\frac{D}{g_{t1}L} \right) \tanh(g_{t1}L/D) \right] \int_{\theta_1'}^{\theta_2'} p_{c1} \sin(\theta') d\theta' + \frac{1}{g_{t2}^2} \left[1 - \left(\frac{D}{g_{t2}L} \right) \tanh(g_{t2}L/D) \right] \int_{\theta_1'}^{\theta_2'} p_{c2} \sin(\theta') d\theta' \right\}, \quad (2.66)$$

where the integration limits, θ_1' and θ_2' , represent the boundaries in which the hydrodynamic pressure to be accounted for applies. In this study, the model is modified by means of the circumferential pressure boundaries θ_1' and θ_2' , which are obtained by solving the roots of the pressure equation according the zero-pressure boundary condition. In the original model proposed by Barrett [20], the integration limits are applied according to the Half-Sommerfeld boundary condition with constant integration limits. The dimensionless auxiliary functions g_{r1} , g_{r2} , g_{t1} and g_{t2} in Equations (2.65) and (2.66) can be described as:

$$g_{r1}^2 = \frac{\pi(2+\varepsilon^2)}{\varepsilon^2} \left[1 + \frac{1}{(1-\varepsilon^2)^{1/2}} - \frac{4}{(4-\varepsilon^2)^{1/2}} \right], \quad (2.67)$$

$$g_{t1}^2 = \frac{\pi(2+\varepsilon^2)}{2} \left[\frac{1}{(1-\varepsilon^2)^{1/2}} - \frac{1}{(4-\varepsilon^2)^{1/2}} \right], \quad (2.68)$$

$$g_{r2}^2 = \frac{2}{\varepsilon^2} \left[\pi + \frac{2(\pi - \gamma_1)}{(1-\varepsilon^2)^{1/2}} - \frac{8(\pi - \gamma_2)}{(4-\varepsilon^2)^{1/2}} \right], \quad (2.69)$$

$$g_{t2}^2 = 2 \left[\frac{(\pi - \gamma_1)}{(1-\varepsilon^2)^{1/2}} - \frac{(\pi - \gamma_2)}{(4-\varepsilon^2)^{1/2}} \right]. \quad (2.70)$$

The auxiliary angles, which appear in Equations (2.67)-(2.70), can be written as follows:

$$\gamma_1 = \tan^{-1} \left[\frac{(1-\varepsilon^2)^{1/2}}{\varepsilon} \right], \quad (2.71)$$

$$\gamma_2 = \tan^{-1} \left[\frac{(4-\varepsilon^2)^{1/2}}{\varepsilon} \right]. \quad (2.72)$$

The centreline pressures, p_{c1} and p_{c2} , in Equations (2.65) and (2.66) are caused by the sliding and squeezing effects, respectively. The pressure in the centreline of the bearing can be obtained by setting the axial coordinate Z in Equations (2.27) and (2.33) to zero as follows:

$$p_{c1} = \frac{-3L^2\eta c(\varepsilon\omega - 2\dot{\varepsilon}_t)\sin(\theta')}{4h^3}, \quad (2.73)$$

$$p_{c2} = \frac{3L^2\eta c\dot{\varepsilon}\cos(\theta')}{2h^3}. \quad (2.74)$$

By substituting Equations (2.73) and (2.74) into Equations (2.65) and (2.66), the resulting hydrodynamic forces can be written as follows:

$$\begin{aligned}
F_r = & \frac{D^3}{L} \left\{ \frac{1}{g_{r1}^2} \left[1 - \left(\frac{D}{g_{r1} L} \right) \tanh(g_{r1} L / D) \right] \right. \\
& \left. \frac{(-3\eta c L^2)(\varepsilon\omega - 2\dot{\varepsilon}_r)}{4} \int_{\theta_1^*}^{\theta_2^*} \frac{\sin(\theta') \cos(\theta')}{h^3} d\theta' \right. , \\
& \left. + \frac{1}{g_{r2}^2} \left[1 - \left(\frac{D}{g_{r2} L} \right) \tanh(g_{r2} L / D) \right] \frac{3\eta c L^2 \dot{\varepsilon}}{2} \int_{\theta_1^*}^{\theta_2^*} \frac{\cos(\theta') \cos(\theta')}{h^3} d\theta' \right\} \quad (2.75)
\end{aligned}$$

$$\begin{aligned}
F_t = & \frac{D^3}{L} \left\{ \frac{1}{g_{t1}^2} \left[1 - \left(\frac{D}{g_{t1} L} \right) \tanh(g_{t1} L / D) \right] \right. \\
& \left. \frac{(-3\eta c L^2)(\varepsilon\omega - 2\dot{\varepsilon}_t)}{4} \int_{\theta_1^*}^{\theta_2^*} \frac{\sin(\theta') \sin(\theta')}{h^3} d\theta' \right. . \\
& \left. + \frac{1}{g_{t2}^2} \left[1 - \left(\frac{D}{g_{t2} L} \right) \tanh(g_{t2} L / D) \right] \frac{3\eta c L^2 \dot{\varepsilon}}{2} \int_{\theta_1^*}^{\theta_2^*} \frac{\cos(\theta') \sin(\theta')}{h^3} d\theta' \right\} \quad (2.76)
\end{aligned}$$

Equations (2.75) and (2.76) describe the hydrodynamic forces in a plain journal bearing. In the model proposed by Barrett, the integrals in Equations (2.75)-(2.76) are computed according to the Half-Sommerfeld condition when the force equations take the form:

$$\begin{aligned}
F_r = & \frac{D^3}{L} \left\{ \frac{1}{g_{r1}^2} \left[1 - \left(\frac{D}{g_{r1} L} \right) \tanh(g_{r1} L / D) \right] \frac{(-3\eta L^2)}{2c^2} (\varepsilon\omega - 2\dot{\varepsilon}_r) \frac{\varepsilon}{(1-\varepsilon^2)^2} + \right. \\
& \left. \frac{1}{g_{r2}^2} \left[1 - \left(\frac{D}{g_{r2} L} \right) \tanh(g_{r2} L / D) \right] \frac{3\eta L^2}{2c^2} \frac{\pi(1+2\varepsilon^2)}{2(1-\varepsilon^2)^{5/2}} \dot{\varepsilon} \right\} \quad (2.77)
\end{aligned}$$

$$\begin{aligned}
F_t = & \frac{D^3}{L} \left\{ -\frac{1}{g_{t1}^2} \left[1 - \left(\frac{D}{g_{t1} L} \right) \tanh(g_{t1} L / D) \right] \frac{3\eta L^2}{4c^2} (\varepsilon\omega - 2\dot{\varepsilon}_t) \frac{\pi}{2(1-\varepsilon^2)^{3/2}} + \right. \\
& \left. \frac{1}{g_{t2}^2} \left[1 - \left(\frac{D}{g_{t2} L} \right) \tanh(g_{t2} L / D) \right] \frac{3\eta L^2}{2c^2} \frac{2\varepsilon \dot{\varepsilon}}{(1-\varepsilon^2)^2} \right\} \quad (2.78)
\end{aligned}$$

It is also important to note that the model predicts the behaviour of bearings in a large range of L/D -ratios. The short bearing theory can only be used when the L/D -ratio is

below 0.5; however, accurate results are obtained when the L/D -ratio is below 0.25. In the proposed model, the finite length correction factors introduced by Barrett et. al. [20] extend the short bearing model to cover bearings with L/D -ratios of up to 1.25. For these reasons, the model is more general than other models introduced in this study.

2.6 Comparison and Validation of the Journal Bearing Models

In chapter 2.5, four solutions for non-linear hydrodynamic forces of plain journal bearings were introduced. All the solutions are based on the same theory of solving the Reynolds equation. However, the resulting equations of hydrodynamic forces produce different results due to differences in implementing techniques. The short bearing solutions are simple to apply and they have a clear physical interpretation as compared to the approximate solutions of the long journal bearing. The long journal bearing models can be assumed to be more general solutions because of their ability to capture a wider range of bearing dimensions. All the models compute the non-linear force of the bearing that is an important feature when they are used in simulations of variable situations of the rotor-bearing system. In this chapter, the bearing models are compared. The comparison is carried out by comparing the static characteristics of the bearing model, that is, the load carrying capacity and dynamic characteristics of the bearing model namely the stiffness and the damping. Also, the equations that can be used to calculate the linearized bearing coefficients are presented in this chapter. This is of interest if a simplified linearized model of bearing is used in analysis. In the comparison, the bearing models are referred to by the following abbreviations: the first short bearing model introduced by Vance is SB1, the second short bearing model introduced by Keskiniva is SB2, the first long bearing model introduced by Butenschön is LB1 and the second long bearing model introduced by Barrett is LB2.

2.6.1 Comparison of the Static Characteristics of the Models

Comparison of the static characteristics of models is accomplished by using a simple model that consists of a rigid rotor that is assumed to be ideal. The rotor is supported in the middle and constrained such that it can move in a XY -plane, as shown in Figure 8. The aim of this comparison is to find out the differences between the models when the load carrying capacity of bearings is studied. Three different bearings which vary in

length of the bearings are simulated using the simple model. Bearing variables in the cases studied are shown in Table 1.

Table 1. Bearing dimensions in test cases.

CASE	L [mm]	D [mm]	c [mm]	η [Pa s]	ω [rad/s]
1	25	100	0.01	0.001	100π
2	50	100	0.01	0.001	100π
3	100	100	0.01	0.001	100π

As can be seen in Table 1, the bearing L/D -ratio is varied from 0.25 to 1.0 in order to emphasise the difference in the results obtained from a short bearing and long bearing model.

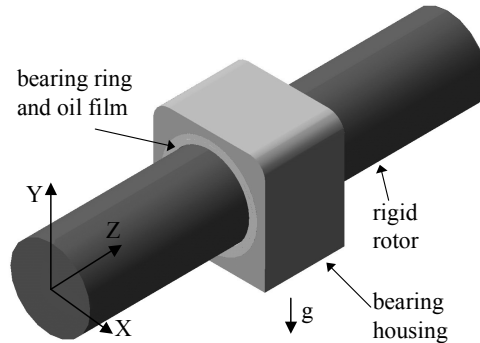


Figure 8. Simulation model of an ideal rotor-bearing system.

The comparison is made by applying a specified load W (rotor mass) and simulating the rotor-bearing system. When the rotor is ideal and perfectly balanced, the rotor obtains a stable position when there are no external forces applied. The eccentricity ratio is obtained from this stable position. When the rotation of the rotor is perfectly stable, there are no radial velocity components and the hydrodynamic force of the bearing is generated completely by a sliding motion. Only one short bearing model, SB1, is included in the comparison of static characteristics. Both short bearing models compute the hydrodynamic force generated by a sliding motion similarly and therefore there is no need to study both of them. The results of the load carrying capacity comparison are

shown in Figures 9-11. The Figures 9-11 present the load carrying capacity of the bearing on the horizontal axis with respect to the eccentricity ratio on the vertical axis.

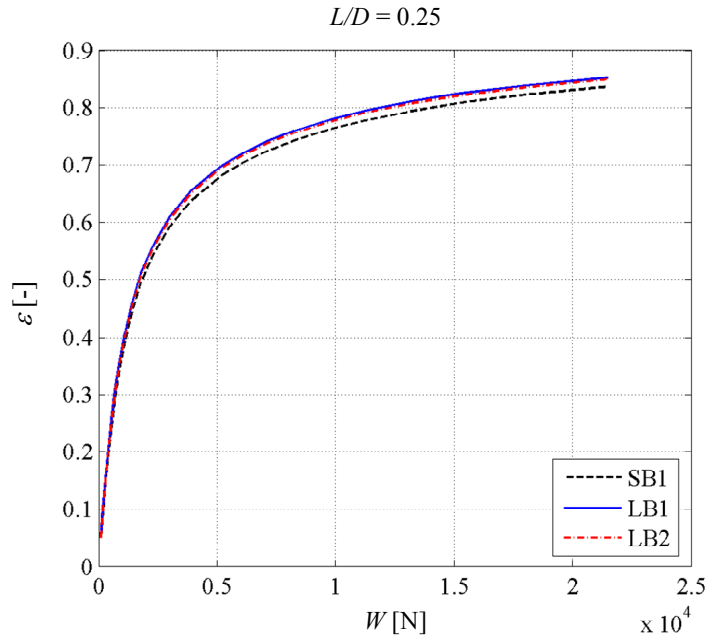


Figure 9. Load carrying capacity according to bearing models when $L/D = 0.25$.

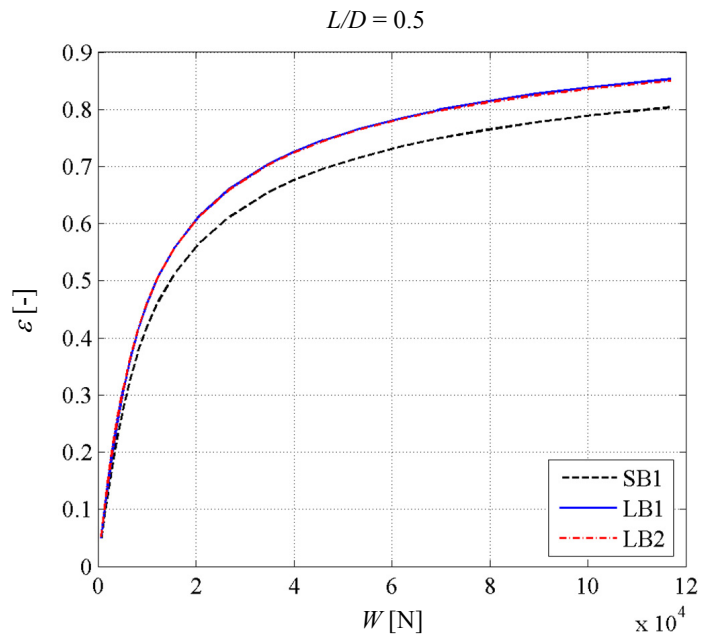


Figure 10. Load carrying capacity according to bearing models when $L/D = 0.5$.

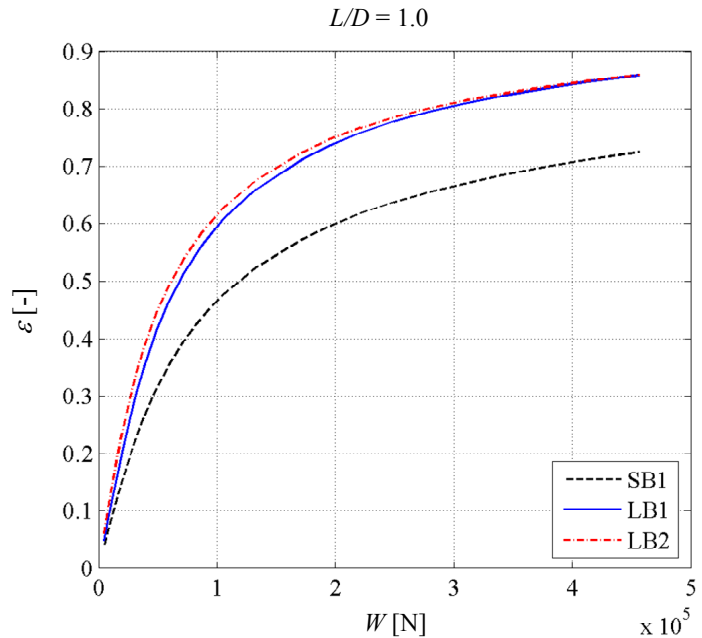


Figure 11. Load carrying capacity according to bearing models when $L/D = 1.0$.

In Figures 9 - 11, it can clearly be seen that the short journal bearing model produces a larger load carrying capacity than the long bearing models when the bearings L/D -ratio increases. In the first case, $L/D = 0.25$, the results agree well with all the models. When the ratio $L/D = 0.5$, a significant difference can be seen in the results obtained from the short and long bearing models. Based on Figures 9 - 11 it can be concluded that the difference becomes larger as the L/D -ratio increases. When considering cases 1-3, both of the long bearing models compute the load carrying capacity very similarly. It can be also concluded that the short bearing model predicts a significantly larger load carrying capacity when the L/D -ratio is 0.5 or larger. The short bearing model predicts approximately a 40% larger load carrying capacity ($\varepsilon = 0.7$) when the L/D -ratio is 0.5 and approximately a 150% larger load carrying capacity ($\varepsilon = 0.7$) when the L/D -ratio is 1.0, in comparison to the long bearing model 2.

2.6.2 Comparison of the Dynamic Characteristics of the Models

A journal bearing can be considered as a spring-damper system with non-linear stiffness and damping coefficients. These coefficients may be linearized if the displacement of the journal is small around the equilibrium position. Based on an experimental study of oil-film dynamic coefficients, Zhou et al. [26] stated that when the excitation amplitude is large, the linear model is invalid. In this study, the comparison of the bearing models' dynamic characteristics is accomplished by computing linearized coefficients. The theoretical background for the computation of bearing coefficients can be found in [1], [17] and [27]. The linearized bearing force components can be written using linearized stiffness and damping coefficients as follows [17]:

$$\Delta F_x = -K_{xx}X - K_{xy}Y - D_{xx}\dot{X} - D_{xy}\dot{Y} \quad (2.79)$$

$$\Delta F_y = -K_{yx}X - K_{yy}Y - D_{yx}\dot{X} - D_{yy}\dot{Y} \quad (2.80)$$

Equations (2.79) and (2.80) describe the force components when displacement and velocity are changed by a differential amount. The linearized coefficients describing the dynamics of the non-linear hydrodynamic bearing can be obtained by applying partial differentiation to the force equations as follows:

$$\begin{aligned} K_{XX} &= \frac{\partial F_X}{\partial e_X} & K_{XY} &= \frac{\partial F_X}{\partial e_Y} \\ K_{YX} &= \frac{\partial F_Y}{\partial e_X} & K_{YY} &= \frac{\partial F_Y}{\partial e_Y} \end{aligned} \quad (2.81)$$

$$\begin{aligned} D_{XX} &= \frac{\partial F_X}{\partial \dot{e}_X} & D_{XY} &= \frac{\partial F_X}{\partial \dot{e}_Y} \\ D_{YX} &= \frac{\partial F_Y}{\partial \dot{e}_X} & D_{YY} &= \frac{\partial F_Y}{\partial \dot{e}_Y} \end{aligned} \quad (2.82)$$

The description of perpendicular force components F_X and F_Y can be obtained as presented previously for each bearing model. In this study, the partial differentiation is carried out numerically in order to obtain the dynamic coefficients.

Figures 12 and 13 show the stiffness coefficient K_{XX} with respect to journal bearing load when the bearing L/D -ratio is 0.25 and 1.0, respectively. It should be noted that the vertical axis is logarithmic. The coefficient is plotted corresponding to each model presented in this study. Again, there are only three graphs in Figures 12 and 13 as in the static studies where the load carrying capacity comparison is examined. The stiffness coefficients are computed using sliding force component as squeezing force component is not dependent on the displacement. Therefore, the coefficients are computed in a similar manner corresponding to both short bearing models and only the results for one short bearing model are depicted.

A common way to present bearing coefficients in literature is to depict dynamic coefficients with respect to the eccentricity ratio. In this case, when comparing coefficients between different models we should bear in mind that different models predict the static equilibrium position differently for certain load condition as can be seen in Figures 9 - 11. Thereby, when comparing the dynamic characteristics computed by different models we should compare them as dynamic characteristics around the respective static equilibrium position. For this reason the coefficients are shown with respect to the load carried by the bearing.

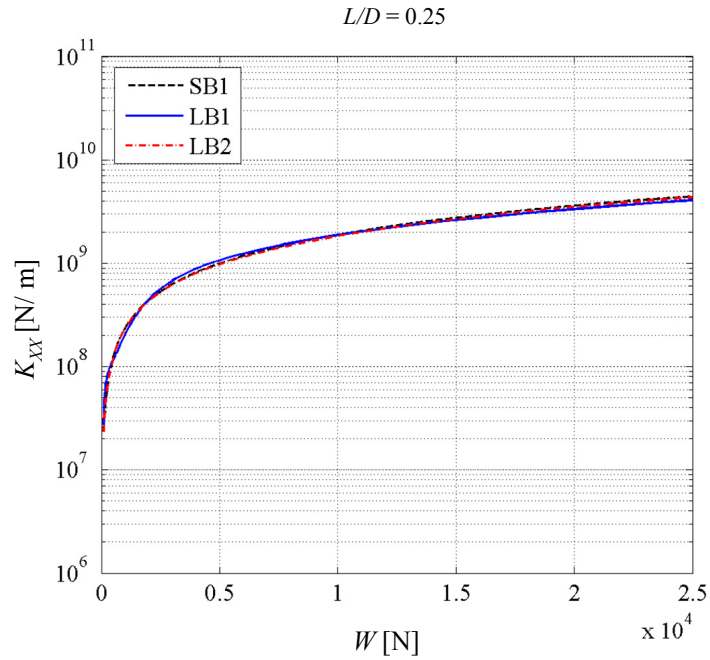


Figure 12. K_{xy} according to the bearing models when $L/D = 0.25$.

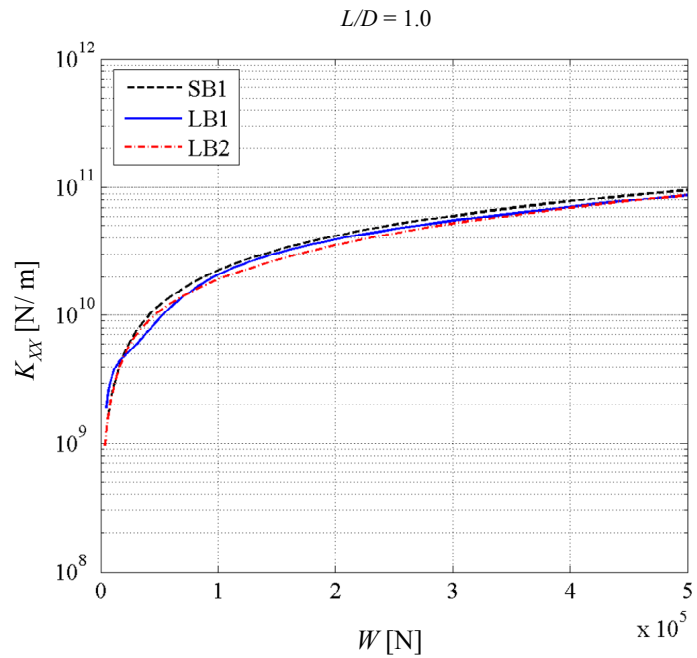


Figure 13. K_{xy} according to the bearing models when $L/D = 1.0$.

It can be seen in Figures 12 and 13 that the models for long and short journal bearings predicts the stiffness coefficient K_{XX} of the bearing quite similarly. The other three coefficients are shown in Appendix A and B. The only stiffness coefficient that has some differences between models is the cross-connection term K_{XY} .

The damping coefficients are presented for all four bearing models. Figures 14 and 15 show the damping coefficient D_{XX} with respect to journal bearing load when the bearing L/D -ratio is 0.25 and 1.0, respectively.

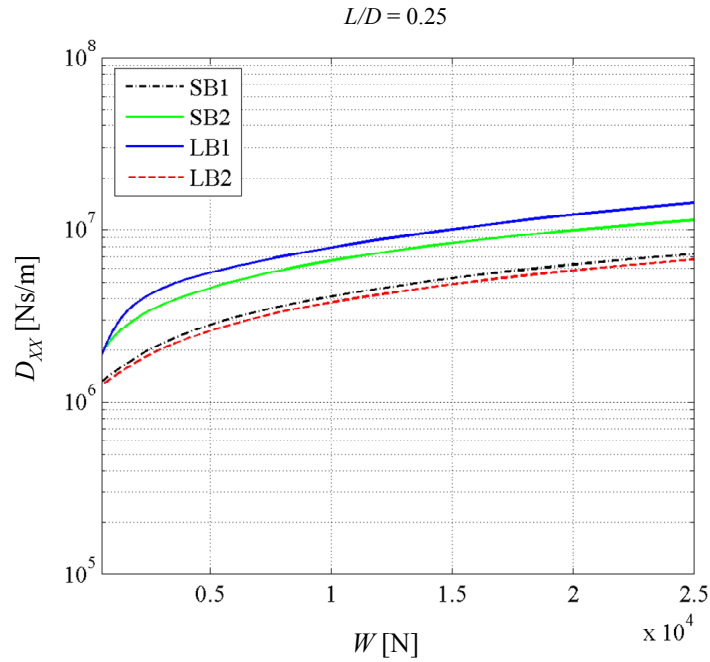


Figure 14. D_{XX} according to the bearing models when $L/D = 0.25$.

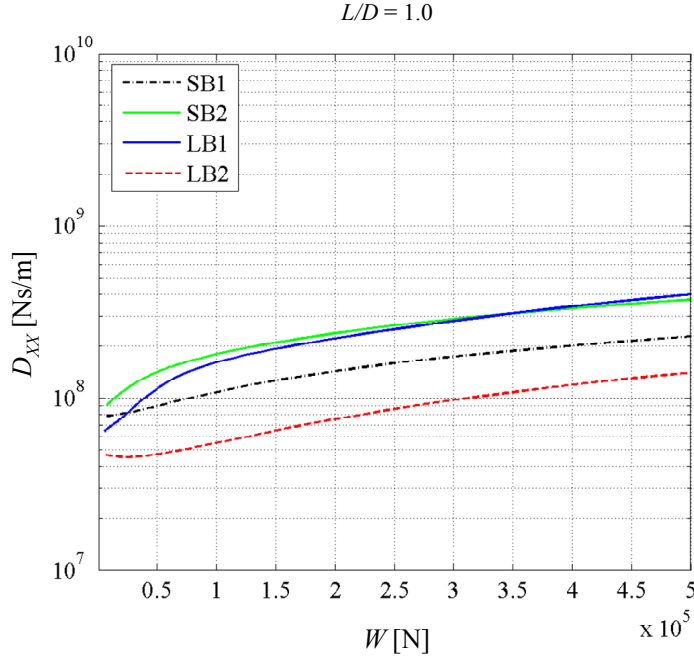


Figure 15. D_{xy} according to the bearing models when $L/D = 1.0$.

It can be seen from Figures 14 and 15 that in terms of the damping coefficient D_{xy} , the bearing models disagree. When considering damping coefficients the differences between models are larger than in the case of stiffness coefficients. The SB1 and LB2 predict most of the coefficients similarly when the L/D-ratio is small. This is expected since LB2 is based on model SB1. In general, LB1 gives the largest values for damping coefficients when looking at Figures 14 and 15 and Appendix C and Appendix D that illustrate the other three damping coefficients. Based on this study it is difficult to state which model gives most correct results for dynamic coefficients. It can nevertheless be stated that there are some differences between the models especially when considering the damping coefficients.

Reference [17] proposes a method to compute the dynamic coefficients analytically for a short journal bearing. The analytic equations give the same results as the numerical computation when model SB1 is considered. In Reference [17], the dimensionless coefficients K'_{ij} and D'_{ij} are given by:

$$K'_{XX} = 4 \left[2\pi^2 + (16 - \pi^2) \varepsilon^2 \right] Q(\varepsilon) \quad (2.83)$$

$$K'_{XY} = \frac{\pi \left[-\pi^2 + 2\pi^2 \varepsilon^2 + (16 - \pi^2) \varepsilon^4 \right]}{\varepsilon (1 - \varepsilon^2)^{1/2}} Q(\varepsilon) \quad (2.84)$$

$$K'_{YX} = \frac{\pi \left[\pi^2 + (32 + \pi^2) \varepsilon^2 + 2(16 - \pi^2) \varepsilon^4 \right]}{\varepsilon (1 - \varepsilon^2)^{1/2}} Q(\varepsilon) \quad (2.85)$$

$$K'_{YY} = \frac{4 \left[\pi^2 + (32 + \pi^2) \varepsilon^2 + 2(16 - \pi^2) \varepsilon^4 \right]}{(1 - \varepsilon^2)} Q(\varepsilon) \quad (2.86)$$

$$D'_{XX} = \frac{2\pi (1 - \varepsilon^2)^{1/2} \left[\pi^2 + 2(\pi^2 - 8) \varepsilon^2 \right]}{\varepsilon} Q(\varepsilon) \quad (2.87)$$

$$D'_{XY} = 8 \left[\pi^2 + 2(\pi^2 - 8) \varepsilon^2 \right] Q(\varepsilon) \quad (2.88)$$

$$D'_{YX} = D'_{XY} \quad (2.89)$$

$$D'_{YY} = \frac{2\pi \left[\pi^2 + 2(24 - \pi^2) \varepsilon^2 + \pi^2 \varepsilon^4 \right]}{\varepsilon (1 - \varepsilon^2)^{1/2}} Q(\varepsilon) \quad (2.90)$$

where

$$Q(\varepsilon) = \frac{1}{\left[\pi^2 + (16 - \pi^2) \varepsilon^2 \right]^{3/2}} \quad (2.91)$$

The dimensional dynamic coefficients can be obtained as follows:

$$K_{ij} = \frac{F}{c} K'_{ij} \quad (2.92)$$

$$D_{ij} = \frac{F}{c\omega} D'_{ij} \quad (2.93)$$

The use of dynamic coefficients can be considered as a simplified approach to describe the journal bearing in a simulation model. The use of coefficients leads to realistic description of bearing responses when there is no need to study the detailed behaviour of the system or non-idealities of the bearings. It is important to note, however, that the use of dynamic coefficients based on linearization is valid only when the displacements of the journal around its equilibrium are small. In this study, coefficients are presented only to show the differences between journal bearing models.

2.6.3 A Validation of the Model for Multibody Simulations

In this section, one of the presented models for the journal bearing is chosen based on its suitability for simulations of the rotor systems in multibody simulation software, such as ADAMS. The model should be appropriate for use in a number of situations, such as rotor run-up over critical speeds of the rotor. In practice, this means that the model needs to be able to describe the non-linear behaviour of the journal bearing. This is due to the fact that the amplitudes of the shaft motion may be large in the simulations. A simulation model of the rotor system may consist of many bodies while some may need to be modelled as flexible bodies. For this reason, the simulation model that describes system mechanics may be computationally time-consuming and therefore expensive. Consequently, the bearing model should be efficient in a computational sense and, therefore, the solutions based on, for example, the FE-method are not considered. On the other hand, the simplest method, that is, the use of dynamic coefficients, is not an acceptable option because of its linear nature.

As shown in the comparison of four bearing models, there is a significant difference between the results of the computed dynamic coefficients and the load carrying capacity obtained from the short and long journal bearing models. The long bearing models are more general as they produce more realistic results in a wider range of bearing L/D -ratios. However, the short bearing theory is widely used and applied in the solution of the Reynolds equation. It is also noteworthy that the physical interpretation of the short bearing theory is more straightforward as compared to semi-analytical models of long

bearings. This gives a good opportunity to develop the model by modifying the pressure equation by including circumferential defects in the bearing bushing or in the shaft journal. The model of the finite length bearing by Barrett [20] is defined by applying the finite length correction factors. The use of correction factors modifies the non-linear bearing forces obtained from the short bearing theory. Barrett et al. compared their model with the analytical solution of finite length journal bearings. They concluded that the correlation with the analytical solution was good even at $L/D = 1.25$. Therefore this model is the most general one to use for modelling bearings of different size. Nevertheless, in this study the measurements from the real structure were performed with a bearing that has $L/D = 0.33$. Bearings with such L/D -ratios are still adequately covered using models of short journal bearings. Generally, short bearing theory operates well with L/D -ratios up to 0.5. Because of the size of the test bearing and issues mentioned above, the SB1 is considered to be most suitable for use in this study and to be developed further. It should also be noted that in the LB2 model the centreline pressure from the short bearing theory is used in the solution of the force equations. For this reason the developed model of short journal bearing including the circumferential defects can be presented in a similar way also with the LB2 model. In Chapter 4.1 the chosen bearing model is verified with the results obtained from literature.

3 NON-IDEALITIES IN JOURNAL BEARING

The journal bearing assembly may consist of a number of non-idealities caused by manufacturing and/or inaccurate installation. Such non-idealities are, for example, waviness of the shaft journal, roughness of the sliding surfaces and misalignment of the bearings. All the non-idealities have an effect on the bearing's behaviour. Choy et al. [28] studied the effects of axial misalignment on the bearing equilibrium position, lubricant fluid film thickness, pressure distribution and stiffness characteristics. They concluded that in light loading, the misalignment results in a double peak in pressure distribution instead of one pressure peak as in the case of a perfectly aligned bearing. The double peak was shown to decrease when the load was increased. They also concluded that the stiffness of the bearing increased as the misalignment increased. Guha [29] studied the steady-state characteristics of a misaligned journal bearing. He concluded that the load carrying capacity of the bearing increases as the misalignment increases due to the increased hydrodynamic pressure. Boyer and Fillon [30] studied experimentally the effects of misalignment on plain journal bearing performance. They concluded that the maximum pressure in the mid-plane of the bearing decreases as the misalignment occurs and the circumferential position of maximum pressure changes. They also noted that the oil flow rate is increased by the misalignment and the minimum film thickness is reduced. Finally, they came to the general conclusion that the effect of the misalignment is more significant when the rotational velocity and load are low and when the hydrodynamic effects are small in such that it is unable to counteract the misalignment.

Based on previous studies it can be stated that misalignment has an effect on journal bearing performance especially when the bearing is lightly loaded and rotational velocity is low. However, misalignment is not expected to produce excitation forces in the system and as this study is focused on the superharmonic vibrations of rotor systems, misalignments are ignored. As presented in chapter 1, non-idealities that excite vibrations have been studied by few authors. The waviness of the shaft journal is a non-ideality that can lead to superharmonic vibrations in which the natural vibration mode of the rotor is excited when the rotational velocity is a fraction of the natural frequency of the rotor-bearing system. In practice, the cross-section of the shaft journal is never

ideally circular. The waviness is present due to inaccuracy in manufacturing. When considering the vibrations of rotor-bearing system, the waviness of the shaft journal should be accounted for. In the proposed model the waviness is included in the equation of bearings film thickness. In the model, the cross-sectional shape of the shaft journal is described using the Fourier cosine series. The Fourier series offers a possibility to describe nearly any function with a sum of cosine and sine terms with proper coefficients [31]. In this case, the waviness of the shaft journal can be described employing cosine terms only in the Fourier series. The shaft journal of a real structure can be measured, for example, in the centre lathe by using a measuring device specially designed for the purpose. The measure device used in this study is named Hybrid (by RollResearch International) [32]. Hybrid uses inductive measuring rods which have an accuracy of 1 μm . The measuring device consists of four measuring rods which enable the separation of the shape of the journal surface from the movement of the journal. When the results are treated with Fast Fourier Transform (FFT) one can obtain a finite number of coefficients that describe the shape of the measured surface. The Fourier cosine series can be used to describe a finite amount of data as an infinite, continuous description as in Equation (3.1).

3.1 Modelling of Waviness of the Shaft Journal

This chapter introduces a method to describe the waviness non-ideality in the journal bearing model. The approach is further developed from the model presented in [24]. The approach presented in [24] was based on introducing the waviness of the shaft journal for the equation of film thickness in pressure Equation (2.17). The agreement of the results of simulation model and measurements from test rig was not perfect and therefore a new approach was considered. In this case the waviness of the shaft journal was introduced to the Reynolds equation.

In the case of an ideal circular shaft journal, the film thickness of the bearing can be written as in Equation (2.4). It can be seen from Equation (2.17), that the film thickness does not depend on the rotation angle of the shaft. However, waviness in the shaft journal leads to a variation in the film thickness when the shaft rotates. Furthermore, variation in the film thickness leads to modified pressure distribution and therefore

affects the hydrodynamic force components of journal bearing. The radius of a non-ideal shaft journal can be described with the help of the Fourier cosine series as follows:

$$R_e = R_0 + \sum_{k=m}^s R_k \cos(k\varphi + \psi_k), \quad (3.1)$$

where R_0 is the nominal radius of the shaft journal and R_k and ψ_k are the amplitude and the phase angle of k^{th} order waviness, respectively. In Equation (3.1), m is the lowest harmonic waviness component to be considered and s is, correspondingly, the highest. In this study, only waviness orders of 2, 3 and 4 are considered, since the amplitudes of higher orders were small in the measurements performed on the test bearing. It is important to point out that the higher waviness orders can be included in a similar manner when necessary. The amplitudes and phase angles of the harmonic components can be obtained from measurements and by analysing the results using FFT. In Equation (3.1), angle φ is the angular coordinate of the shaft journal and can be written as follows:

$$\varphi = \theta - \beta, \quad (3.2)$$

where angle β identifies the journal reference axis (\dot{x}, \dot{y}) orientation with respect to the reference coordinate system of the bearing (X, Y) as can be seen in Figure 3.

By introducing non-ideal shaft journal profile expressed in Equation (3.1) into Reynolds equation as written in Equation (2.3), the effects due to waviness non-ideality can be captured by pressure equation of the journal bearing and furthermore to the hydrodynamic force equations. The Reynolds equation including non-ideal shaft journal profile can be written as:

$$\frac{1}{R_e} \frac{\partial}{\partial \theta} \left(h_e^3 \frac{1}{R_e} \frac{\partial p_e}{\partial \theta} \right) + \frac{\partial}{\partial Z} \left(h_e^3 \frac{\partial p_e}{\partial Z} \right) = 6\eta \left(\frac{1}{R_e} \frac{\partial}{\partial \theta} U_e h_e + 2 \frac{\partial h_e}{\partial t} \right), \quad (3.3)$$

where p_e stands for the pressure in non-ideal bearing assembly. By making the assumption of short journal bearing and dividing the equation by h_e^3 the Reynolds equation can be written as:

$$\frac{\partial^2 p_e}{\partial Z^2} = \frac{6\eta \left(\frac{1}{R_e} \frac{\partial}{\partial \theta} U_e h_e + 2 \frac{\partial h_e}{\partial t} \right)}{h_e^3}, \quad (3.4)$$

where h_e is the film thickness of the journal bearing with non-ideal shaft journal and can be written as:

$$h_e = c_e - e_x \cos(\theta) - e_y \sin(\theta), \quad (3.5)$$

where c_e is the non-ideal radial clearance of the bearing and it can be defined as:

$$c_e = R_b - R_e, \quad (3.6)$$

where R_b is the radius of bearing bushing and R_e radius of shaft journal as described in Equation (3.1). By substituting Equations (3.1) and (3.6) into the Equation (3.5) the film thickness can be written as:

$$h_e = c - \sum_{k=m}^s R_k \cos(k\varphi + \psi_k) - e_x \cos(\theta) - e_y \sin(\theta). \quad (3.7)$$

U_e in Equation (3.4) represents the surface velocity of non-ideal shaft journal and can be written as:

$$U_e = \omega R_e - \dot{e}_x \sin(\theta) + \dot{e}_y \cos(\theta). \quad (3.8)$$

After substitution of R_e the equation takes the following form:

$$U_e = \omega \left(R_0 + \sum_{k=m}^s R_k \cos(k\varphi + \psi_k) \right) - \dot{e}_X \sin(\theta) + \dot{e}_Y \cos(\theta) \quad (3.9)$$

The Reynolds equation for short journal bearing with non-ideal representation of shaft journal shape can be expressed by substituting Equations (3.1), (3.6) and (3.9) to the Equation (3.4) as follows:

$$\begin{aligned} \frac{\partial^2 p_e}{\partial Z^2} &= \frac{6\eta}{\left(c - \sum_{k=m}^s R_k \cos(k\varphi + \psi_k) - e_X \cos(\theta) - e_Y \sin(\theta) \right)^3} \times \\ &\left\{ \frac{1}{R_0 + \sum_{k=m}^s R_k \cos(k\varphi + \psi_k)} \right. \\ &\left. \frac{\partial}{\partial \theta} \left[\left(\omega \left(R_0 + \sum_{k=m}^s R_k \cos(k\varphi + \psi_k) \right) - \dot{e}_X \sin(\theta) + \dot{e}_Y \cos(\theta) \right) \times \right. \right. \\ &\left. \left. \left(c - \sum_{k=m}^s R_k \cos(k\varphi + \psi_k) - e_X \cos(\theta) - e_Y \sin(\theta) \right) \right] + \right. \\ &\left. 2 \frac{\partial}{\partial t} \left(c - \sum_{k=m}^s R_k \cos(k\varphi + \psi_k) - e_X \cos(\theta) - e_Y \sin(\theta) \right) \right\} \end{aligned} \quad (3.10)$$

Equation (3.10) can be solved for pressure equation by integrating it twice with respect to Z . After integration the equation twice with respect to Z the pressure equation can be written as:

$$\begin{aligned}
p_e = & \frac{6\eta}{\left(c - \sum_{k=m}^s R_k \cos(k\varphi + \psi_k) - e_x \cos(\theta) - e_y \sin(\theta) \right)^3} \times \\
& \left\{ \frac{1}{R_0 + \sum_{k=m}^s R_k \cos(k\varphi + \psi_k)} \right. \\
& \frac{\partial}{\partial \theta} \left[\left(\omega \left(R_0 + \sum_{k=m}^s R_k \cos(k\varphi + \psi_k) \right) - \dot{e}_x \sin(\theta) + \dot{e}_y \cos(\theta) \right) \times \right. \\
& \left. \left. \left(c - \sum_{k=m}^s R_k \cos(k\varphi + \psi_k) - e_x \cos(\theta) - e_y \sin(\theta) \right) \right] + \right. \\
& \left. 2 \frac{\partial}{\partial t} \left(c - \sum_{k=m}^s R_k \cos(k\varphi + \psi_k) - e_x \cos(\theta) - e_y \sin(\theta) \right) \right\} Z^2 + C_{1e}Z + C_{2e}
\end{aligned} \tag{3.11}$$

The integration constants C_{1e} and C_{2e} can be solved in a similar way as integration constants C_1 and C_2 , in the case of ideal journal bearing as presented in Chapter 2.1. After solving the integration constants in Equation (3.11) the pressure equation becomes more complicated than in the case of ideal bearing and it can not be presented explicitly. The calculation is performed by using commercial calculation tool MapleTM from Maplesoft. The Fortran code is used in ADAMS to calculate the bearing forces as described above. Furthermore, the bearing model is built up as a subroutine in ADAMS that is called each time step.

By taking the shaft journal waviness into account the pressure equation in respect to circumferential coordinate, is no longer defined only by trigonometric functions as described in chapter 2.1.1 for the case of ideal bearing. It is noteworthy that the negative and positive pressure regions differ from the ideal case. In the ideal journal bearing model, the pressure field is equally divided in the negative and positive pressure sections that both have length of π radians in the direction of circumferential coordinate θ . However, in the case of non-ideal journal bearing the position is different as can be seen in Figure 16.

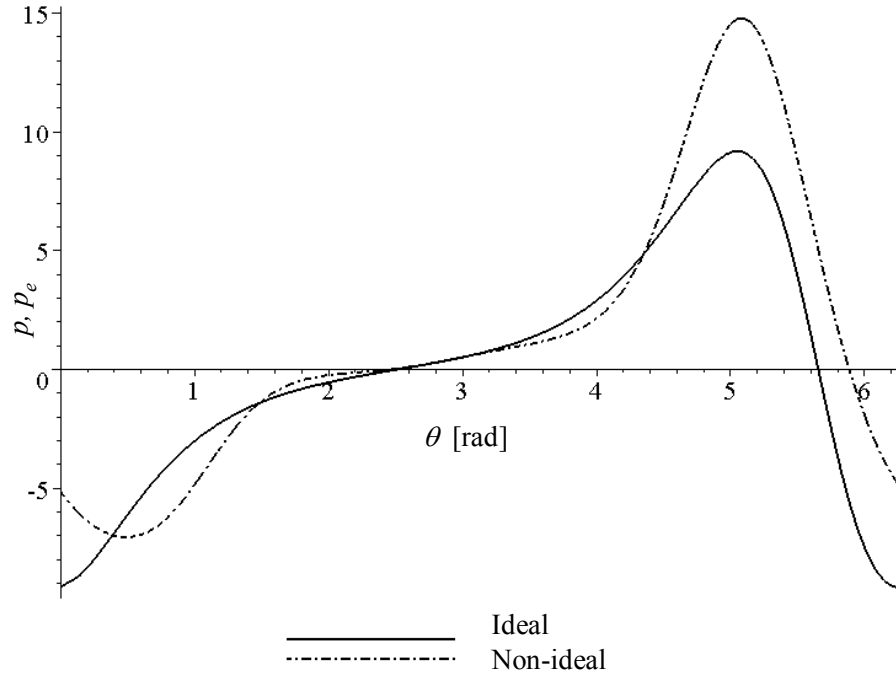


Figure 16. Pressure distribution according to circumferential coordinate in case of ideal and non-ideal shaft journal.

As can be seen in Figure 16 the non-ideal pressure distribution differs from the ideal one. It is important to note that the shape of the pressure curve and the position of pressures zero-point changes while the shaft journal rotate.

Due to the complex pressure equation of the non-ideal bearing, the closed form integration is not available when computing bearing force components contrary to the ideal bearing model. Still, the solution can be provided by means of numerical integration methods such as Midpoint rule, Simpson's rule etcetera. For the curve shapes that represent non-ideal bearing distribution the both mentioned methods offers accurate results with reasonable number of steps. In computation, the numerical method used for integration is Midpoint rule [33], [34].

In the integration of the pressure field, the aim is to utilize the region in the oil film where pressure has positive values. In this sense, the approach resembles the Half-

Sommerfeld boundary condition. In the case of ideal shaft journal, the condition of positive pressure can be fulfilled with methods presented earlier in Chapter 2.1.1. However, in the case of non-ideal shaft journal the length of positive pressure region varies as the shaft journal rotates. At some point the positive region is longer than π radians and at some point the region is shorter than π radians.

The correct boundaries for integration can be obtained by monitoring the pressure equation for each integration step. The numerical integration is performed over the whole circumferential coordinate $\theta = 0..2\pi$. During each step of numerical integration with each value of θ the pressure equation is solved and the sign is verified. If the sign is positive, the respective numerical integration section is accounted for and to the contrary with negative sign the respective integration section is ignored in the computation of the hydrodynamic bearing force components.

3.2 Modelling of Waviness of the Bearing Bushing

Modelling of the waviness of bearing bushing that may exist in journal bearing is presented in this chapter. Defects of non-rotating part of journal bearing assembly, such as the waviness of bearing bushing, do not excite vibrations. However, this shape error has an effect on oil film thickness and therefore on the dynamic behaviour of the bearing as was stated for example by Rasheed [14].

The waviness of bearing bushing can be taken into account by introducing the non-ideal radius of bearing bushing in Equation (3.6). The non-ideal radius of bearing bushing can be written as:

$$R_{be} = R_{b0} + \sum_{k=m}^s R_{bk} \cos(k\theta + \psi_{bk}) \quad (3.12)$$

where R_{b0} is the nominal radius of bearing bushing, R_{bk} and ψ_{bk} are the amplitude and the phase angle of k^{th} order waviness, respectively. By substituting R_b in Equation (3.6) with R_{be} , the equation for journal bearing radial clearance can be written as follows:

$$c_e = R_{b0} + \sum_{k=m}^s R_{bk} \cos(k\theta + \psi_{bk}) - R_e \quad (3.13)$$

Furthermore, by substituting the non-ideal presentation of shaft journal radius from Equation (3.1) into Equation (3.13), the expression of film thickness that takes into account both the waviness in shaft journal and waviness in bearing bushing can be written as follows:

$$h_{be} = c + \sum_{k=m}^s R_{bk} \cos(k\theta + \psi_{bk}) - \sum_{k=m}^s R_k \cos(k\varphi + \psi_k) - e_x \cos(\theta) - e_y \sin(\theta) \quad (3.14)$$

By substituting Equation (3.14) into the Reynolds equation in similar manner as described in chapter 3.1, the pressure equation for hydrodynamic journal bearing with non-ideal shape of shaft journal and bearing bushing can be solved.

In Figure 17, a graphical presentation of non-ideal shaft journal and bearing bushing is depicted. In both parts only the 2nd order waviness component of equal size is included.

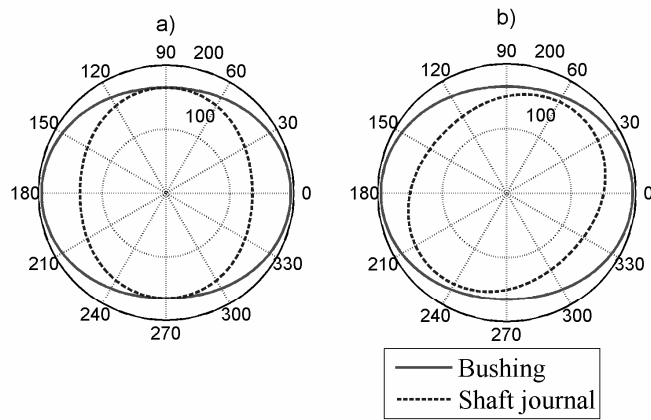


Figure 17. A graphical presentation of exaggerated waviness of the shaft journal and bearing bush, (a) $\psi_{b2} = \psi_2 = 0$, (b) $\psi_{b2} = 0$ and $\psi_2 = \frac{\pi}{2}$.

4 NUMERICAL EXAMPLES

The proposed journal bearing model is implemented into a commercial multibody simulation software application (MSC.ADAMS [35]) by employing the equations introduced in the previous chapter. The model is used to analyse the dynamic response of a rotor system in which the journal bearing is measured to be non-ideal. In the first part of this chapter, a simple rigid rotor with two degrees of freedom supported by one journal bearing is studied. In the second part, a detailed model of a roll tube supported with two journal bearings is studied. The model of the roll tube describes the test rig that was used in measurements of non-idealities. The detailed model of the roll tube is verified using the measurement results of the test rig.

4.1 A Rigid Rotor with Journal Bearing

In general, non-linear behavior must be considered if the system operates in a non-linear region. A non-linear system can be described by using linear equations provided that changes of non-linear variables are insignificant during the operation. For example, a non-linear mass-spring system can be described with a linear spring coefficient if the displacement during operation is small enough that spring force changes linearly with respect to displacement. The hydrodynamic force produced by journal bearing is highly non-linear with respect to displacement of the journal. In this chapter, the linear and non-linear bearing models are compared by means of simple rotor system with two degrees of freedom in order to shed light on the capabilities of nonlinear bearing models.

The example presented in this chapter consists of a rigid rotor described by two degrees of freedom that are translations in X- and Y-directions as presented in Figure 18. In this example, rotation velocity about Z-axis is assumed to be constant. The numerical results of different models are computed by using similar system parameters as explained in [36]. The linear model is computed by using a Matlab from The Mathworks Inc. The results are compared to the results presented in [36] for the linear computation. The results from linear model are also compared to the results computed in ADAMS environment in which the non-linear model is employed. It is important to reiterate that

the purpose of this chapter is to verify the non-linear simulation model built up in ADAMS with the results presented in [36].

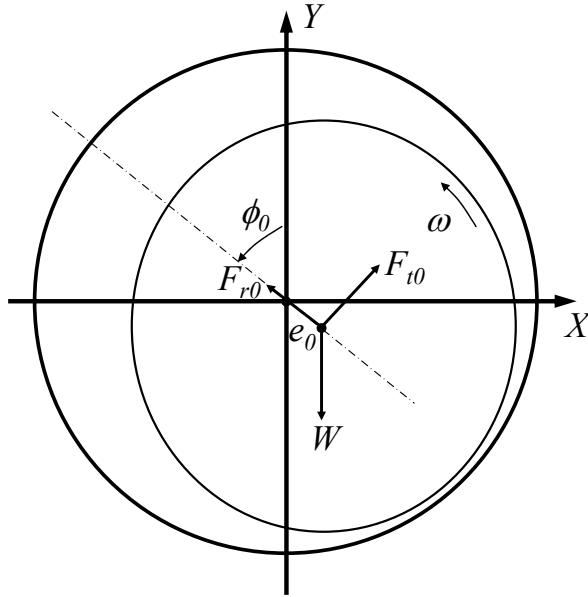


Figure 18. Plain cylindrical journal bearing in equilibrium position.

4.1.1 The computation of linearized responses

The equations of motion for a rigid rotor with a linear bearing can be written as follows:

$$\begin{bmatrix} M & 0 \\ 0 & M \end{bmatrix} \begin{bmatrix} \ddot{X} \\ \ddot{Y} \end{bmatrix} + \begin{bmatrix} D_{XX} & D_{XY} \\ D_{YX} & D_{YY} \end{bmatrix} \begin{bmatrix} \dot{X} \\ \dot{Y} \end{bmatrix} + \begin{bmatrix} K_{XX} & K_{XY} \\ K_{YX} & K_{YY} \end{bmatrix} \begin{bmatrix} X \\ Y \end{bmatrix} = \begin{bmatrix} F_{Xu} \\ F_{Yu} \end{bmatrix}, \quad (4.1)$$

where M is mass of the rigid rotor. D_{ij} and K_{ij} are the linearized damping and stiffness coefficients of the journal bearing, respectively. X and Y are the displacements of the rotor in fixed coordinate system. F_{Xu} and F_{Yu} are the excitation force components due to mass unbalance as described in Equation (4.11). Note that in the computing of the linearized model, the displacements (X, Y) are assumed to be small with respect to static equilibrium position not respect to centre of the bearing.

In order to obtain closed form solutions for the linearized coefficients, a rotating coordinate system is used. The rotating coordinate system is used in a similar manner as in Chapter 2.2 when solving analytically the bearing forces based on assumption of short journal bearing.

The static equilibrium of the journal bearing can be solved by setting journal bearing resultant forces in rotating coordinates equal to externally applied forces as follows:

$$F_{r0} = -W \cos(\phi_0) \quad (4.2)$$

$$F_{t0} = W \sin(\phi_0), \quad (4.3)$$

where W is the static load of the journal bearing. The static load is due to gravity and it applies in Y -direction. In Equations (4.2) and (4.3), ϕ_0 is the attitude angle of the journal in static equilibrium position e_0 , as depicted in Figure 18. F_{r0} and F_{t0} are the radial and tangential hydrodynamic force components of the bearing in static equilibrium position and they can be written employing short bearing theory by setting the translational velocity components to be zero and using static equilibrium eccentricity ratio as well as attitude angle for journal position in Equations (2.20) and (2.21) as follows:

$$F_{r0} = -\eta R_0 L \left(\frac{L}{c} \right)^2 \left[\frac{\omega \varepsilon_0^2}{\left(1 - \varepsilon_0^2 \right)^2} \right] \quad (4.4)$$

$$F_{t0} = \eta R_0 L \left(\frac{L}{c} \right)^2 \left[\frac{\omega \pi \varepsilon_0}{4 \left(1 - \varepsilon_0^2 \right)^{3/2}} \right] \quad (4.5)$$

By substituting the hydrodynamic force components Equations (4.4) and (4.5) into Equations (4.2) and (4.3) the static equilibrium position can be defined as follows [36]:

$$\frac{\eta R_0}{2} \left(\frac{L}{c} \right)^3 \left(\frac{\omega \varepsilon_0 c}{W} \right) \left[\frac{\sqrt{16\varepsilon_0^2 + \pi^2 (1-\varepsilon_0^2)}}{2(1-\varepsilon_0^2)^2} \right] = 1 \quad (4.6)$$

and

$$\tan(\phi_0) = \frac{\pi \sqrt{1-\varepsilon_0^2}}{4\varepsilon_0} \quad (4.7)$$

The static equilibrium eccentricity ratio can be solved from Equation (4.6) using, for example, Newton-Raphson iteration method [33]. By using the solved eccentricity ratio, the attitude angle can be solved from Equation (4.7).

Bearing forces can be calculated based on linearized bearing coefficients as described in equations of motion defined in Equation (4.1). In general, the linearized bearing coefficients can be obtained by calculating the partial derivatives of force components in static equilibrium position as explained in chapter 2.6.2. When computing coefficients according to the short bearing theory, it is possible to find analytical equations for radial and tangential coefficients as follows [36]:

$$\begin{bmatrix} K_{rr} & K_{rt} \\ K_{tr} & K_{tt} \end{bmatrix} = \frac{\eta R}{2} \left(\frac{L}{c} \right)^3 \omega \begin{bmatrix} \frac{4\varepsilon_0 (1+\varepsilon_0^2)}{(1-\varepsilon_0^2)^3} & \frac{\pi}{2(1-\varepsilon_0^2)^{3/2}} \\ \frac{-\pi (1+2\varepsilon_0^2)}{2(1-\varepsilon_0^2)^{5/2}} & \frac{2\varepsilon_0}{(1-\varepsilon_0^2)^2} \end{bmatrix} \quad (4.8)$$

$$\begin{bmatrix} D_{rr} & D_{rt} \\ D_{tr} & D_{tt} \end{bmatrix} = \frac{\eta R}{2} \left(\frac{L}{c} \right)^3 \begin{bmatrix} \frac{\pi (1+2\varepsilon_0^2)}{(1-\varepsilon_0^2)^{5/2}} & \frac{-4\varepsilon_0}{(1-\varepsilon_0^2)^2} \\ \frac{-4\varepsilon_0}{(1-\varepsilon_0^2)^2} & \frac{\pi}{(1-\varepsilon_0^2)^{3/2}} \end{bmatrix} \quad (4.9)$$

The coordinate transformation of radial and tangential coefficients to XY-coordinate system can be performed in similar manner to both stiffness and damping coefficients as follows:

$$\begin{bmatrix} K_{XX} & K_{XY} \\ K_{YX} & K_{YY} \end{bmatrix} = \begin{bmatrix} \sin(\phi_0) & \cos(\phi_0) \\ -\cos(\phi_0) & \sin(\phi_0) \end{bmatrix} \begin{bmatrix} K_{rr} & K_{rt} \\ K_{tr} & K_{tt} \end{bmatrix} \begin{bmatrix} \sin(\phi_0) & -\cos(\phi_0) \\ \cos(\phi_0) & \sin(\phi_0) \end{bmatrix} \quad (4.10)$$

The right side of the equations of motion defined in Equation (4.1) describes the harmonic forces acting in the journal. In the studied case, forces are due to mass unbalance. Figure 19 depicts the centrifugal force caused by the unbalance mass, m_u , which is located at distance e_u from the Z-axis, that is, the rotating axis.

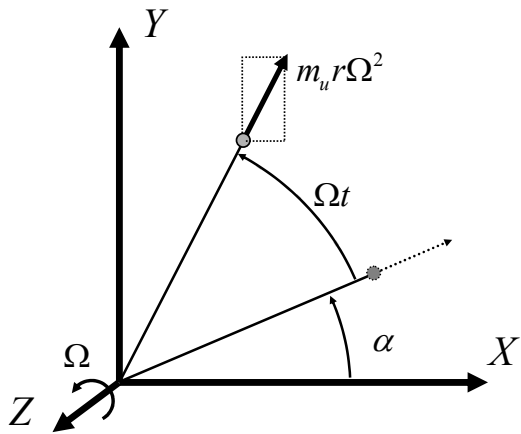


Figure 19. Definition of unbalance mass and its centrifugal force.

Components of the unbalancing force in Equation (4.1) can be written as follows [37]:

$$\begin{bmatrix} F_{Xu} \\ F_{Yu} \end{bmatrix} = m_u e_u \omega^2 \begin{bmatrix} \cos(\omega t + \tau) \\ \sin(\omega t + \tau) \end{bmatrix} \quad (4.11)$$

Using the following trigonometric equalities,

$$\cos(\omega t + \tau) = \cos(\omega t) \cos(\tau) - \sin(\omega t) \sin(\tau) \quad (4.12)$$

$$\sin(\omega t + \tau) = \sin(\omega t)\cos(\tau) + \cos(\omega t)\sin(\tau) \quad (4.13)$$

Equation (4.11) can be written as:

$$\begin{bmatrix} F_{Xu} \\ F_{Yu} \end{bmatrix} = m_u e_u \omega^2 \begin{bmatrix} -\sin(\tau) \\ \cos(\tau) \end{bmatrix} \sin(\omega\tau) + m_u e_u \omega^2 \begin{bmatrix} \cos(\tau) \\ \sin(\tau) \end{bmatrix} \cos(\omega\tau) \quad (4.14)$$

By identifying the time-independent force components the unbalance force vectors, \mathbf{F}_s and \mathbf{F}_c , can be written as follows:

$$\mathbf{F}_s = m_u e_u \omega^2 \begin{bmatrix} -\sin(\tau) & \cos(\tau) \end{bmatrix}^T \quad (4.15)$$

$$\mathbf{F}_c = m_u e_u \omega^2 \begin{bmatrix} \cos(\tau) & \sin(\tau) \end{bmatrix}^T \quad (4.16)$$

Equations of motion can be rewritten as follows:

$$\mathbf{M}\ddot{\mathbf{x}} + \mathbf{D}\dot{\mathbf{x}} + \mathbf{K}\mathbf{x} = \mathbf{F}_s \sin(\omega t) + \mathbf{F}_c \cos(\omega t), \quad (4.17)$$

where \mathbf{M} is the mass matrix of the rigid rotor, \mathbf{D} is the linearized damping matrix of the supporting bearing and \mathbf{K} is the linearized stiffness matrix of the supporting bearing. \mathbf{x} is the displacement vector of the rigid rotor and the solutions for that are sought in the form

$$\mathbf{x} = \mathbf{x}_s \sin(\omega t) + \mathbf{x}_c \cos(\omega t), \quad (4.18)$$

where \mathbf{x}_s and \mathbf{x}_c are the vectors representing the response components. By solving the first and second time derivative of Equation (4.18) and substituting them into Equation (4.17) and identifying $\sin(\omega t)$ and $\cos(\omega t)$ terms, the following equation can be obtained [37]:

$$\begin{bmatrix} \mathbf{K} - \mathbf{M}\omega^2 & -\omega\mathbf{D} \\ \omega\mathbf{D} & \mathbf{K} - \mathbf{M}\omega^2 \end{bmatrix} \begin{bmatrix} \mathbf{x}_s \\ \mathbf{x}_c \end{bmatrix} = \begin{bmatrix} \mathbf{F}_s \\ \mathbf{F}_c \end{bmatrix} \quad (4.19)$$

This linear system of equations can be solved for given values of ω , and the obtained results, $\mathbf{x}_s(\omega)$ and $\mathbf{x}_c(\omega)$, can be used to calculate the displacement vector \mathbf{x} according to Equation (4.18).

4.1.2 Comparison between linear and non-linear models

In the first studied cases, the non-linear bearing model that is used in development of the model that accounts the non-idealities is compared to the results presented in [36]. The results presented in [36] are computed by solving the Reynolds equation and using the short bearings assumption. When carrying out the integration of the pressure equation the circumferential boundary condition was the Reynolds boundary condition in [36]. Furthermore, in the axial direction the boundary condition was that pressure is zero on both sides of the bearing. Secondly, the results obtained from linear model are compared with the non-linear bearing model in different operation conditions. In this section, linear model is solved using Matlab code while non-linear model is calculated using ADAMS software.

The physical parameters of the system are similar to the example that is presented in [36]. In the studied case, L/D -ratio is 0.25 which justifies the use of the short bearing theory.

Table 2. Parameters of the simulated system

Properties of rigid rotor		Bearing properties	
Mass	22.680 kg (5.0986 Lbs)	Inner diameter	50.8 mm (2.0 in)
Unbalance mass configurations		Length	12.7 mm (0.5 in)
$e_u = 25$ mm, $m_u = 2.880$ g (0.1oz-in)		Radial clearance	0.0508 mm (0.002 in)
$e_u = 25$ mm, $m_u = 5.761$ g (0.2oz-in)		Viscosity of the oil	6.8948E-3 Pas (1.0E-6 Re却ns)
$e_u = 25$ mm, $m_u = 14.402$ g (0.5oz-in)			
$e_u = 25$ mm, $m_u = 28.803$ g (1.0oz-in)			

In the first comparison, seven different cases are studied including three cases without unbalance using rotational velocities of 4000 rpm, 10000 rpm and 12000 rpm and four cases with different unbalance configurations as described in Table 2. In the unbalance cases, the used rotational velocity is 4000 rpm. The comparison with the linear model is performed using the latter 4 cases with different unbalances. The displacement results are given in units [inch] instead of [mm] that are otherwise used in this study. The units are changed to simplify the comparison to [36]. Results for the first three studied cases are presented in Figures 20 and 22.

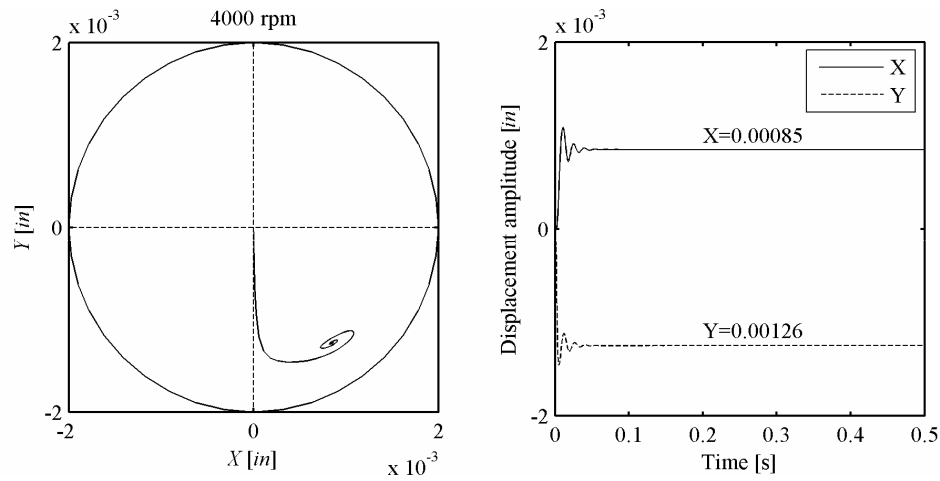


Figure 20. Results from non-linear model with rotational velocity 4000 rpm, no unbalance.

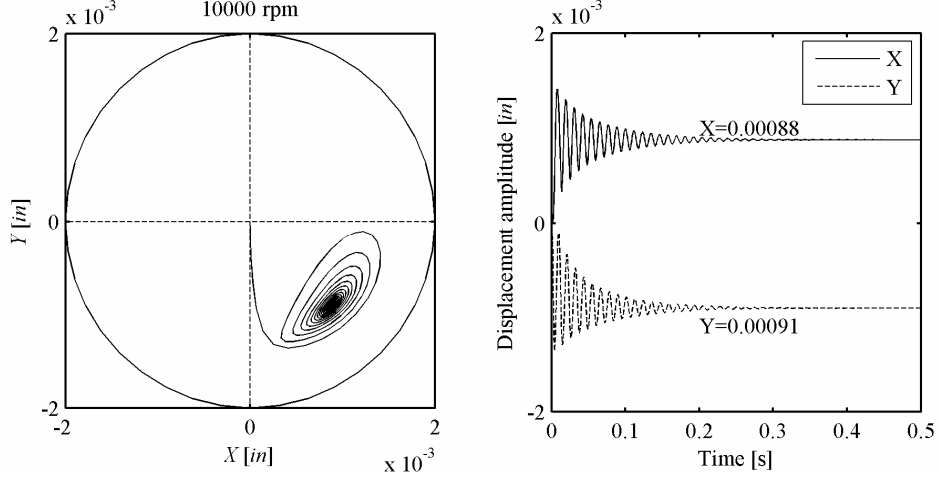


Figure 21. Results from non-linear model with rotational velocity 10000 rpm, no unbalance.

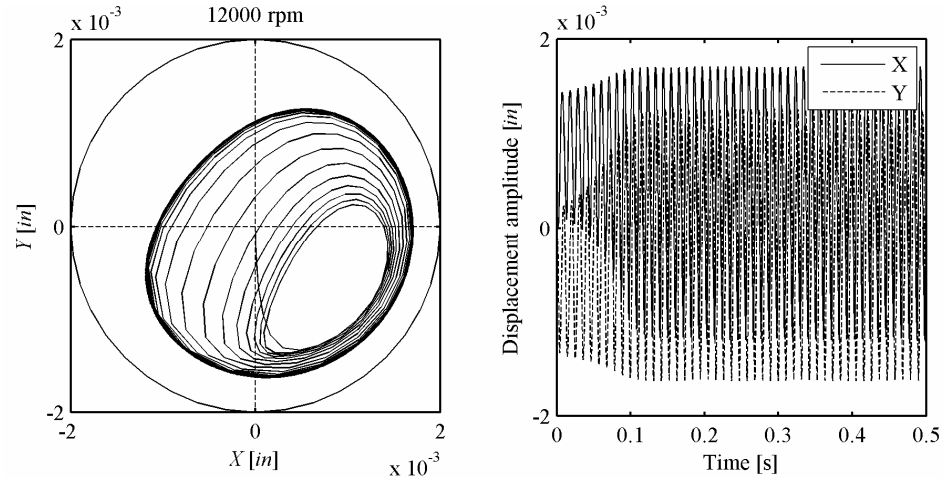


Figure 22. Results from non-linear model with rotational velocity 12000 rpm, no unbalance.

The results shown in Figures 20 - 22 agree with the results presented in [36]. The results of the non-linear model without unbalance presented in [36] are shown in Appendix E. As the equilibrium positions coincident in two different results, the load carrying capacity of the bearing calculated using different models agree. Further, the vibrations of the rotor before reaching the equilibrium position are similar. Accordingly, the

damping calculated using the two models are the same. As can be seen in Figure 22, the journal whirls around the equilibrium position when rotational velocity is 12000 rpm even when no external forces acting to the journal. This phenomenon is called oil-whirl, that is, self-excitation in journal bearing. The frequency analysis shows that the whirling frequency is 95.2 Hz, that is, 5713 rpm, which is the same whirling frequency that is reported in [37]. The whirling frequency is often referred to as half-whirling frequency as it is close to the half rotational velocity. The results of frequency analysis of journal displacement components are shown in Figure 23.

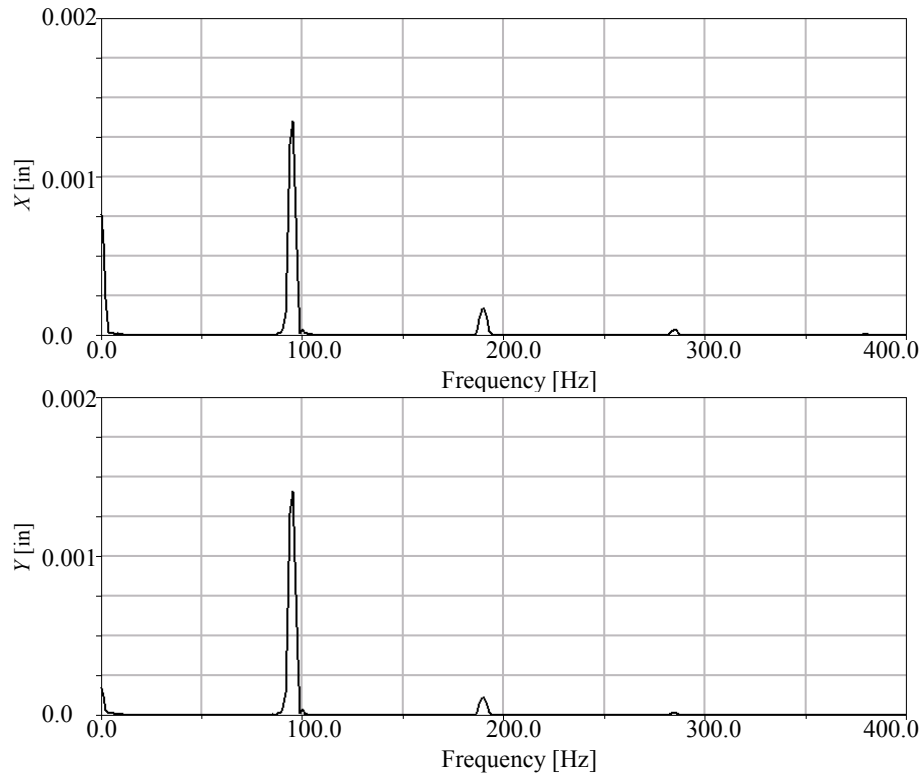


Figure 23. FFT of displacement components at rotational velocity 12000 rpm, no unbalance.

Figure 24 shows the results based on the non-linear model with four different unbalances. Additionally the same system is computed using the linearized model. Also these results are shown in Figure 24.

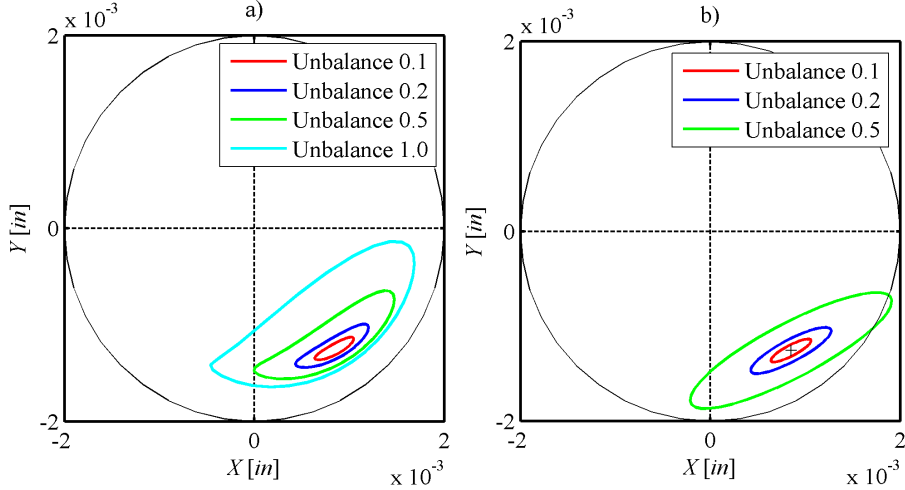


Figure 24. Results based on (a) non-linear model and (b) linear model with unbalances.

As can be seen in Figure 24 (a), the orbits agree with the one presented in [36]. The results of the non-linear and the linear model with different unbalances presented in [36] are shown in Appendix F. The similar displacement amplitudes of the rotor can be interpreted in such that the stiffness and damping of the bearing computed by different models agrees. Furthermore, the similar shapes of the orbits, particularly with high unbalance, are due to comparable non-linear behavior of different models.

As can be seen in Figure 24 (a), the shapes of orbits are nearly elliptical for small unbalance while they become more complicated with large unbalance. It is noteworthy that the orbit size does not increase linearly with respect to the unbalance as the linear theory predicts. FFT-analysis of responses with unbalancing force shows that the rotor oscillates around its equilibrium position with synchronous (1X) vibration amplitude when unbalance is small. In cases of large unbalance (0.5 and 1.0), the superharmonic (2X) vibration components become visible in FFT-analysis. This is due to non-linear behavior of the bearing which introduces the non-elliptical orbit with large amplitudes.

When comparing the results from the linear model, Figure 24 (b), with the results of linear model presented in [36] again the results agree. However, a small difference in the amplitudes of the responses can be noticed. Since the exact numerical values of results are not presented in [36], it is cumbersome to analyse accurately the source of

the discrepancy. One explanation could be that in reference [36], an erroneous equation for computing the damping coefficients of the bearing was used. In reference [36] the equation to calculate damping coefficient described in Equation (4.9) is multiplied by angular velocity ω that is not correct.

When comparing Figure 24 (a) with (b), the difference between results from the non-linear and the linear model can be seen clearly. In the case of small unbalance the orbit shapes are similar. However, in cases of larger unbalance (unbalance 0.5) the linear theory predicts an overly large response.

As explained in the beginning of this chapter the non-linear behavior should be considered in some cases. Accordingly, as shown with the results from linear and non-linear bearing models, the linear model predicts incorrect results if the operation takes place in non-linear regime. When designing rotor-bearing systems, the main interest is in locations of critical speeds and system instability threshold. These focuses of interest can be addressed by the linear analysis. However, there are several situations such as large vibration amplitudes of the rotor and operation near and beyond the instability threshold when the non-linear model should be used. It is noteworthy that excitation forces produced by non-idealities of the bearing, such as the waviness of the shaft journal, can lead to large vibration amplitudes of the rotor. If, for example, the translational movement of the rotor needs to be investigated in an accurate manner, the linear theory may not produce a satisfactory result. As explained in the examples, the journal orbit tends to increase when unbalance increases. The linear theory predicts the output (response) to increase linearly relative to input (force) which is not according to nature. For example, the case of large unbalance configuration (unbalance = 0.5) the linear model predicts the orbit to be outside of the bearing bushing which is not physically possible. It was also seen that, in some cases, the non-linear behavior of the bearing may excite the rotor vibration even if there is no non-idealities present in the system. Near the instability threshold the bearing starts to generate sub-harmonic excitation, whose frequency is about half of the whirling frequency of the rotor. In the case of large unbalance, the non-linear behavior of the oil film may also introduce a superharmonic (2X) vibration component. The computation of the non-linear model that was used in examples of rigid rotor takes about 8 seconds in the simulation of 1 second

with 1 ms time step. For this reason, it can be concluded that the non-linear bearing model is not computationally expensive enough to justify the use of linear model.

The aim in this study is to introduce a method to take into account the excitations that take place due to waviness of the shaft journal. It is meaningful to use non-linear model as basis for the model development to reduce the number of uncertainties acting in the simulation model. By linearizing the bearing model, an additional simplification as well as uncertainty would be added to the simulation model. The bearing model used in this study can describe non-linear behavior of oil film forces and can therefore be used to simulate various situations in a rotor-bearing system.

4.2 A Simulation Model of a Roll Tube Supported by Plain Journal Bearings

Traditionally, the calculation of rotor dynamics is covered mainly by computing natural frequencies and stability of the rotor systems [7]. The responses of rotor systems can be also calculated using multibody simulation approach which is a general procedure for dynamic analysis of mechanical systems. The traditional methods are usually based on certain simulation models that are derived with simplifying assumptions. Such assumptions lead to models that may operate only on restricted conditions such as under the assumption of constant rotational velocity. Simplified models may not take into account non-idealities in the system that can excite the system natural frequencies and, accordingly, affect the natural frequency of the system. Such features are for example bearing clearance and waviness in shaft journal and in bearing bushing. Multibody simulation have been previously found out to be an effective tool for simulating dynamics of different rotor systems [6], [7], [8] and [9].

The rotor system under investigation consists of a roll tube supported by two journal bearings. The simulation model of the rotor-bearing system includes the flexible roll tube, detailed non-linear model of journal bearings and description of the support of the roll. The parameters of the real structure are reproduced in the simulation model of the system as accurately as possible. This is achieved by measuring the non-idealities of the real structure and introducing them into the simulation model. In order to validate the proposed journal bearing model, the simulated results are compared with the

measurements obtained from the real structure. The MBS-model of the test rig is shown in Figure 25.

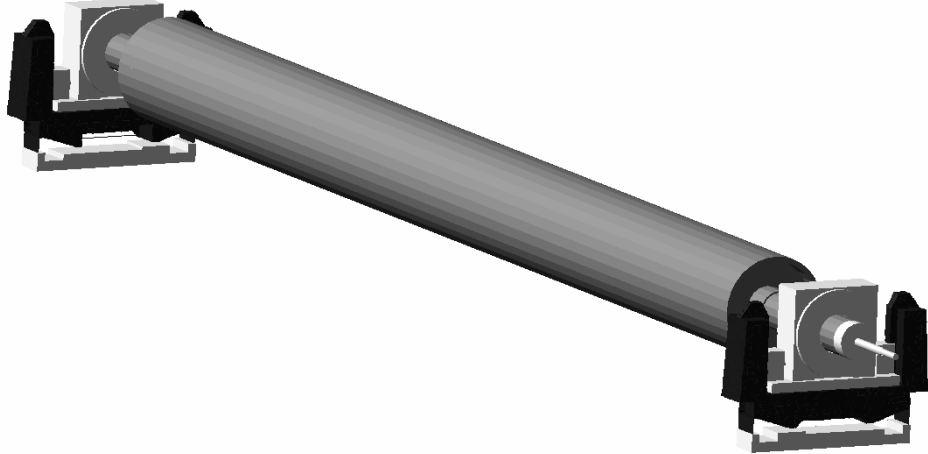


Figure 25. The simulation model of the test rig.

4.2.1 Multibody Dynamics

Mathematically, a body consists of an infinite number of particles while the inertial properties of the body consist of the properties of its particles. In multibody systems, the bodies interact with each other through joints. Mathematically, the joints are described by constraints between bodies. These constraints are simple to formulate when employing the body coordinate system. The body coordinate is fixed to the body and therefore the description of a particle in the body coordinate system remains constant when the body is assumed to be rigid. For this reason, the utilisation of the body coordinate system simplifies the description of the constraints.

Equations of Motion of Rigid Body Systems

When describing the dynamics of a body, the particles of the body are described in the global coordinate system. The global or inertial frame of reference coordinates are fixed and do not move with the body. The description of a rigid body in a three dimensional space, as in Figure 26, can be defined with six coordinates. Three coordinates define the location and another three coordinates define the orientation of the body.

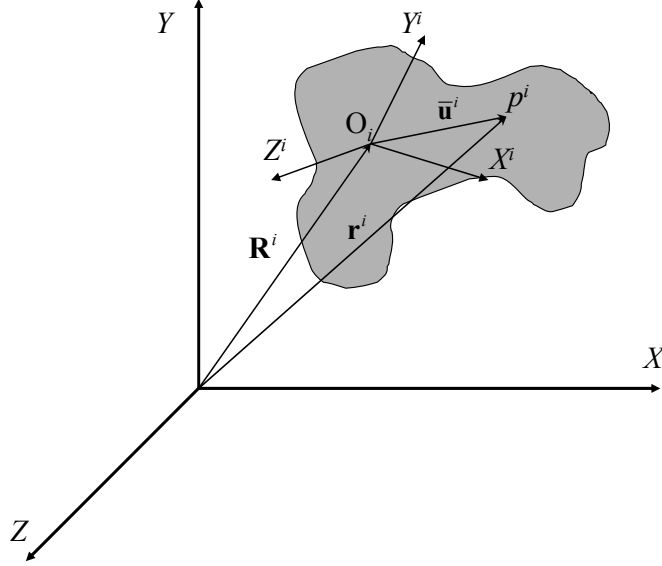


Figure 26. A rigid body in a three dimensional space.

The position of the arbitrary particle p^i of body i in the global coordinate system can be defined as following [38]:

$$\mathbf{r}^i = \mathbf{R}^i + \mathbf{A}^i \bar{\mathbf{u}}^i \quad (4.20)$$

where \mathbf{R}^i is the position vector from the origin of the global coordinate system to the origin of the local coordinate system, \mathbf{A}^i is the rotational matrix, that describes the orientation of the local coordinate system with respect to the global coordinate system and $\bar{\mathbf{u}}^i$ is the position vector of the particle p^i in the local coordinate system. Although there are a number of ways to describe the rotation matrix \mathbf{A}^i , the description based on the Euler angles is frequently used [40].

It is important to note that the rotational matrix \mathbf{A}^i includes non-linear terms, which enables a description of large rotations. In the multibody analysis, generalized coordinates are variables that are used to describe the position of particles in the system.

In a three dimensional space, the location and orientation of a body can be described with a vector of generalized coordinates as follows:

$$\mathbf{q}^i = [R_1^i \ R_2^i \ R_3^i \ \phi^i \ \theta^i \ \psi^i]^T \quad (4.21)$$

where R_1^i , R_2^i and R_3^i define the location of the origin of the local coordinate system of body i and ϕ^i , θ^i and ψ^i Euler angles that are used in the description of the rotational matrix.

The generalized coordinates are not typically independent. In multibody systems, the joints (i.e. constraints) form interaction between the coordinates. For this reason, movement in one body can cause movement in other bodies. The interactions between the different bodies can be expressed by using constraint equations. For the complete system, the generalized coordinates can be written as follows:

$$\mathbf{q} = [q_1 \ q_2 \ q_3 \dots q_n]^T \quad (4.22)$$

in which n is the number of generalized coordinates. A part of the components of the vector \mathbf{q} can be coupled with constraints. In dynamic analysis, the number of constraint equations n_c must be smaller than the number of generalized coordinates n . The constraint equations can be expressed in the general form as:

$$\mathbf{C}(q_1 \ q_2 \dots q_n, t) = 0 \quad (4.23)$$

in which $\mathbf{C} = [C_1(\mathbf{q}) \ C_2(\mathbf{q}) \ \dots \ C_{n_c}(\mathbf{q})]^T$ are the independent constraint equations. In Equation (4.23), the constraints are dependent of time and coordinates.

The constraints can be introduced to the equation of motion employing the augmented formulation with Lagrange multipliers. In this case, the equation of motion is a set of differential algebraic equations. Typically, the equations are solved through the use of the numerical integration approach of ordinary differential equations. To this end, the equation of motion is written as follows:

$$\begin{bmatrix} \mathbf{M} & \mathbf{C}_q^T \\ \mathbf{C}_q & 0 \end{bmatrix} \begin{bmatrix} \ddot{\mathbf{q}} \\ \boldsymbol{\lambda} \end{bmatrix} = \begin{bmatrix} \mathbf{Q}_e + \mathbf{Q}_v \\ \mathbf{Q}_c \end{bmatrix} \quad (4.24)$$

where matrix \mathbf{M} is a matrix that consists of mass matrices of all the bodies in the system, \mathbf{Q}_e is the generalized force vector of non-conservative forces, \mathbf{Q}_v is the quadratic velocity vector and \mathbf{C}_q is the matrix, which is formed from constraints and is called a Jacobian matrix. \mathbf{Q}_c is a vector that is comprised by differentiating the constraint equations twice with respect to time. With the equation of motion, the acceleration of the generalized coordinates $\ddot{\mathbf{q}}$ and Lagrange multipliers $\boldsymbol{\lambda}$ can be solved. The detailed derivation of the equations is given by Shabana in References [38] and [39].

4.2.2 Flexible Roll Tube

Flexibility in multibody dynamics can be modelled using a number of approaches. A rotor experiences large rotational displacements while deformations within the rotor usually remain small. For this reason, the multibody simulation approach with the floating frame of reference formulation is used to model the flexibility of the roll tube [39].

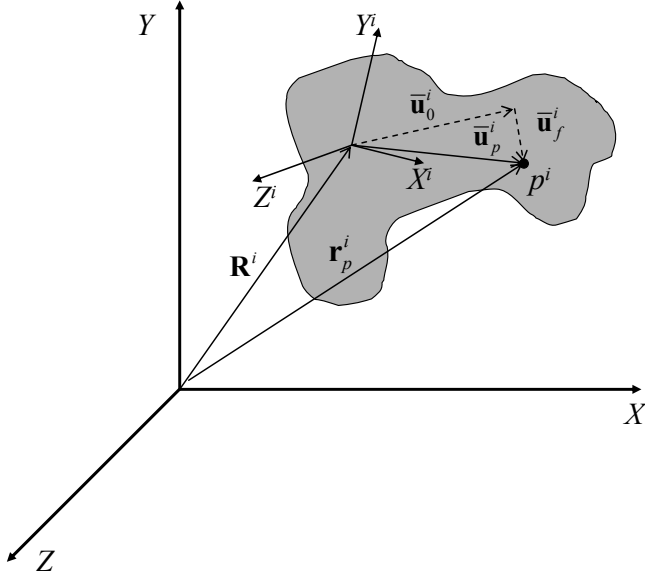


Figure 27. Global position of an arbitrary particle, p^i .

In the floating frame of reference approach, the global position of an arbitrary particle of the flexible body i , as depicted in Figure 27, can be defined as follows:

$$\mathbf{r}_p^i = \mathbf{R}^i + \mathbf{A}^i (\bar{\mathbf{u}}_o^i + \bar{\mathbf{u}}_f^i) \quad (4.25)$$

where \mathbf{R}^i is the position vector from the origin of the global coordinate system to the origin of the reference coordinate system, $\bar{\mathbf{u}}_o^i$ is the position vector that defines the undeformed position of the particle, and $\bar{\mathbf{u}}_f^i$ is the position vector that defines the deformed position of the particle. In Equation (4.25), vectors $\bar{\mathbf{u}}_o^i$ and $\bar{\mathbf{u}}_f^i$ are defined within the reference coordinate system that describe large translations and rotations of the flexible body. Due to the use of the reference coordinate system, the conventional finite element approach can be employed in the description of the vector $\bar{\mathbf{u}}_f^i$. It is noteworthy, however, that finite element models usually consist of a large number of nodal degrees of freedom, which makes it computationally expensive to define the deformations in the time domain analyses. This drawback can be overcome using the component mode synthesis [41] together with the floating frame of reference

formulation. In the component mode synthesis, the deformation vector can be described using vibration modes and modal coordinates instead of nodal coordinates. As a consequence, the dimensionality of the original finite element model (i.e. degrees of freedom) can be reduced without a significant loss of accuracy [39]. Using the component mode synthesis, the deformation of the flexible body can be described as follows:

$$\bar{\mathbf{u}}_f^i = \Phi^i \mathbf{p}^i \quad (4.26)$$

where Φ^i is the modal transformation matrix whose columns are the vibration modes and \mathbf{p}^i is the modal coordinates associated with the deformation modes.

In this study, the deformation modes defined in Equation (4.26) are calculated by employing the Craig-Bampton method with the orthonormalization procedure [42], which yields the orthogonal Craig-Bampton modes. The Craig-Bampton method results in two sets of modes that are non-orthogonal constraint modes and orthogonal fixed interface normal modes. The constraint modes can be obtained from a static equilibrium analysis while the fixed interface normal modes can be obtained by solving an eigenvalue analysis. Due to the use of static analysis, the constraint modes are not orthogonal, feature of which leads to non-diagonal forms of general stiffness and mass matrixes. In this study, the orthonormalization procedure is applied to the Craig-Bampton modes in order to enforce modes to be orthogonal.

In this study, the roll tube is modelled in a commercial finite element code (ANSYS) using eight-node brick-shaped solid elements with rotational degrees of freedom (SOLID 73). Figure 28 shows the coordinate system, parameters and mesh of the FE model. The finite element mesh of the roll is fine, as can be seen in Figure 28. The thickness of the shell of the roll tube is based on measurements carried out on the real structure. The finite element mesh is as dense as the grid used in the measurements. It is important to note that the modes and frequencies needed in the floating frame of reference approach are solved using the lumped mass approach, which may not lead to an exact representation of inertia of the element. However, the use of a fine finite

element mesh makes it possible to obtain an acceptable approximation for inertia properties of the flexible body.

Number of nodes	8744
Number of elements	5536
<i>Material properties:</i>	
Young's Modulus	$2.107 \cdot 10^{11}$ N/m ²
Mass Density	7801 kg/m ³
Poisson's ratio	0.3
<i>Dimensions of the rotor:</i>	
Total length of the rotor	5000 mm
Length of the shell	4000 mm
Diameter of the shell	322.5 mm

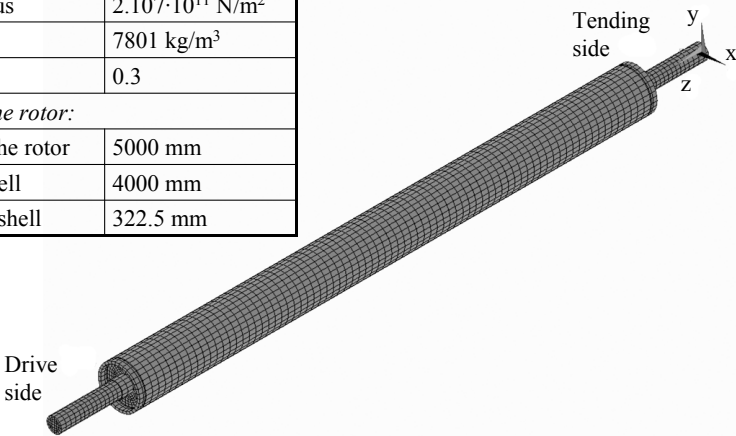


Figure 28. FE-model of the roll.

In the measurements, the thickness of the shell of the roll varied between 17.86 and 19.59 mm with the average value being 18.72 mm. Since the shell thickness is not constant, the roll has a non-ideal mass and stiffness distribution. The non-ideal mass distribution causes unbalance excitations, and the non-ideal stiffness distribution can cause a weight resonance in which the variation in bending stiffness, together with gravity, excites the symmetrical modes. This resonance condition occurs when the rotational velocity is one half of the frequency of the symmetrical mode. The details of the modelling of the variation in the thickness of the shell of the roll tube are described in [7] and [43].

Table 3 shows the inertia tensor, selected modes and their frequencies. The mass of the roll is 791 kg and the centre of mass relative to the coordinate system shown in Figure 28 is located [mm] at the point (-0.010, -0.053, 2499.705). The non-ideality of the roll can be seen from the inertia properties and the natural frequencies of the orthogonal bending mode pairs of the roll. The location of the centre of the mass is not on the neutral axis and the products of inertia are not equal to zero. It is noteworthy that the

frequencies of the orthogonal bending mode pairs are not equal as they would be in the case of an ideal roll.

Table 3. The inertia tensor and selected mode pairs of the roll.

NATURAL FREQUENCIES OF SELECTED MODE PAIRS					
Bending mode pair	1	2	3	4	5
Freq. [Hz]	77.8 / 77.9	200.0 / 200.2	279.6 / 279.7	348.5 / 348.7	523.3 / 523.5
Inertia tensor [kgm^2] (defined in the coordinate system shown in Figure 28)					
$\mathbf{I} = \begin{bmatrix} I_{xx} & I_{xy} & I_{xz} \\ & I_{yy} & I_{yz} \\ \text{symm.} & & I_{zz} \end{bmatrix} = \begin{bmatrix} 6649.988 & 0.005 & 0.024 \\ & 6650.008 & 0.070 \\ & \text{symm.} & 14.525 \end{bmatrix}$					

Comparison with the Experimental Modal Analysis

The experimental modal analysis was performed to measure natural frequencies of the test roll [44]. The modal analysis was done by using lifting belts and spring set between the belts and the hoist crane. The frequencies of the measured rigid body modes were close to zero.

The incorrect damping ratios for modes 2,3 and 6 are due to the hoisting belts that increased the damping in the vertical direction. For this reason, the lower damping values are used for each mode pair in the simulation model [7]. The results of the experimental modal analysis are shown in Table 4.

Table 4. The results of the experimental modal analysis of the roll [7].

Mode	Frequency [Hz]	Damping ratio [%]	Comments
1	78.048	0.018	
2	78.285	0.138	Damping incorrect
3	196.67	0.035	Damping incorrect
4	196.93	0.016	
5	270.27	0.023	
6	270.35	0.034	Damping incorrect

A good agreement is obtained between measured and simulated natural frequencies of the roll as can be seen when comparing results in Table 3 with Table 4.

4.2.3 Support of the Roll

The support of the roll is a modified pedestal of a balancing machine. The support rollers of the balancing machine have been replaced with bearing housings. In the simulation model, the support is modelled using one flexible body and two rigid bodies. These bodies are connected by spring-damper forces and constraints. The support assembly and the properties of the flexible frame body are shown in Figure 29. The frame body is an assembly of a base body made of cast iron and steel bodies, which are bolted to the base body. The flexibility of the frame body is modelled using the same approach as is employed in the roll. A total of 20 vibration modes of the frame body are selected for the dynamic simulation, while the bandwidth of the selected modes varies between 226 Hz and 6234 Hz. The total weight of the pedestal assembly is 127 kg. The journal bearing is modelled as a force between the bearing housing and the rotor. The bearing force is computed on the basis of the proposed non-linear journal bearing model that accounts waviness.

To shed a light on the support properties, the following stiffness coefficients and damping ratios are determined using the simulation model of the pedestal:

- Vertical stiffness 262 MN/m (*Y*-direction in global coordinate system)
- Horizontal stiffness 63 MN/m (*X*-direction in global coordinate system)
- Horizontal and vertical damping ratios 2 %.

The above stiffness values are obtained by measuring the displacements caused by the load. The damping ratios are determined by simulating the force impulse and using the logarithmic decrement, as explained in [45]. The horizontal stiffness is dominated by a piezo sensor, the stiffness of which is stated to be 70 MN/m. The piezo sensor, that is, the spring element, is modelled between the cast iron frame body and the steel base plate, as can be seen in Figure 29.

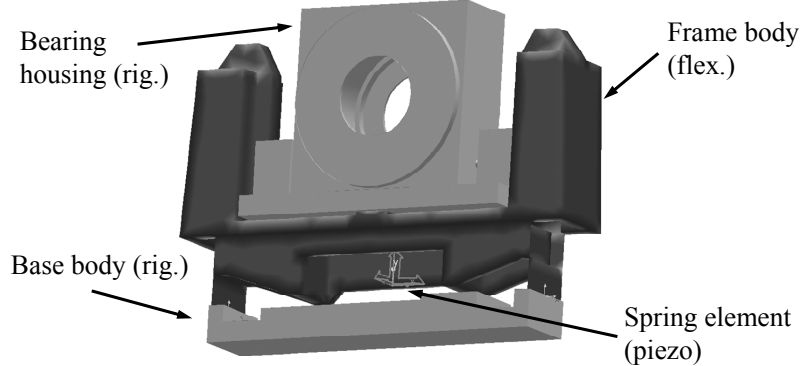


Figure 29. The pedestal structure of the test rig.

4.2.4 *Journal Bearing*

The bearing used in the test rig is a plain hydrodynamic journal bearing, the dimensions of which are shown in Table 5. The bearing L/D -ratio is 0.33. Figure 30 depicts the pressure distribution that the rotation of the journal generates in the bearing. The proposed model of the journal bearing omits the oil feed groove; however, since the groove is located in the upper part of the bearing, the pressure around the groove can be assumed to be low. Therefore, the error caused by this simplification is not significant considering the dynamics or load carrying capacity of the bearing. The oil feed in the test bearing is obtained by one axially aligned groove, the length and width of which are 35 mm and 6 mm, respectively.

Table 5. The parameters of the journal bearing.

Inner diameter	150 mm
Outer diameter	170 mm
Length	50 mm
Radial clearance	0.075 mm
Used lubricant	Shell Tellus T ISO VG 32

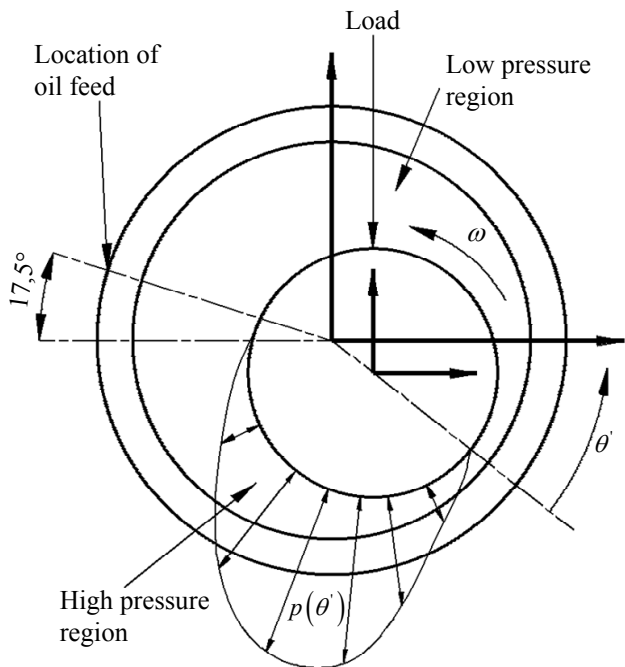


Figure 30. The hydrodynamic pressure generated by rotation of the journal in the journal bearing, and the location of the oil feed in the test bearing.

4.2.5 Shaft Journal Waviness

The shaft journal of the bearing always has some waviness due to manufacturing tolerances. In the bearing model, waviness is obtained from measurements. The waviness of the shaft journal is measured in three cross-sections; in the middle of the sliding surface and 20 mm in both directions from the middle.

The proposed bearing model assumes that the thickness of the oil film remains constant along the axial direction. For this reason, the shape of the shaft journal is assumed to be constant along the axial direction. Accordingly, a weighted mean is computed from the three measured cross-sectional shapes. The weighting coefficients are obtained based on the assumption that the shape of the cross-section is the most dominating in the axial position in which the hydrodynamic pressure is largest, that is, in the middle of the bearing. The weighting factors are evaluated based on the pressure distribution of the short journal bearing in the axial direction, and they can be written as follows:

$$f(Z) = Z^2 - \frac{L^2}{4} \quad (4.27)$$

where Z is the axial coordinate and L the length of the bearing. The weighting factors can be computed using the following expression [33]:

$$\lambda_i = \frac{f_i}{\sum_{i=1}^3 f_i} \quad (4.28)$$

where f_i is obtained by computing Equation (4.27) using axial coordinate Z_i of the measured cross-section. The weighted means can be computed as

$$R_\lambda = \lambda_1 R_1 + \lambda_2 R_2 + \lambda_3 R_3 \quad (4.29)$$

The weighted means of the waviness components and their phase angles are shown in Table 6 for the drive side and tending side of the roll, respectively.

Table 6. The weighted means of the waviness components and their phase angles of the shaft journal.

Waviness order	Amplitude [μm]		Phase angle [rad]	
	Drive side	Tending side	Drive side	Tending side
2	5.21	5.53	5.02	5.72
3	1.19	1.53	4.60	1.49
4	1.07	1.57	5.05	4.63
5	0.21	0.33	5.24	1.54

As can be seen in Table 6, the amplitude of the 5th-order waviness component is small. Based on Table 6, it can be assumed that higher components become even smaller and consequently less important in terms of the rotor system simulation. Therefore, only 2nd-, 3rd- and 4th-order components are considered in this study. Figure 31 shows the

exaggerated profiles of shaft journals in drive side and tending side. Waviness amplitudes are multiplied by factor 300 to visualise the shape.

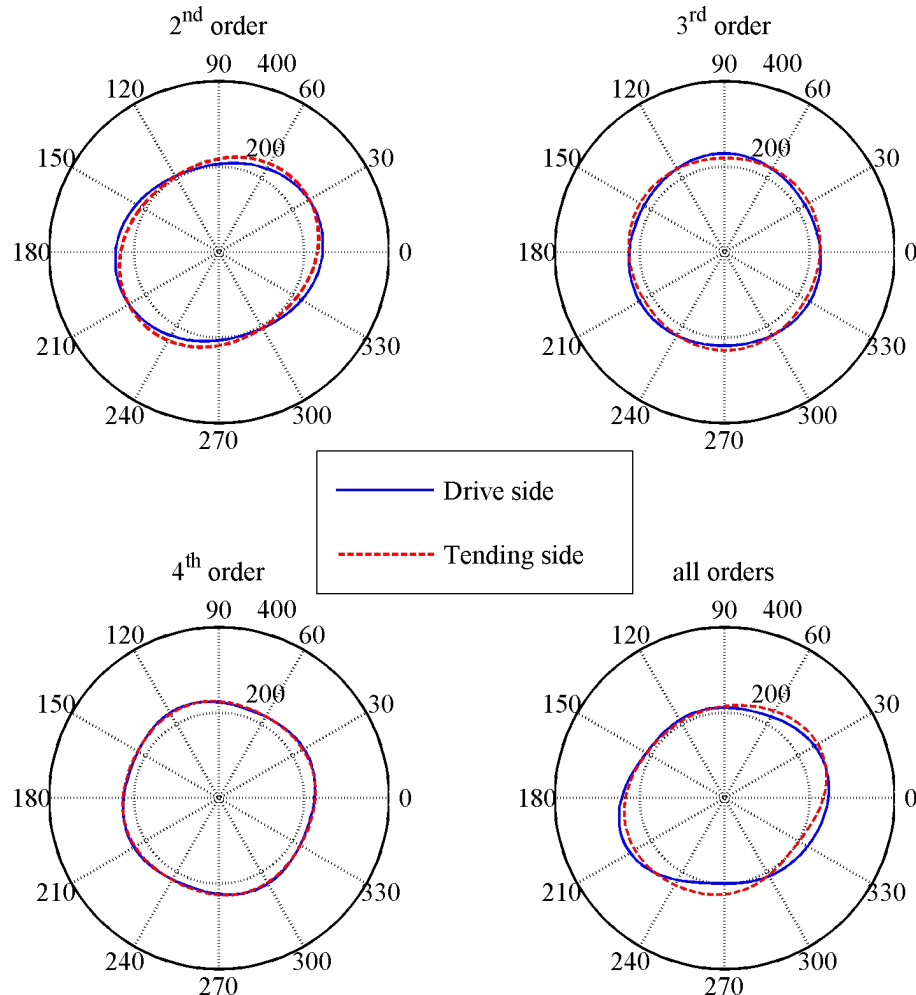


Figure 31. A graphical presentation of exaggerated waviness of the shaft journal.

4.2.6 Bearing Bushing Waviness

The waviness of bearing bushing was not measured from bearings used in the test rig. However, this non-ideality is always present in real assemblies due to manufacturing errors. For this reason also the effect of the bushing waviness to the results is studied by simulation runs that will be explained in Chapter 4.2.9.

4.2.7 Temperature and Viscosity of the Lubricants

The viscosity of the lubricant is highly dependent on the operating temperature. Accordingly, the dynamic behaviour of the bearing depends on the viscosity of the oil. In the measurements, the oil temperature rose as the rotational velocity of the rotor increased. At the beginning of measurements, the temperature of the oil was 30 °C, while at the end, it was close to 70 °C as can be seen in Figure 32. Figure 32 illustrates the oil temperature measured during experimental testing and is plotted versus the rotational velocity of the rotor. The oil temperature was measured from the return flow, in which case it can be assumed to be close to the average temperature of the oil inside the bearing. In the simulations, the oil temperature is recorded by computing the oil viscosity according to the DIN standard 31654 T2 as follows [3]:

$$\eta = \eta_x e^{\left(\frac{159.56}{T+95^\circ C} - 0.181913 \right) \ln \frac{\rho VG}{10^6 \eta_x}} \quad (4.30)$$

where $\eta_x = 0.18 \cdot 10^{-3}$ Pas, ρ is the density of the lubricant, T is the temperature of the lubricant and VG is the viscosity grade of the lubricant. In this study, the viscosity grade is 32 and the density of the lubricant $\rho = 900$ kg/m³. In the simulations, the temperature of the lubricant is calculated from the measurement results using a curve fitting method. In this way, the oil temperature at different rotational velocities is set at the same value in the simulations and measurements.

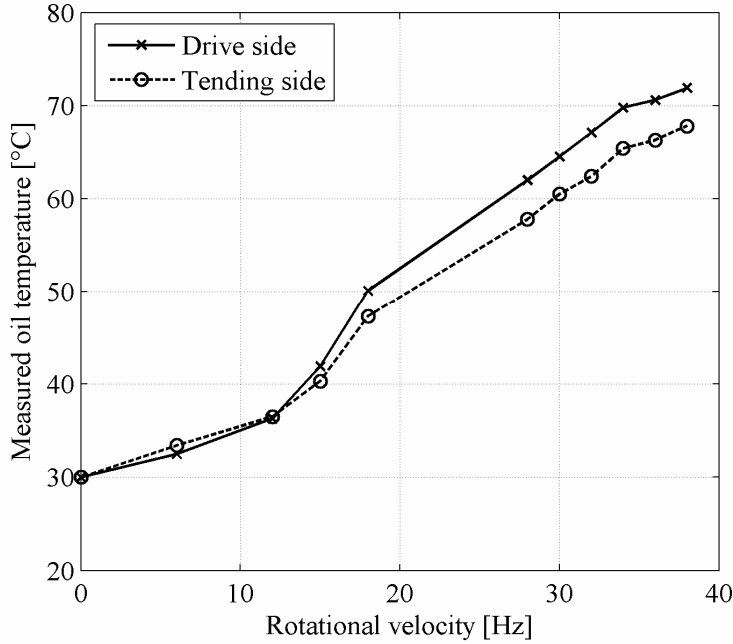


Figure 32. Temperature of the lubricant during measurements.

4.2.8 Measurements of the Rotor System

The measurement equipment comprises a PC-based data acquisition system, two laser sensors with amplifiers, a connection panel and a guide bar in which the sensors have been installed. The displacement of the roll is measured in the middle of the roll in the vertical and horizontal directions with two laser sensors as shown in Figure 33 where the locations of the measurement points are illustrated. The angular velocity of the rotor is obtained from a pulse sensor. The measurement equipment in the test rig is similar to that used in the active damping tests performed on the same structure [46].

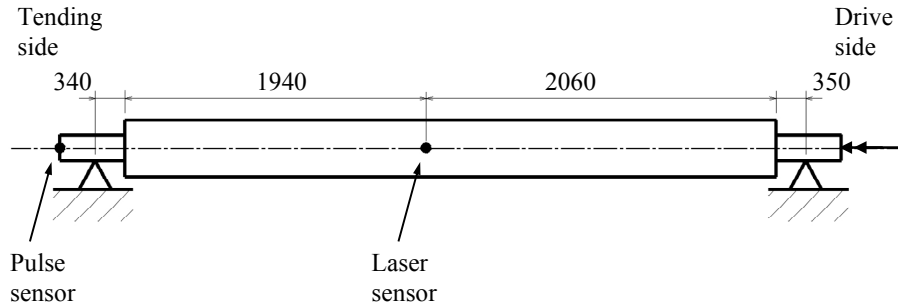


Figure 33. The locations [mm] of the measurement points.

4.2.9 Verification of the Model of the Rotor-Bearing System

In this chapter, the simulation results are compared with measurements performed on the real structure. The horizontal and vertical throw is measured from the middle of the rotor. In the comparison the half-critical rotational velocity region is studied. The results are plotted using amplitude vs. rotational velocity charts and spectrum maps.

Results of the Half-Critical Speed

The variable shell thickness and waviness of the shaft journal are included in the simulation model of the rotor system; therefore, two non-idealities influence the half-critical speed region of the rotor system. Additionally, as described in Chapter 3.2 the waviness of bearing bushing was included in the bearing model to emphasize its effect on response. Even if the third non-ideality does not excite the system it will have some effect on system response. To study the half-critical speed region, seven different cases are simulated. The first three cases studied the effect of non-ideal shaft journal and stiffness variation of rotor shell to dynamic responses. Using two simulations the effect of bearing bushing waviness on dynamic responses are considered. Additionally, two simulations are performed to study the effect of unbalance mass on the response at half-critical speed region. The first five simulation cases are described in Table 7. In cases 4 and 5 only the second order waviness component was considered to the bearing bushing. The cases used to study the effect of unbalance are described in the end of this chapter.

Table 7. Five cases on half-critical survey.

Case	Shaft journal	Shell of the rotor	R_{b2} [μm]	ψ_{b2}
1	Waviness included	Ideal	0	0
2	Ideal	Variable thickness	0	0
3	Waviness included	Variable thickness	0	0
4	Waviness included	Variable thickness	2	$\pi/2$
5	Waviness included	Variable thickness	2	π

Figure 34 shows the amplitudes of the twice-running-speed response in the middle of the roll with respect to the rotational velocity for the cases 1-3 compared with the measured results. Figure 35 shows the amplitudes of twice-running-speed response in the middle of the roll for cases 4-5 compared with the measured results. Figure 36 shows the spectrum maps in the middle of the roll. The spectrum maps are obtained using case three which includes both measured non-idealities.

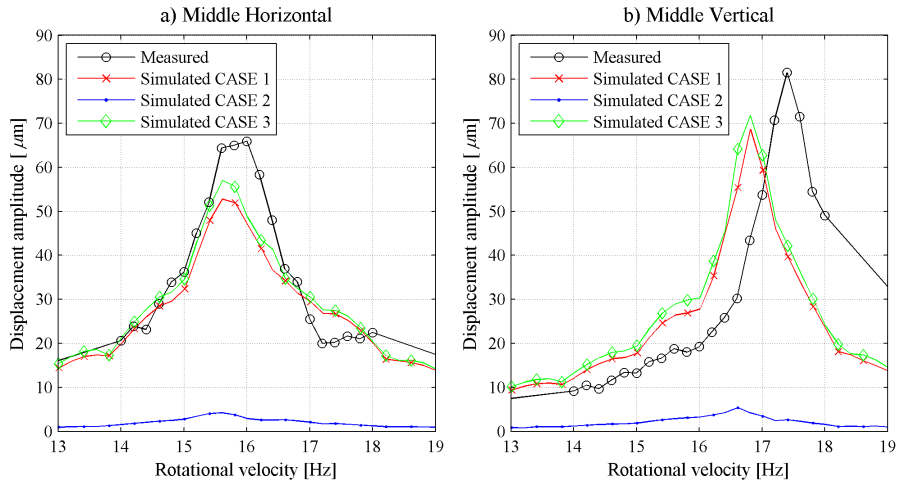


Figure 34. The amplitudes of the twice-running-speed response in the middle, (a) horizontal, (b) vertical.

The agreement of twice-running-speed response is good between measured and simulated results. The amplitude of the twice-running-speed response is slightly larger in the test rotor than in the simulation model, as can be seen in Figure 34. The difference is small enough that it may be caused by a number of possible reasons. For

example the measurement of the waviness of the shaft journal has an accuracy of $1\mu\text{m}$ and the largest waviness component was $5.5\mu\text{m}$. For this reason, even 20% error is possible in the measurements of shaft journal waviness component. The phase angles of the waviness components effects to response as well. Depending on the phase in between the shaft journal waviness and the stiffness variation of the shell, they may emphasize each other in terms of excitation or, on the other hand, they may attenuate each other in terms of excitation. Furthermore, as can be seen from Figure 34 the shaft journal waviness affects strongly to the response amplitude.

However, the difference may be partly caused by the journal bearing model in which the oil viscosity influences the stiffness and damping characteristics of the bearings. Therefore, the difference may be due to inaccuracies in the approximations of the oil viscosity. It must also be noted that the film thickness of the bearing may change during the operation of the bearing. The hydrodynamic pressure can cause elastic deformations in the bearing housing, which is not accounted for in the proposed model. As a result, the gap between the shaft journal and the bearing ring may differ from that used in the model. LaBouff and Booker [47] have studied the effects of an elastic bearing housing in the case of a dynamically loaded journal bearing. Their results showed that when the elasticity of the housing is included, the bearing eccentricity ratio and minimum film thickness as well as the peak pressures inside the bearing are modified. Prakash and Peeken [15] conclude that the elastic deformation of the bearing ring decreases the effects of roughness. In this case, the clearance of the bearing may change because of the high oil pressure acting in the bearing. Moreover, thermal expansion is one uncertainty that may change the bearing gap. The nominal radial clearance of the bearing is $75\ \mu\text{m}$, which is a small dimension considering the other dimensions of the system. The above-mentioned uncertainties may most probably change the amplitudes of the twice-running-speed response of the rotor-bearing system with the amount of difference between measured and simulated results.

The waviness of the shaft journal influences the vibrations of the system in the half-critical speed region. The waviness in the shaft journal leads to a vibration amplitude that is considerably larger than that caused by variations in the stiffness of the rotor, which can be seen when comparing cases 1 and 2 in Figure 34. Based on this result it

can be concluded that the shaft journal waviness is the most significant non-ideality of the rotor system with journal bearings when considering the vibrations in half-critical speed regime.

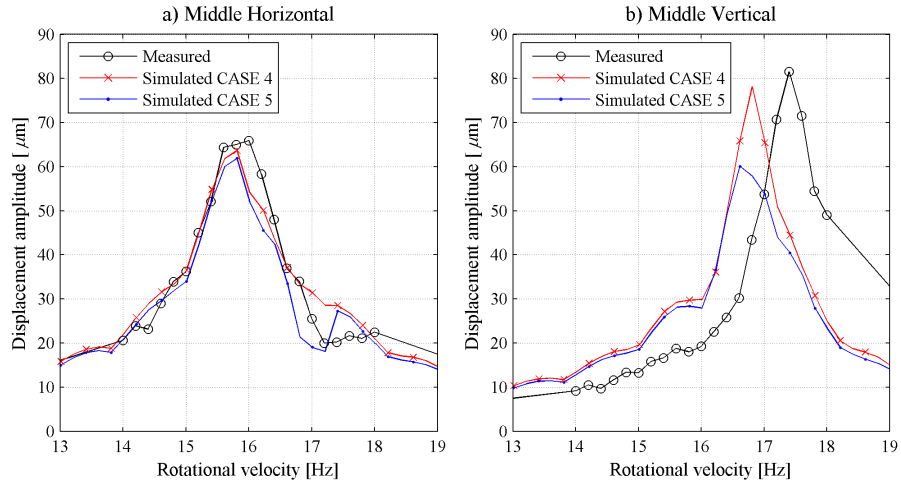


Figure 35. The amplitudes of the twice-running-speed response in the middle for additional simulation cases, (a) horizontal, (b) vertical.

As can be seen in Figure 35 the waviness error of bearing bushing affects significantly the twice-running-speed response. The used waviness error in simulation cases four and five can be considered to be inside the manufacturing tolerances and therefore its presence in test bearing is possible. It can also be concluded that this uncertainty of the model alone can explain the small difference between measured and simulated results in Figure 34.

The shapes of the simulated response curves are similar to the measured ones. Both results also show the cross-coupling between the vertical and the horizontal amplitudes. The peak amplitudes and rotational velocities at which they occur are presented in Table 8.

Table 8. Peak amplitudes in half-critical survey.

	Measured	Case1	Case2	Case3	Case4	Case5
Horizontal peak [μm]	66.0 at 16.0Hz	52.8 at 15.6Hz	4.2 at 15.6Hz	57.1 at 15.6Hz	63.7 at 15.8Hz	61.9 at 15.8Hz
Vertical peak [μm]	81.6 at 17.4Hz	68.7 at 16.8Hz	4.9 at 16.6Hz	71.8 at 16.8Hz	78.2 at 16.8Hz	60.1 at 16.6Hz

It can be seen in Table 8 that the highest amplitudes of the twice-running-speed responses were reached at different velocities for different directions. This difference is mainly due to different stiffness characteristics of the supporting structure in the vertical and horizontal directions. The stiffness of the support was not measured, although based on FE-model of the support the horizontal stiffness of the structure was remarkably lower than in vertical direction. In the measurements the difference between velocities where the highest vibration amplitudes were seen was a bit larger than in simulations. This difference between simulation and measurement results is likely to be result from inaccurate stiffness of the supporting structure in the simulation model.

The simulated spectrum maps in the middle of the rotor can be seen in Figure 36. All the modelled excitations can be seen in the map in Figure 36.

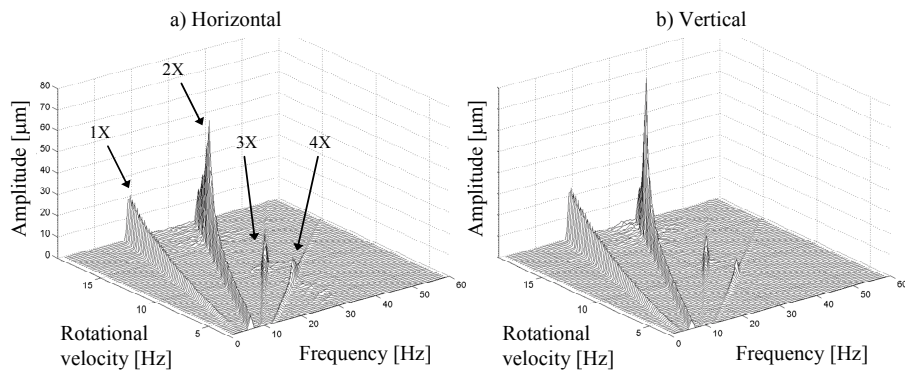


Figure 36. Simulated spectrum maps of the throw in the middle of the roll, (a) horizontal (b) vertical.

As was stated before in Chapter 4.1 the unbalance of the rotor may affect the vibration amplitude of twice rotating velocity due to oil film non-linearity. In the following, results based on measurements and simulations of roll with two different unbalance configurations are presented. The first configuration is named UB0 and it refers to balanced test roll. In the second configuration, called UB1, three unbalance masses were added to the roll. Figure 37 presents the unbalance masses in configuration UB1.

MASS POSITION	MASS [g]	R [mm]	α [$^{\circ}$]
1	75	177.5	270
2	50	177.5	0
3	50	177.5	0

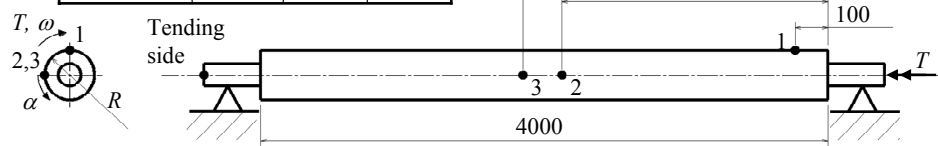


Figure 37. Mass point locations in the measurements of configuration UB1.

The amplitudes of twice rotating velocity response from the measurements and simulations are presented in Figure 38 from the measurements and simulations. The simulation model included the same non-idealities as case 3 in Table 7.

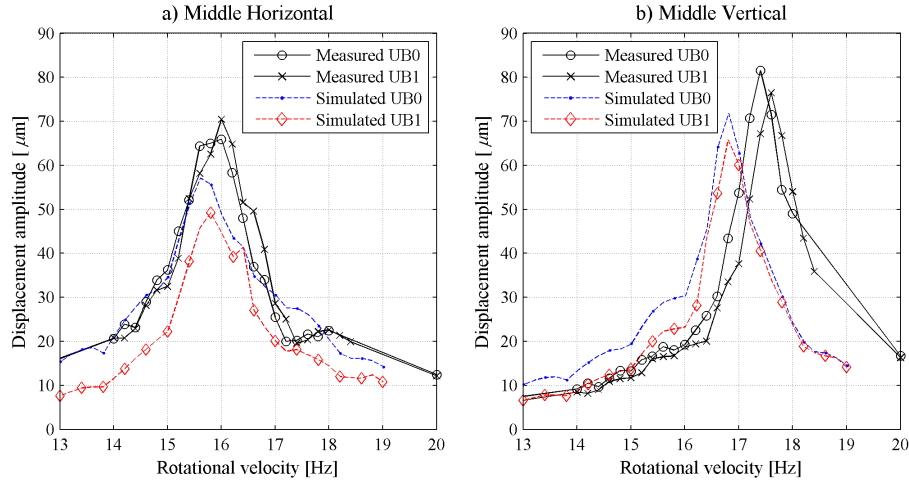


Figure 38. The amplitudes of the twice-running-speed response in the middle for simulation configurations UB0 and UB1, (a) horizontal, (b) vertical.

It can be seen in Figure 38 that the unbalance configuration had an effect on the amplitudes of twice-running-speed response in measurements as well as in simulation. The difference between simulated responses of UB0 and UB1 are in magnitude similar to the ones from measurements. This can be interpreted such that the effect of unbalance to twice-running-speed response is similar between measurements and simulation. However, in the simulations the unbalance masses decreased the amplitudes in both directions but in the measurements the amplitudes increased in horizontal direction and decreased in vertical direction. The same comparison was performed also with simulation model as case 1 in Table 7 and the results were similar as both directions decreased in simulations when unbalance masses according the configuration UB1 were added.

5 CONCLUSIONS

In this thesis, the theory of modelling of the hydrodynamic plain journal bearing was studied. Two models for the short journal bearing and two models for the long journal bearing were examined. The computation of linear dynamic coefficients for journal bearings was presented. Four bearing models were compared with respect to the load carrying capacity. The dynamic properties of the models were compared by means of linearized stiffness and damping coefficients that were calculated for each model. In reality, the journal bearing has always some non-idealities. The waviness of the shaft journal is one of the non-idealities of a rotor-bearing system that can cause superharmonic vibrations. This study introduced a method for modelling the waviness in shaft journals in the case of a hydrodynamic journal bearing support. One of the presented bearing models, introduced by Vance [17], was chosen for further development to describe the waviness in the shaft journal. The proposed journal bearing model is based on the short bearing solution of the Reynolds equation and the bearing model accounts for the waviness of the shaft journal in the bearing by employing the Fourier cosine series. This complicates the integration of the pressure equations of the bearing, making it necessary to use a numerical integration procedure in the solution of the equation. While numerical integration is used, it is possible to apply variable integration boundaries as a consequence of which only the positive pressure region is accounted for. The method can be adapted to situations where the length and boundaries of positive pressure region varies. Additionally, a method to take into account waviness in bearing bushing was presented. Even if the non-ideal bearing bushing does not excite the vibrations of rotor-bearing system, based on simulations it was found to have influence to system response.

The proposed bearing model was implemented in commercial multibody dynamics software. The implemented model was firstly used to verify the model of ideal bearing with results obtained from literature by means of simple model of rigid rotor with one journal bearing. Furthermore, the simple model was used to emphasize the differences in responses calculated with linear and non-linear bearing models. It was summarized that the linear model can be used in many situations but, on the other hand, gives unrealistic results in certain cases. The multibody approach gives the possibility of

describing the non-idealities of rotor-bearing systems in such a way that the coupling between the non-ideal bearing assembly and non-ideal rotor is accounted for. In the introduced simulation approach, the proposed model was employed in order to describe a non-ideal rotor-bearing system. The rotor system examined consists of a roll tube, journal bearings and support of the roll. The ideal tube roll was used to emphasise the vibrations excited by the non-ideal bearing assembly exclusively. Based on the simulation results, it can be concluded that the vibrations due to non-idealities in bearings are significantly larger than the excitations due to a non-ideal roll. The simulation results also showed that the bearing assembly has a significant effect on vibrations of rotor-bearing systems. Based on the simulation results, presence of waviness in bearing bushing was discovered to have an effect on system response. In conclusion, the coupled simulation which can take both non-ideal bearings and non-ideal rotors into account should be used when the vibration analysis is performed.

The simulation results for the rotor system were verified using measurement results obtained from the existing structure. A comparison between the simulated and measured results showed that the proposed model accurately predicts the dynamic behaviour of the rotor-bearing system. The displacement amplitude of the twice-running-speed vibration component agrees well with the measured one. There are some discrepancies between the simulated and measured results in the case of the displacements of the twice-running speed response. However, this can be explained by, for example, the presence of bearing bushing waviness. There are also some other uncertainties that may have an effect on response amplitudes of error tolerance of a few percent. The actual stiffness variation of the rotor may be different than the modelled one. The real roll probably has other non-idealities than the variation in the shell thickness, such as welds and uneven distribution of the modulus of elasticity. The changes in shape in the bearing gap caused by thermal expansion and elastic deformation in the bearing bushing should be accounted for in the bearing model in order to obtain more accurate results. However, the proposed method for modelling the waviness in shaft journals in journal bearings provides reliable response curves for the rotor system studied.

5.1 Suggestions for Future Studies

In this study, the effect of shaft journal waviness on rotor superharmonic vibration was considered to be significant in the analyses of the rotor-bearing system. The proposed bearing model is able to capture the dynamic behaviour of the bearing. However, some inaccuracies were discovered in the comparison between simulated and measured results. In order to develop a more accurate model of the hydrodynamic bearing, the elasticity of the bearing bushing should be included in order to capture the effects of high pressure into the bearing geometry. The temperature expansion of the different bodies in the bearing assembly is a characteristic that should also be taken into account. Additionally, the viscosity of the lubricant was considered to be dependent on temperature only. However, in order to obtain a more accurate description of lubricant viscosity, the viscosity's dependence of current pressure might be taken into the consideration.

Multibody dynamics simulation is a flexible and general approach to the analysis of rotor systems. However, as in all simulations, the level for the necessary accuracy is difficult to determine. A detailed simulation model may become too expensive to compute, and therefore, it may not serve its purpose efficiently enough. In bearing modelling, an accurate description of the pressure field can be obtained using the solution of the Reynolds equation, for example, by means of FEM, in which case additionally the formal non-idealities of the bearing could be included. This approach, however, leads to expensive computation. On the other hand, the non-idealities in the bearing affect the system response and they should be included in the simulation model. In this study, an efficient method to include shape non-idealities in the bearing was introduced. However, there are some uncertainties that need to be considered in the future. Therefore, the model should be verified more with experimental data, obtained from a test rig specifically designed for measurements of bearing performance.

In the future, as the demands on the performance of rotating machinery increase, the tools for design should develop as well. Detailed simulation of complex systems offers an efficient tool for analysing systems in detail. As the computing capacity of computers increases, detailed simulations can be computed more efficiently. Mathematical modelling has interested scientists for quite a while and therefore several

theories about the modelling of components of mechatronic machines are available. The multibody dynamics approach gives an opportunity to employ the developed methods and to analyse the coupled components as whole machines. A good example of such simulation application is the studied rotor-bearing system.

REFERENCES

- [1] Goodwin, M.J. Dynamics of Rotor-Bearing Systems. London: Unwin Hyman. 1989.
- [2] Constantinescu, V.N. Sliding Bearings. New York: Allerton Press. 1985.
- [3] Kivioja, S., Kivivuori, S. and Salonen, P. Tribologia – kitka, kuluminen ja voitelu. Helsinki: Otatieto. 1998.
- [4] Rao, J.S. Rotor Dynamics. New Delhi: Wiley Eastern. 1983.
- [5] Krämer, E. Dynamics of Rotors and Foundations. Berlin Heidelberg: Springer-Verlag. 1993.
- [6] Brown, M.A. and Shabana, A.A. Application of Multibody Methodology to Rotating Shaft Problems. Journal of Sound and Vibration. 1997. Vol. 204: pp. 439-457.
- [7] Sopanen, J. Studies of Rotor Dynamics Using a Multibody Simulation Approach. Doctoral Thesis. Lappeenranta University of Technology. Department of Mechanical Engineering. 2004.
- [8] Sopanen, J. Virtuaaliprototyypien käyttö roottorin dynamiikan analysoinnissa. Master's Thesis. Lappeenranta University of Technology. Department of Mechanical Engineering. 1999.
- [9] Kärkkäinen, A. Dynamic Simulations of Rotors During Drop on Retainer Bearings. Doctoral Thesis. Lappeenranta University of Technology. Department of Mechanical Engineering. 2007.

- [10] Pinkus, O. and Sternlicht, B. Theory of Hydrodynamic Lubrication. New York: McGraw-Hill Book Company Inc. 1961.
- [11] Cameron, A. Basic Lubrication Theory, 3rd Edition. Chichester: Ellis Horwood Limited. 1981.
- [12] Hamrock, B.J. Fundamentals of Fluid Film Lubrication. Ohio: McGraw-Hill Inc. 1994.
- [13] Someya, T. Journal-Bearing Databook. Berlin: Springer-Verlag. 1989.
- [14] Rasheed, H.E. Effect of Surface Waviness on the Hydrodynamic Lubrication of a Plain Cylindrical Sliding Element Bearing. Wear. 1998. Vol. 223: pp. 1-6.
- [15] Prakash, J. and Peeken, H. The Combined Effect of Surface Roughness and Elastic Deformation in the Hydrodynamic Slider Bearing Problem. ASLE Transactions. 1985. Vol. 28: 1. pp. 69-74.
- [16] Bachschmid, N., Pizzigoni, B. and Tanzi, E. On 2xrev – Vibration Components in Rotating Machinery Excited by Journal Ovalization and Oil Film Non-linearity. ImechE. Conference Transactions 2000-6. Paper C576/083/2000. pp. 449-458.
- [17] Vance, J.M. Rotordynamics of Turbomachinery. Texas: John Wiley & Sons Inc. 1988.
- [18] Keskiniva, M. Simulation and Balancing of Flexible Rotors in Terms of Semidefinite Modal Coordinates. Doctoral Thesis. Tampere University of Technology. 1997.
- [19] Butenschön H.-J. Das Hydrodynamische, Zylindrische Gleitlager endlicher breite unter instationärer Belastung. Dissertation. Technische Universität Karlsruhe. 1976.

- [20] Barrett, L.E., Allaire, P.E. and Gunter E.J. A Finite Length Bearing Correction Factor for Short Bearing Theory. *Journal of Lubrication technology*. 1980. Vol. 102: pp. 283-290.
- [21] Hannukainen, P. Comparison of Journal Bearing Modeling Methods. Master's Thesis. Lappeenranta University of Technology. Department of Mechanical Engineering. 2001.
- [22] Booker, J.F. A Table of the Journal-Bearing Integral. *Journal of Basic Engineering*. June 1965. pp. 533-535.
- [23] Frene, J., Nicolas D., Deguerce B., Berthe D. and Godet M. Hydrodynamic Lubrication - Bearings and Thrust Bearings. *Tribology Series* 33. Amsterdam: Elsevier Science. 1997.
- [24] Hannukainen, P., Sopanen, J. and Mikkola, A. Subharmonic Vibrations of a Roll Tube Supported by Plain Journal Bearings. *Journal of Multi-Body Dynamics*. 2003. Vol. 107: pp. 301-312.
- [25] Lang, O.R. *Gleitlager*. Berlin: Springer. 1978.
- [26] Zhoy, H., Zhao, S., Xu, H. and Zhu, J. An Experimental study on oil-film coefficients. *Tribology International*. 2004. Vol. 37: pp. 245-253.
- [27] Virtanen, J. Dynamic Properties of Bearings – State of the Art. VTT manufacturing Technology. Espoo. 1999. Report VALB409.
- [28] Choy, F.K., Braun, M.J. and Hu, Y. Nonlinear Study of a Misaligned Hydrodynamic Journal Bearing. *Tribology Transactions*. 1993. Vol. 36: pp. 421-431.
- [29] Guha, S.K. Analysis of Steady-state Characteristics of Misaligned Hydrodynamic Journal Bearings with Isotropic Roughness Effect. *Tribology International*. 2000. Vol. 33: pp. 1-12.

- [30] Boyer, J. and Fillon, M. An Experimental Analysis of Misalignment Effects on Hydrodynamic Plain Journal Bearing Performances. *Journal of Tribology*. 2002. Vol. 124: pp. 313-319.
- [31] Gerald, C.F. and Wheatley, P.O. *Applied Numerical Analysis*, 6th Edition. Reading: Addison Wesley. 1999.
- [32] RollResearch International. Espoo. Finland. [accessed at 9.3.2004], available in: <http://www.rollresearch.fi/>.
- [33] Råde, L. and Westergren, B. *Beta - Mathematics Handbook for Science and Engineering*. Lund. Studentlitteratur. 1995.
- [34] Mäkinen, R.A.E. *Numeeriset menetelmät*. Lecture notes 1: University of Jyväskylä. Department of Mathematical Information Technology. 1999.
- [35] ADAMS 10.0 Online Documentation. Mechanical Dynamics, Inc. 1999.
- [36] Chen, W.J. and Gunter, E.J. *Introduction to Dynamics of Rotor-Bearing Systems*. Trafford Publishing. 2005.
- [37] Lalanne, M. and Ferraris, G. *Rotordynamics Prediction in Engineering*, 2nd Edition. West Sussex: John Wiley & Sons. 1998.
- [38] Shabana, A.A. *Computational Dynamics*. New York: John Wiley & Sons. 2001.
- [39] Shabana, A.A. *Dynamics of Multibody Systems*, 2nd Edition. New York: John Wiley & Sons. 1998.
- [40] Goldstein, H. *Classical Mechanics*, 2nd Edition. Reading (MA): Addison-Wesley. 1980.

- [41] Kim, S. and Haug, E.J. Selection of deformation modes for flexible multibody dynamics. *Mechanics of Structures and Machines*. 1990. Vol. 18: pp. 565-586.
- [42] Craig, R.R. and Bampton, M.C.C. Coupling of Substructures for Dynamic Analyses. *AIAA Journal*. 1968. Vol. 6: pp. 1313-1319.
- [43] Sopanen, J. and Mikkola, A. Study of Sub-harmonic Vibration of a Tube Roll Using Simulation Model. 2nd Triennial International Symposium on Multi-body Dynamics: Monitoring & Simulation Techniques, held in Bradford, UK, 2000. pp. 57-68.
- [44] Juhanko, J., and Porkka, E. PyöriVÄRE – Telakoelaitteen verifointimittaukset – Liukulaakeritu roottori, osa 1, Helsinki University of Technology Reports in Machine Design 6/2001.
- [45] Rao, S.S. Mechanical vibrations, 2nd edition. Reading (MA): Addison-Wesley. 1990.
- [46] Kuosmanen, P., Juhanko, J., Porkka, E., Valkonen, A. and Järvinuoma, M. Active Vibration Control of Large-Scale Rotors. ICMA'02 Conference, held in Tampere, Finland. 2002. pp. 411-417.
- [47] LaBouff, G.A. and Booker, J.F. Dynamically Loaded Journal Bearings: A Finite Element Treatment for Rigid and Elastic Surfaces. *Journal of Tribology*. 1985. Vol. 107: pp. 505 - 515.

Appendix A Stiffness coefficients when $L/D = 0.25$.

1(2)

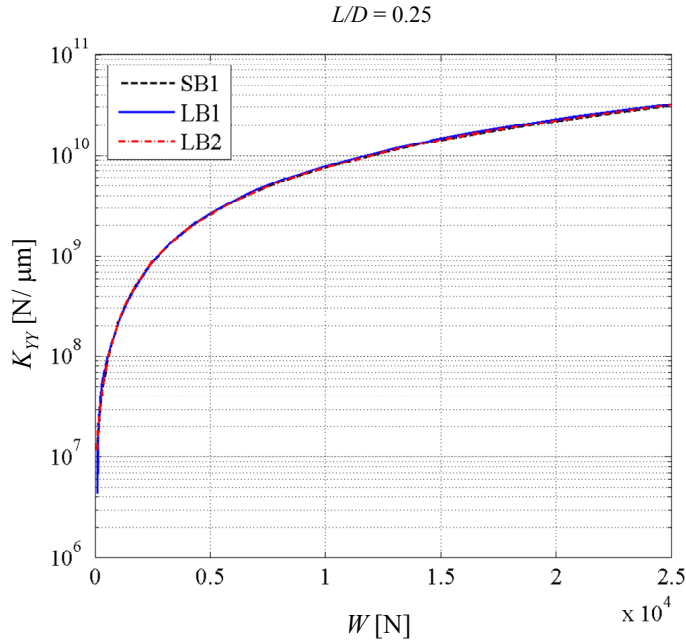


Figure A.1. K_{YY} according to bearing models when $L/D = 0.25$.

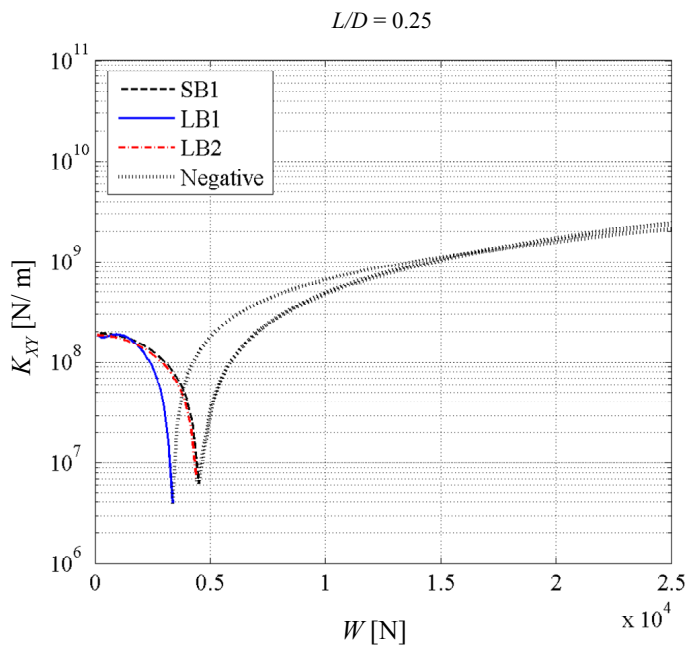


Figure A. 2. K_{XY} according to bearing models when $L/D = 0.25$.

Appendix A Stiffness coefficients when $L/D = 0.25$.

2(2)

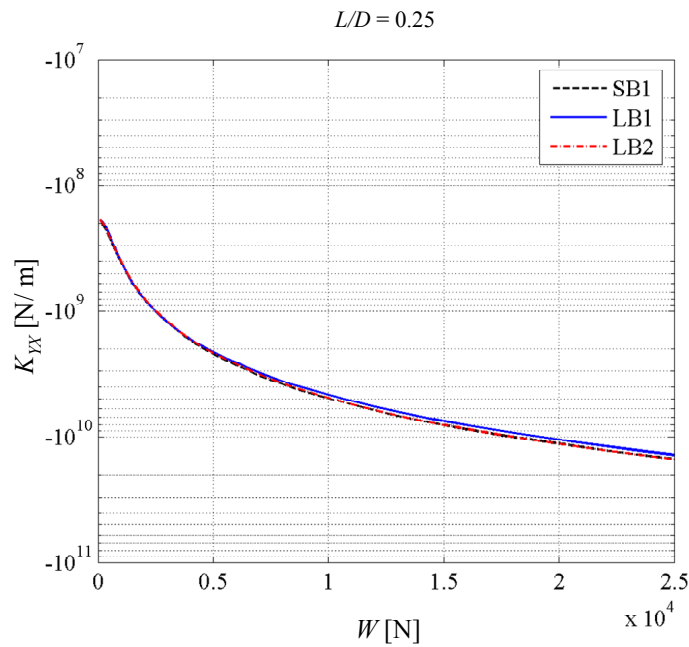


Figure A. 3. K_{YX} according to bearing models when $L/D = 0.25$.

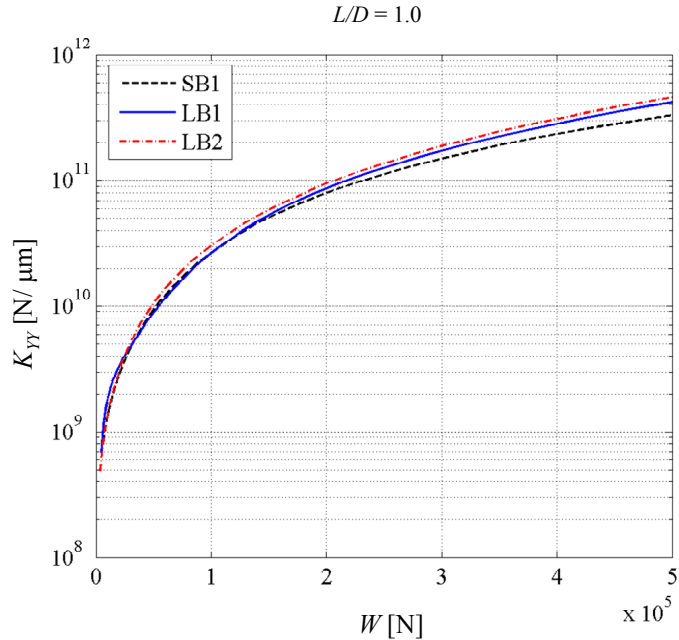
Appendix B Stiffness coefficients when $L/D = 1.0$.


Figure A. 4. K_{YY} according to bearing models when $L/D = 1.0$.

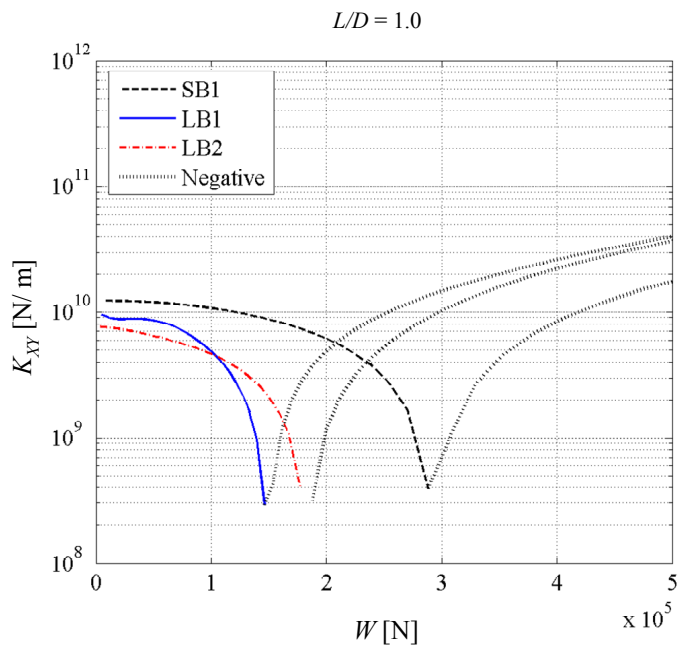


Figure A. 5. K_{XY} according to bearing models when $L/D = 1.0$.

Appendix B Stiffness coefficients when $L/D = 1.0$.

2(2)

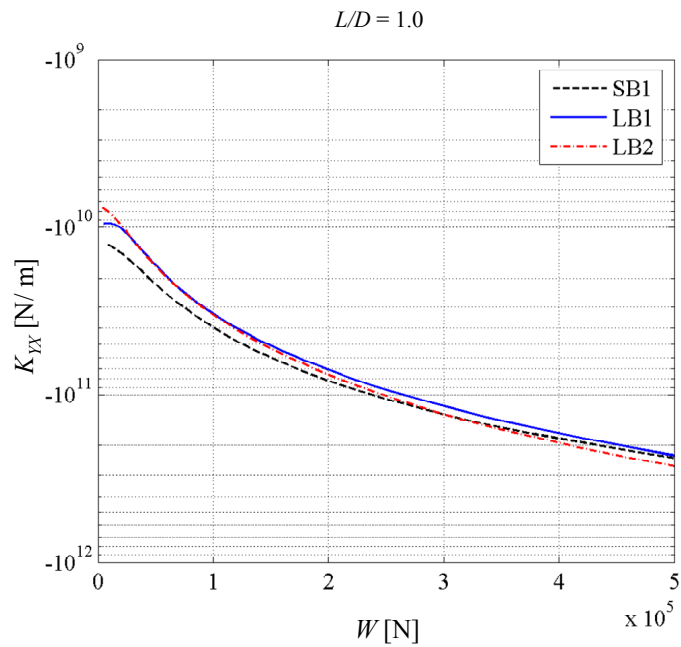


Figure A. 6. K_{YX} according to bearing models when $L/D = 1.0$.

Appendix C Damping coefficients when $L/D = 0.25$.

1(2)

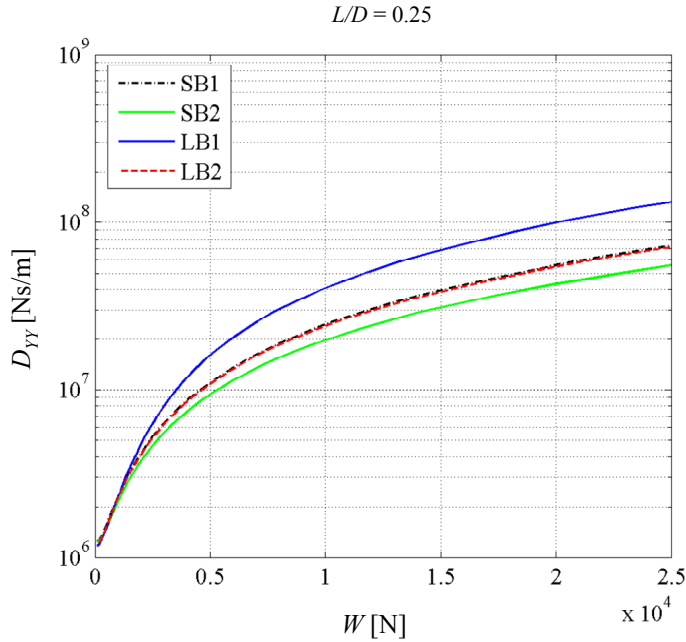


Figure A. 7. D_{YY} according to bearing models when $L/D = 0.25$.

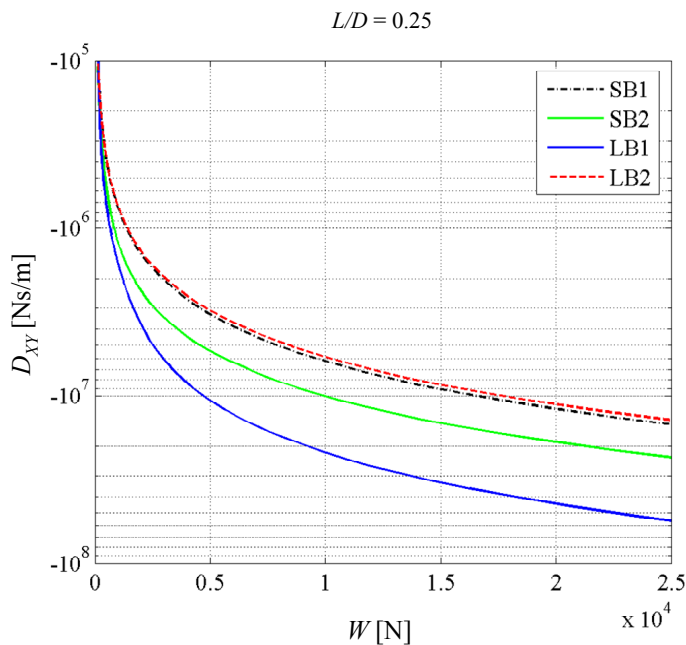


Figure A. 8. D_{XY} according to bearing models when $L/D = 0.25$.

Appendix C Damping coefficients when $L/D = 0.25$.

2(2)

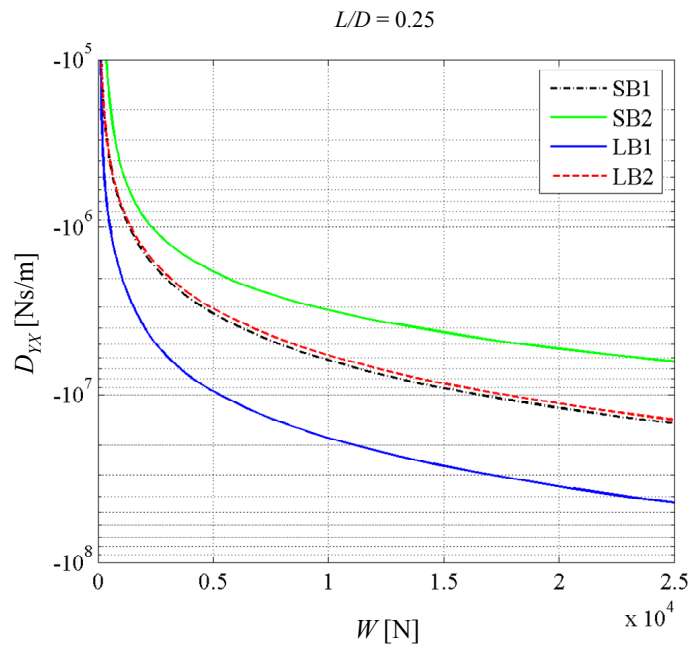


Figure A. 9. D_{YX} according to bearing models when $L/D = 0.25$.

Appendix D Damping coefficients when $L/D = 1.0$. 1(2)

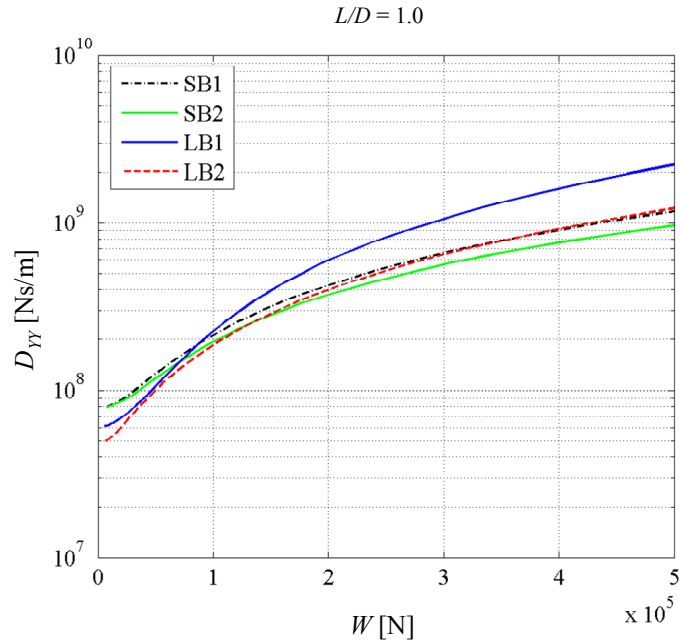


Figure A. 10. D_{YY} according to bearing models when $L/D = 1.0$.

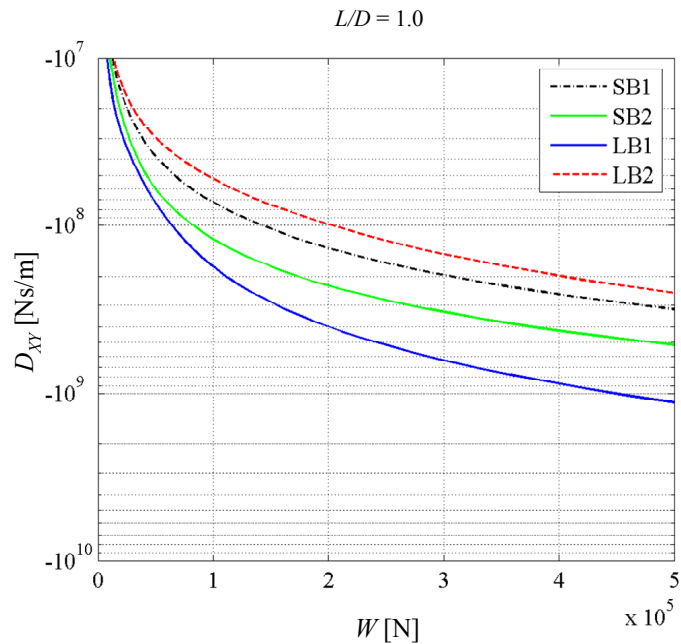


Figure A. 11. D_{XY} according to bearing models when $L/D = 1.0$.

Appendix D Damping coefficients when $L/D = 1.0$.

2(2)

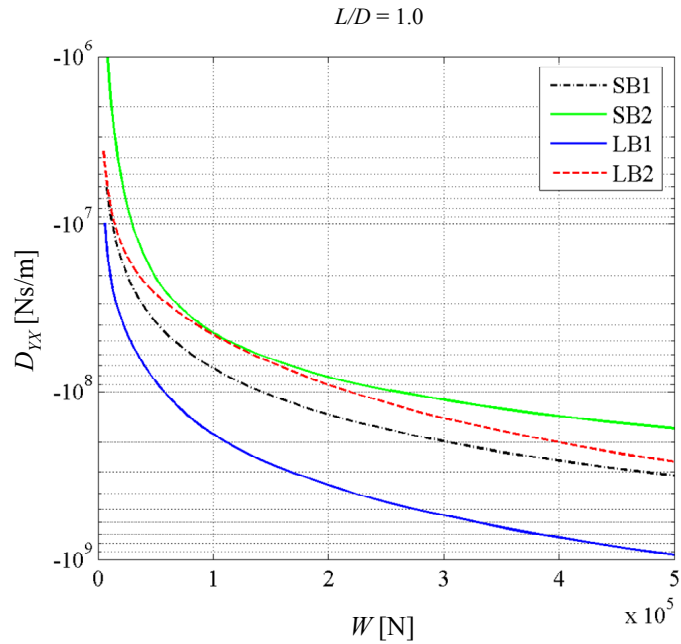


Figure A. 12. D_{YX} according to bearing models when $L/D = 1.0$.

**Appendix E Results from non-linear model without unbalance presented
in [36].**

1(2)

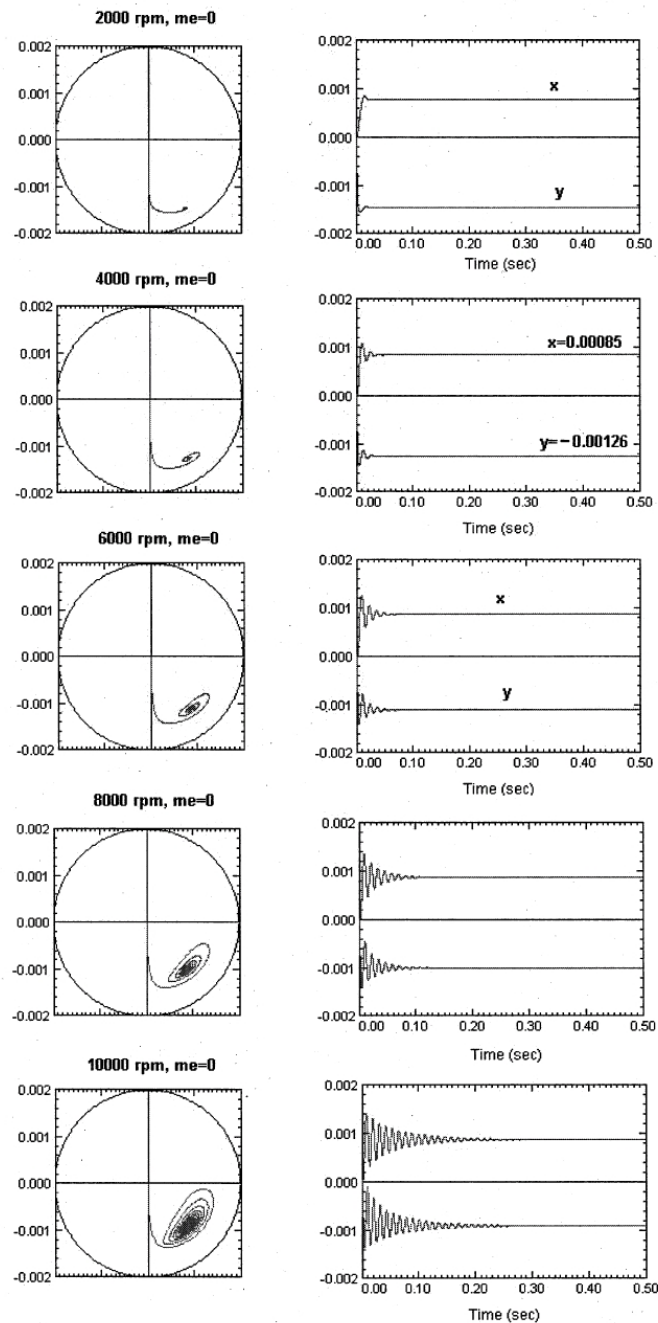


Figure 6.8-4 Journal equilibrium positions

**Appendix E Results from non-linear model without unbalance presented
in [36].**

2(2)

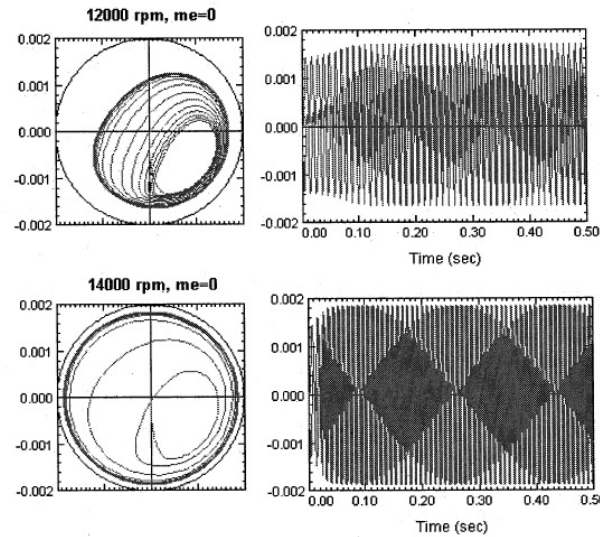


Figure 6.8-5 Journal equilibrium motion

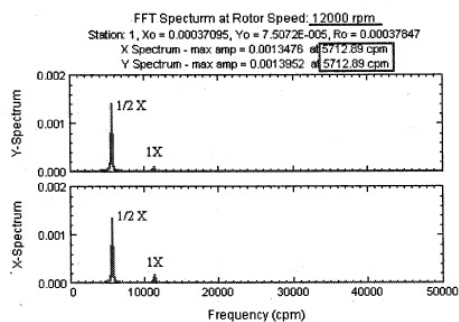


Figure 6.8-6 FFT at 12,000 rpm

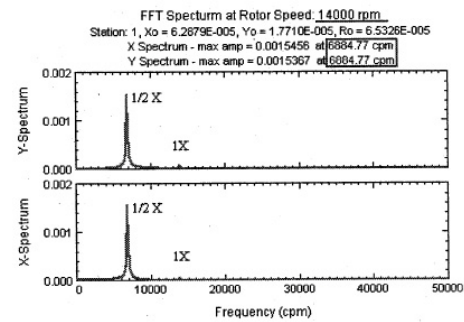


Figure 6.8-7 FFT at 14,000 rpm

**Appendix F Results from non-linear and linear model with unbalance
presented in [36].**

1(1)

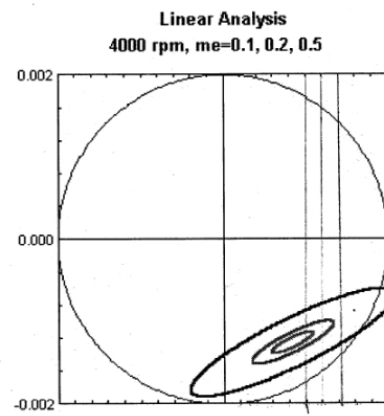
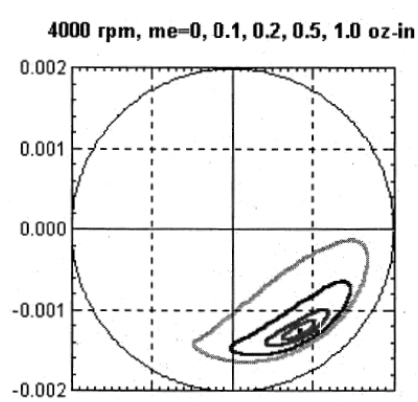


Figure 6.8-9 Journal steady state orbits

Figure 6.8-22 Steady state unbalance response orbits

ACTA UNIVERSITATIS LAPPEENRANTAENSIS

278. NEDEOGLO, NATALIA. Investigation of interaction between native and impurity defects in ZnSe. 2007. Diss.
279. KÄRKÄINEN, ANTTI. Dynamic simulations of rotors during drop on retainer bearings. 2007. Diss.
280. KARPOVA, TATJANA. Aqueous photocatalytic oxidation of steroid estrogens. 2007. Diss.
281. SHIPOLOVA, OLGA. Particle transport method for convection-diffusion-reaction problems. 2007. Diss.
282. ILONEN, JARMO. Supervised local image feature detection. 2007. Diss.
283. BOTAR-JID, CLAUDIU CRISTIAN. Selective catalytic reduction of nitrogen oxides with ammonia in forced unsteady state reactors. Case based and mathematical model simulation reasoning. 2007. Diss.
284. KINNUNEN, JANNE. Direct-on-line axial flux permanent magnet synchronous generator static and dynamic performance. 2007. Diss.
285. VALTONEN, MIKKO. Performance characteristics of an axial-flux solid-rotor-core induction motor. 2007. Diss.
286. PUNNONEN, PEKKA. Impingement jet cooling of end windings in a high-speed electric machine. 2007. Diss.
287. KÄRRI, TIMO. Timing of capacity change: Models for capital intensive industry. 2007. Diss.
288. TUPPURA, ANNI. Market entry order and competitive advantage of the firm. 2007. Diss.
289. TARKAINEN, ANSSI. Field sales management control: Towards a multi-level theory. 2007. Diss.
290. HUANG, JUN. Analysis of industrial granular flow applications by using advanced collision models. 2007. Diss.
291. SJÖMAN, ELINA. Purification and fractionation by nanofiltration in dairy and sugar and sweetener industry applications. 2007. Diss.
292. AHO, TUOMO. Electromagnetic design of a solid steel rotor motor for demanding operation environments. 2007. Diss.
293. PURHONEN, HEIKKI. Experimental thermal hydraulic studies on the enhancement of safety of LWRs. 2007. Diss.
294. KENGOL, ATHAKORN. An evaluation of ICTs investment using decision support systems: Case applications from distributor's and end user's perspective group decision. 2007. Diss.
295. LASHKUL, ALEXANDER. Quantum transport phenomena and shallow impurity states in CdSb. 2007. Diss.
296. JASTRZEBSKI, RAFAŁ PIOTR. Design and implementation of FPGA-based LQ control of active magnetic bearings. 2007. Diss.
297. GRÖNLUND, TANJA. Development of advanced silicon radiation detectors for harsh radiation environment. 2007. Diss.
298. RUOKONEN, MIKA. Market orientation in rapidly internationalizing small companies – evidence from the software industry. 2008. Diss.

299. OIKARINEN, TUIJA. Organisatorinen oppiminen – tapaustutkimus oppimisprosessien jännitteistä teollisuusyrityksessä. 2008. Diss.
300. KARHULA, JUKKA. Cardan gear mechanism versus slider-crank mechanism in pumps and engines. 2008. Diss.
301. RAJAMÄKI, PEKKA. Fusion weld metal solidification: Continuum from weld interface to centerline. 2008. Diss.
302. KACHINA, ANNA. Gas-phase photocatalytic oxidation of volatile organic compounds. 2008. Diss.
303. VIRTANEN, PERTTU. Evolution, practice and theory of European database IP law. 2008.
304. TANNINEN, KATI. Diffusion of administrative innovation: TQM implementation and effectiveness in a global organization. 2008. Diss.
305. PUUSTO, ANTTI. The initial oxidation of transition metal surfaces. 2008. Diss.
306. FELLMAN, ANNA. The effects of some variables on CO₂ laser-MAG hybrid welding. 2008. Diss.
307. KALLIOINEN, MARI. Regenerated cellulose ultrafiltration membranes in the treatment of pulp and paper mill process waters. 2008. Diss.
308. PELTOLA, SATU. Capability matrix – identifying and evaluating the key capabilities of purchasing and supply management. 2008. Diss.
309. HONKAPURO, SAMULI. Performance benchmarking and incentive regulation – considerations of directing signals for electricity distribution companies. 2008. Diss.
310. KORHONEN, KIRSI. Facilitating coordination improvement efforts in cross-functional process development programs. 2008. Diss.
311. RITVANEN, VIRPI. Purchasing and supply management capabilities in Finnish medium-sized enterprises. 2008. Diss.
312. PYNNÖNEN, MIKKO. Customer driven business model – connecting customer value to firm resources in ICT value networks. 2008. Diss.
313. AL NAZER, RAMI. Flexible multibody simulation approach in the dynamic analysis of bone strains during physical activity. 2008. Diss.
314. The Proceedings of the 7th MiNEMA Workshop. Middleware for Network Eccentric and Mobile Applications. Ed. by Pekka Jäppinen, Jouni Ikonen and Jari Porras. 2008.
315. VÄÄTÄNEN, JUHA. Russian enterprise restructuring – the effect of privatisation and market liberalisation on the performance of large enterprises. 2008. Diss.
316. DABAGHMESHIN, MAHSA. Modeling the transport phenomena within the arterial wall: porous media approach. 2008. Diss.
317. HAIMALA, JUHA. Supplier's position in project marketing networks. 2008. Diss.
318. UOTILA, TUOMO. The use of future-oriented knowledge in regional innovation processes: research on knowledge generation, transfer and conversion. 2008. Diss.
319. LAPPALAINEN, TOMMI. Validation of plant dynamic model by online and laboratory measurements – a tool to predict online COD loads out of production of mechanical printing papers. 2008. Diss.
320. KOSONEN, ANTTI. Power line communication in motor cables of variable-speed electric drives – analysis and implementation. 2008. Diss.